

Alma Mater Studiorum – Università di Bologna

DOTTORATO DI RICERCA IN CHIMICA

Ciclo 34

**Settore Concorsuale: 03/A2**

**Settore Scientifico Disciplinare: CHIM/02**

TOWARDS ECO-FRIENDLY BATTERIES: CONCEPTS FOR LITHIUM  
AND SODIUM ION BATTERIES

**Presentata da:** Christina Toigo

**Coordinatore Dottorato:**

Prof.ssa Domenica Tonelli

**Supervisore:**

Prof.ssa Catia Arbizzani

Co-Supervisore:

Prof. Karl-Heinz Pettinger

**Esame finale anno 2022**



*To my family*



## Table of contents

I	Acknowledgements .....	1
II	Abstract .....	2
III	Aim of the thesis.....	4
1	Introduction.....	1
1.1	General overview .....	1
1.2	Lithium Ion Batteries .....	2
1.3	Strategies to improve economic sustainability of lithium ion batteries .....	4
1.3.1	Active Materials.....	4
1.3.1.1	Cathode active materials.....	5
1.3.1.2	Anode active materials.....	8
1.3.2	Electrolyte.....	13
1.3.3	Inactive Materials .....	15
1.3.3.1	Separator .....	16
1.3.3.2	Conducting additives .....	17
1.3.3.3	Current collector.....	18
1.3.3.4	Binder .....	19
1.3.4	Processing.....	24
1.3.4.1	Dry mixing and dispersing .....	25
1.3.4.2	Coating.....	26
1.3.4.3	Drying .....	27
1.3.4.4	Calandring.....	27
1.3.4.5	Combination to half-cell or full cell .....	27
1.3.4.6	Calculation of electrode capacity .....	30
1.3.5	End-of-Life/Second-Life .....	30
1.3.5.1	Recycling of batteries .....	31
1.3.5.2	Second-life strategies .....	31
1.4	Sodium Ion Batteries .....	32
1.5	Strategies to improve economic sustainability of sodium ion batteries.....	33
1.5.1	Active Materials.....	34
1.5.1.1	Cathode active materials.....	34
1.5.1.2	Anode active materials.....	34
1.5.2	Electrolyte.....	35
1.5.3	Inactive Materials .....	36

1.5.3.1	Separators .....	36
1.5.3.2	Conducting additives .....	37
1.5.3.3	Current collectors .....	37
1.5.3.4	Binders.....	37
1.5.4	Processing.....	38
1.5.5	End-of-Life/Second-Life .....	38
1.6	Characterization techniques.....	38
1.6.1	Cycling tests.....	39
1.6.2	Cyclovoltammetric measurements .....	39
1.6.3	Electrochemical impedance spectroscopy .....	39
1.6.4	Capacitance measurement.....	40
1.6.5	Rheological properties.....	42
1.6.6	Life cycle analysis.....	43
2	Materials and methods .....	44
2.1	Chemicals.....	44
2.2	Characterization techniques and equipment.....	47
3	Anode formulations with water-based binders .....	56
3.1	Graphite with PVDF binder.....	56
3.1.1	Swelling and capacitance measurement.....	57
3.1.1.1	Swelling pre-tests .....	58
3.1.1.2	Swelling tests with EC/DMC .....	58
3.1.2	Mechanical and physicochemical measurements.....	60
3.1.2.1	EDX spectroscopy .....	60
3.1.2.2	Peeling test.....	61
3.1.2.3	Bending test.....	63
3.1.3	Electrochemical measurements of graphite anodes.....	64
3.1.3.1	Half cell tests .....	65
3.1.3.2	Full cell tests .....	67
3.1.4	Conclusion .....	69
3.2	LTO with sodium alginate binder .....	69
3.2.1	Bio-based polymers for battery applications .....	70
3.2.2	Chemical properties and application fields of sodium alginate .....	70
3.2.3	Physicochemical and mechanical measurements.....	72
3.2.4	Rheological properties of LTO-SA slurries .....	76
3.2.5	Result of rheological measurements.....	79
3.2.6	Result of contact angle measurements.....	83

3.2.7	Electrochemical measurements .....	84
3.3	LTO with mixed binders: comparison between PVDF/SA and PVDF/CMC.....	85
3.3.1	Chemical properties and application fields of CMC .....	86
3.3.2	Physicochemical and mechanical measurements .....	86
3.3.3	Rheological measurements .....	89
3.3.4	Electrochemical measurements .....	90
3.3.5	Electrode fading.....	93
3.3.6	Conclusion .....	94
4	Improved current collector surfaces for LTO electrodes .....	95
4.1	Influence of active material size.....	96
4.2	Physicochemical and mechanical measurements.....	96
4.3	Electrochemical impedance study.....	100
4.4	Conclusion .....	106
5	Preparation of Sodium Ion Battery .....	107
5.1	Evaluation of suitable anode and cathode materials.....	108
5.1.1	Selection of and synthesis process for anode material.....	109
5.1.2	Synthesis process of cathode material.....	116
5.2	Preparation of electrodes.....	118
5.3	Cyclovoltammetric measurements .....	120
5.4	Conclusion .....	124
6	Conclusions.....	126
7	References.....	128
8	List of acronyms.....	142
9	List of figures .....	145
10	List of tables.....	149
11	List of publications.....	150
12	List of contributions to conferences.....	151



## I Acknowledgements

My deepest gratitude goes to my supervisors Prof.ssa Catia Arbizzani for giving me the great opportunity to work alongside the highly scientific environment of the Laboratory of Electrochemistry of Materials for Energetics (LEME) of the Department of Chemistry of Alma Mater Studiorum - University of Bologna and Prof. Karl-Heinz Pettinger for his invaluable scientific support and the opportunity to spend 9 months of ERASMUS+ exchange at the Technology Center for Energy of Landshut University of Applied Sciences. Thanks to both of you for aiding in my growth as a student and researcher.

I am very grateful to my university colleagues Martin Frankenberger, Barbara Poisl, Bernhard Springer, Viktoria Peterbauer, Alexander Dinter, Mohammad Said El Halimi and Mehrdad Mashkour for manifold fruitful discussions and their great support and friendship.

I am also thankful to my colleagues at BlueSky Energy, especially Neha Ghanbahadur, Christoph Thilker, Jonathan Schubert and Thomas Krausse.

I kindly acknowledge the financial support given by the ERASMUS+-Programme (grant number 2019-IT02-KA103-061398) who funded my internship at HAW Landshut as well as my employer BlueSky Energy for further financial support.

Finally, I would express my deepest gratitude to my family, who supported me in any kind in pursuing this work...

## II Abstract

In general, the intelligent and efficient use of energy storage systems will be one of the main challenges for a successful implementation of strategies against climate change. Alternative and renewable ways of energy generation have emerged within the last decade, suffering from the problem of not being available at any day- and night-time. Therefore, the produced energy needs to be stored in an effective way for being used at any given time. For this purpose, lithium ion batteries have been developed and are utilized in multiple ways. With all the enthusiasm accompanying battery development, one should not forget that raw materials like lithium and cobalt are limited, too. Therefore, the question of battery sustainability is arising, trying to balance raw material availability, mining and manufacturing with its positive effects on the reduction of fossil fuel dependency.

Several aspects have to be considered and reveal a high impact on the further increase of research topics related to sustainability. On the one hand, an increased awareness on ecological aspects is becoming more and more apparent both for individuals but also for companies and even national economies. On the other hand, people are getting aware of the additional safety issues related with standardly used lithium ion batteries. At the moment human mankind is performing the step from commonly used small-scale applications in mobile phones, laptops and many more to large-scale applications in electric vehicles (EVs) and home/industrial storage systems. So in future, enormous amounts of energy will have to be stored and of course, safety aspects are of rising interest with higher proportions of batteries in people's surroundings. As a last aspect, it is worth mentioning that also economic aspects are of interest. Great amounts of funding are provided, concentrating on renewable energy systems in general, and an improvement of its sustainability, recyclability and effectivity in special. All these factors indicate the urgent need to delve into the topic of sustainable energy storage, both for well-established systems and newly developed ones.

Several possibilities are arising aiming the development of "greener", more sustainable energy storage systems. One point is the completely water-based processing of battery electrodes, thus being able to renounce the use of toxic solvents in the preparation process. Despite its advantage of lower cost and eco-friendliness, there is the need of similar mechanical and electrochemical behavior for boosting this preparation mode.

Another point – accompanying the water-based processing - is the replacement of solvent-based polymer binders by water-based ones. These binders can be based on fluorinated, crude-oil based polymers on the one side, but also on naturally abundant and economic friendly biopolymers.

The most common anode materials, graphite and lithium titanate (LTO), have been subjected a water-based preparation route with different binder systems. LTO is a promising anode material for lithium ion batteries (LIBs), as it shows excellent safety characteristics, does not form a significant SEI and its volume change upon intercalation of lithium ions is negligible. Unfortunately, this material suffers from a rather low electric conductivity - that is why an intensive study on improved current collector surfaces for LTO electrodes was performed.

In order to go one step ahead towards sustainable energy storage, anode and cathode active materials for a sodium ion battery were synthesized. Anode active material resulted in a successful product which was then subjected to further electrochemical tests.

In this PhD work the development of “greener” energy storage possibilities is tested under several aspects. The ecological impact of raw materials and required battery components is examined in detail.

### III Aim of the thesis

This thesis addresses several sustainability aspects for lithium and sodium ion battery systems and aims to investigate different approaches for increasing the sustainability of battery materials for lithium and sodium ion batteries, with a detailed insight to state-of-the-art materials and processing as well as sustainable and practically working alternatives.

The main focus lies on the use of solvent-free, water-based binder systems and sustainable raw and active materials with low environmental impact and their characterization.

In chapter 1, basic concepts of lithium and sodium ion batteries are provided, ranging from raw materials, their processing and further preparation steps to the assembly of a battery – each of them with a side-view on sustainability-related topics.

Chapter 2 deals with the used chemicals, the preparation steps of anodes, cathodes and electrochemical cells, and the different characterization techniques which were used in this thesis.

Chapter 3 is focusing on anode formulations comprising of solvent-free and water-based binders. As anode active materials, graphite and LTO are used. They are combined with aqueous poly vinylidene fluoride suspensions, carboxy methylcellulose and sodium alginate as polymeric binders.

In chapter 4, an improvement of LTO electrodes by the modification of current collector foil is addressed. This modification is performed as copper deposition by pulsed current and clearly demonstrates an improved connection and an increased active surface area.

In chapter 5, the focus lies on the preparation of different anode and cathode materials for the use in SIBs and various characterization techniques.

# 1 Introduction

## 1.1 General overview

By the use of fossil fuels and with a forthcoming industrialisation, human mankind is influencing the earth's climate in a significant way. Several strategies initiated by the European Union are now to be followed in order to decrease human CO<sub>2</sub> emission and keep the global temperature increase at the lowest possible level. In addition to a promotion of topics like the fast development of renewables, carbon capture and storage and circular economy, a big issue is also to maximize energy efficiency and the use of electricity for energy supply [1]. Due to the fact that most renewable energy sources are fluctuating ones and a power grid is not able to store energy, there is a huge need for energy storage systems.

Since their discovery and further development in the 1970s and 1980s by Nobel Prize Laureates John B. Goodenough, M. Stanley Whittingham and Akira Yoshino, LIBs have been established as the main energy storage system not only for portable electronics but also more and more for applications in EVs and stationary storage devices. Therefore, LIBs are key components for energy transition by means of storing excess energy in times of oversupply and revealing energy when it is required.

During the last decades, LIBs have been further developed by optimizing properties like energy density, life time, safety and costs. But not only are these aspects of importance. People are getting more and more aware of topics affecting long-term influences on both nature and mankind – namely, topics related to sustainability, ethical behavior and possible impacts of sourcing and material release after standard battery lifetime. These aspects may seem like “soft aspects” in contrast to the “hard”, fact- and data-based aspects like energy density and charge capacities, but have nevertheless an increasing impact on the whole industry, driven by consumer needs and wishes.

In recent times, several so-called “post-lithium”-technologies are emerging and under development, being aware of the risks related to supply chains of nowadays' batteries and in particular in regard to the provision of raw materials [1]. The quite low abundance of lithium (20 ppm) compared to sodium (23600 ppm) in the earth crust gives further rise to an accelerated research on alternative battery technologies based on sodium [2].

Kulova et al. defined the term “post-lithium-ion batteries” as electrochemical systems whose specific energy is significantly higher than the specific energy of modern LIBs. They also include battery systems, whose specific energy is comparable to the one of modern commercial LIBs, but their projected costs will be significantly lower [3]. The three technologies of lithium-oxygen batteries, sodium ion batteries and lithium-sulfur batteries are currently referred to as post-lithium-ion systems [3].

Of course, several other technologies are currently under different stages of research, like magnesium, potassium, aluminium or calcium-based systems. A more detailed look into optimization possibilities on anodic and cathodic side of LIBs and SIBs will be given in the following chapters.

## 1.2 Lithium Ion Batteries

The chemical element lithium, with its lowest density of  $0.534 \text{ g/cm}^3$ , the lowest standard potential of  $\text{Li/Li}^+$  ( $-3.05 \text{ V vs SHE}$ ) and the lowest weight of all metals – thus allowing highest energy densities – is in the spotlight of battery development since the last decades [4]. It is used for manifold applications and one cannot imagine everyday life without mobile phones, tablets and laptops based on this technology. A basic configuration of a LIB is represented in Figure 1:

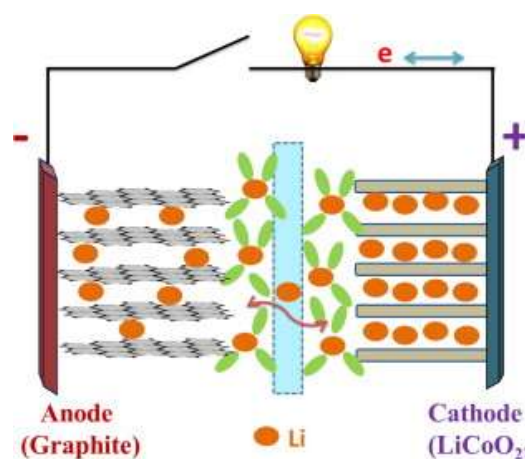


Figure 1: Scheme of lithium insertion/de-insertion  
Reprinted from ref [5] under the terms of the Creative Commons CC-BY license.

The electrodes in a rechargeable system are named according to their function in discharge mode; the anode is the electrode where electrons are released by oxidation (“minus-pole”), the cathode is where reduction takes place (“plus-pole”).

Lithium ions are migrating between the positive and negative electrodes and are inserted within the corresponding active material. During the charging process, electrons are directed into the anode. To keep electrical neutrality, the positive lithium ions are released from the cathode, migrate to the anodic side and are intercalated into the anodic material. The reverse process is taking place during discharging, where lithium ions are migrating from anode to cathode. This combination of lithium intercalation and de-intercalation can be visualized by the movement of a rocking chair and is therefore often called the “rocking chair principle”.

Both anode and cathode materials are named active materials, as they must be able to host lithium ions in a reversible way. Some electrode materials react with lithium to give alloys or other lithiated products. Depending on the active material’s intrinsic conductivity, it may be necessary to add a conducting additive like carbon black (CB). Furthermore, a (polymeric) binder is required to enable a good connection within the active material as well as to the current collector.

Several different materials are currently in use or under research as active materials for LIBs. On the cathode side, there is the need to provide a host framework into which the lithium ion is inserted reversibly [6], so both the lithiated and delithiated structure should own a stable framework. Typically, used materials are layered oxides, spinels and phosphates.

On the anodic side, too, insertion materials are used, where the insertion takes place in a reversible way, preferable with negligible or no volume expansion. Typically, used materials are graphite and lithium titanium oxide (LTO).

An electrolyte is necessary to move the ions from one electrode to the other – so a high ionic mobility within the electrolyte is crucial. Some further parts of a battery are binder and conducting additive within the composite electrode material as well as separator and current collectors.

### 1.3 Strategies to improve economic sustainability of lithium ion batteries

Many different definitions on the economic sustainability of batteries can be found – some concentrating on life cycle analysis (LCA) of complete batteries for mobile and stationary applications [7,8] but also of cathode materials itself [9]. One approach is to rate the environmental intensity of materials by describing the extent to which production and usage of a material can cause damages to critical areas [10]. Several aspects have to be considered for an evaluation of battery sustainability; for example, a higher energy density is accompanied by less required mass of active material leading to less ecological impact. A high cycle life shows positive impact on battery sustainability, as the battery does not have to be replaced very soon by a newly produced one.

Herein economic sustainability is defined as the property of a battery with less damaging effects on the environment, hence the use of raw materials with good availability, minimum or no toxicity and good degradability.

#### 1.3.1 Active Materials

Active materials are electrochemically active components ensuring the storage of energy within the battery. To reach high energy densities, the specific charge of the active materials needs to be as high as possible. This means a high amount of released or absorbed electrons per mass unit is favourable and determines the storage capacity. The used cathode has a great influence on battery performance, as storage capacity depends on how many and how easily lithium ions are extracted from the cathode [11]. Furthermore, a suitable range of the active materials particle size is crucial – it should be as small as possible so the ions have short diffusion ways to travel and as big as necessary to ensure the formation of structures. Smaller active material particles ensure an improved connection to the other electrode components and can therefore realize a higher degree of possible interactions. On the other side, with decreasing particle size, a higher area is exposed to the electrolyte and the reactions that bring to the formation of thin layers on the particles become more important. In some cases these layers are beneficial, like solid electrolyte interface (SEI) in graphite anodes, or cathode electrolyte interface (CEI) in high-voltage cathodes to further prevent the reaction with the

electrolyte. On the other hand, if these layers are too thick, they passivate the electrodes and increase overall resistance. Furthermore, preparation processes are complicated with strongly decreasing particle sizes.

Most active materials lack in electric conductivity and need to be combined with conducting additives, which can lead to reduced energy density within the whole system.

#### 1.3.1.1 Cathode active materials

As mentioned above, lithium-rich compounds are able to form mixed crystals over a wide range of composition. These are namely layered oxides, spinels and phosphates - the most commonly used cathode materials for LIBs. Depending on their structure, charge and size differences between ions, layered oxides can offer fast two-dimensional lithium-ion diffusion and conductivity, as for example  $\text{LiCoO}_2$  (lithium cobalt oxide, LCO) or  $\text{LiNi}_{1-y-z}\text{Mn}_y\text{Co}_z\text{O}_2$  (lithium nickel manganese cobalt oxide, NMC) [12]. Spinel with a crystal structure  $\text{AB}_2\text{X}_4$  like  $\text{LiMn}_2\text{O}_4$  (LMO), or  $\text{LiNi}_2\text{O}_4$  (LNO) allow a three-dimensional movement of lithium ions.

One further group of cathode materials are phosphates, crystallizing in an olivine-like structure (e.g. lithium iron phosphate, LFP or lithium iron manganese phosphate, LFMP). The ionic movement in olivine structures is here limited on a one-dimensional channel system with little possibility for crossing between the channels [13].

Different cathode chemistries of course lead to different charging and discharging curves, resulting from their different cell voltages. Exemplary, one cycle of charging and discharging (CC-CV, respectively CC, as explained in 1.6.1 *Cycling tests*) is depicted in Figure 2. Here, LFMP (in this case, exactly  $\text{LiFe}_{0.33}\text{Mn}_{0.67}\text{PO}_4$ ) was selected as cathode material and combined with a graphite anode. LFP was one of the first cathode materials to be commercialized and is still very commonly used. It owns a high reversible capacity, good structural stability and inherent safety properties. Nevertheless, it has to cope with a low intercalation voltage of about 3.5-3.6 V vs  $\text{Li}/\text{Li}^+$ . Looking at its manganese analogue material lithium manganese phosphate (LMP), one can find a high theoretical capacity, a suitable redox potential (4.1 V of  $\text{Mn}^{2+}/\text{Mn}^{3+}$  vs.  $\text{Li}/\text{Li}^+$ ) combined with a low discharge capacity and bad rate performance. There is the possibility to combine those two materials in terms of a partial substitution of iron by manganese atoms, thus obtaining isostructural  $\text{LiFe}_{0.33}\text{Mn}_{0.67}\text{PO}_4$ . The presence of manganese

is additionally advantageous for this material leading to an increased cell voltage. As visible in Figure 2, the influence of manganese can clearly be seen at the two voltage plateaus corresponding to the two redox couples  $\text{Fe}^{2+}/\text{Fe}^{3+}$  at 3.6 V and  $\text{Mn}^{2+}/\text{Mn}^{3+}$  at approximately 4.1 V. What is also visible at first sight is that the step correlated to the iron redox couple takes around one third of the time when compared to the step of the manganese redox couple. This can easily be ascribed to the ratio of iron to manganese in the active material, which is 0.33 to 0.67.

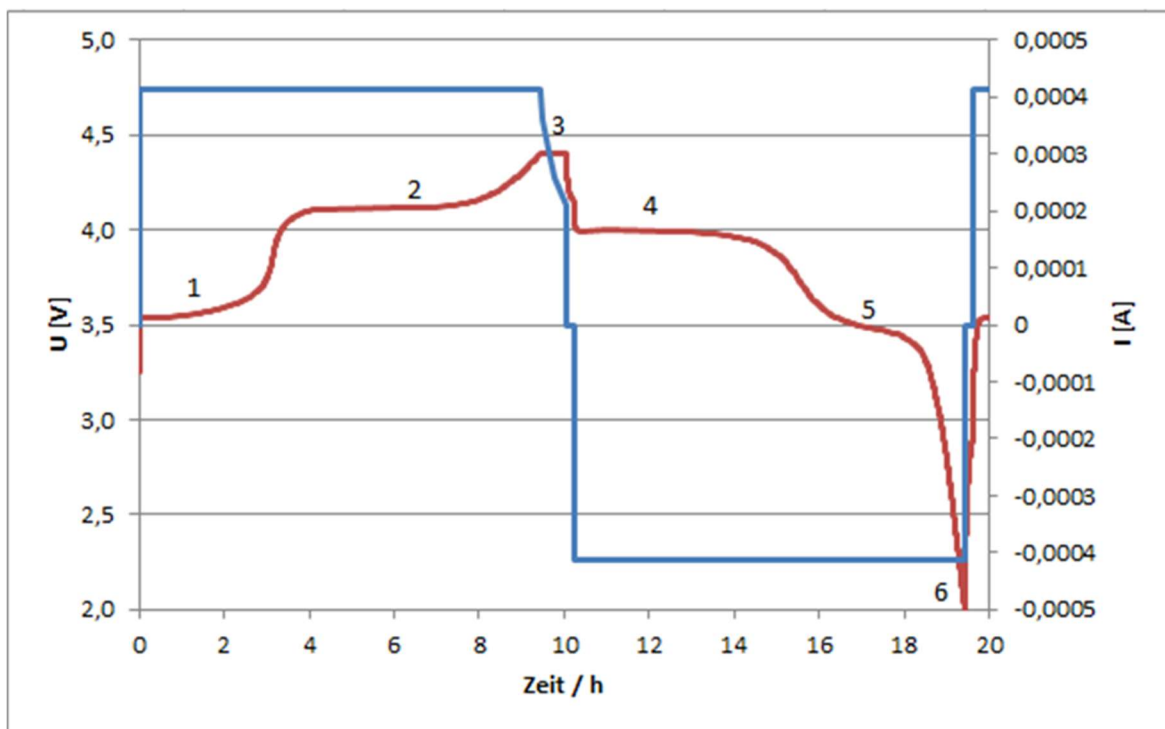


Figure 2: Typical charging-discharging cycle of a LFMP/graphite full cell, performed at C/10 rate. CCCV charging up to 4.3 V and CC discharging up to 2.0 V [14].

In general, there is a big variety of possible cathode materials for LIBs, some of which are well-established and other recently developed. Depending on their properties like theoretical capacity and operating voltage vs.  $\text{Li}/\text{Li}^+$ , an appropriate cathode material for a defined battery can be chosen. Of course, it is not all about “hard facts”, but also about sustainability, especially topics concerning raw material availability and ethical mining of those materials, and further safety aspects.

Wang et al. assessed the environmental sustainability of cathode materials based on three LCA approaches and came to the result that sustainability decreases sequentially from

$\text{LiFe}_{0.98}\text{Mn}_{0.02}\text{PO}_4$  – LFP – LCO due to toxicity and land issues as well as resource consumption [9]. Early stage sustainability evaluation of Hischer et al. reports similar results with lowest impact of LFP, followed by NMC and LCO [15]. A list of commercially available and frequently used cathode materials can be found in Table 1.

Table 1: List of LIB cathode materials.

Cathode material	Formula	Theor. capacity [mAh g <sup>-1</sup> ]	Potential vs Li/Li <sup>+</sup> [V]
Lithium iron phosphate (LFP)	$\text{LiFePO}_4$	170 [11]	3.6
Lithium Nickel Cobalt Manganese Oxide (NCM)	$\text{LiNi}_x\text{Mn}_y\text{Co}_z\text{O}_2$ (NCM622, NCM811...)	275	3.7-5.0
Lithium Manganese Oxide (LMO)	$\text{LiMn}_2\text{O}_4$	285 [16]	4.1
Lithium Cobalt Oxide (LCO)	$\text{LiCoO}_2$	274 [16]-280 [11]	3.7[17]
Lithium Nickel Cobalt Aluminium Oxide (NCA)	$\text{Li}[\text{Ni}_x\text{Co}_y\text{Al}_z]\text{O}_2$	275 [18]– 279 [19]	4.3
Lithium Nickel Manganese Spinel (LNMO)	$\text{LiNi}_{0.5}\text{Mn}_{1.5}\text{O}_4$	146 - 147 [11]	4.7
Lithium Iron Manganese Phosphate (LFMP)	$\text{LiFe}_{0.33}\text{Mn}_{0.67}\text{PO}_4$ (several molecular ratios Fe-Mn possible)	170 [20]	4.1

To summarize the overview on cathode materials given in Table 1, the following metals are under commercial use in LIB cathodes: lithium, cobalt, iron, nickel, manganese and aluminium. Arranging these metals according to their occurrence in the earth crust, one finds this order: aluminium (8.07 %), iron (5.05 %), manganese (0.09), nickel (0.008 %), lithium (0.006 %) and cobalt (0.004 %).

As lithium-based batteries cannot be prepared and operated without lithium, one has to find the most critical raw materials besides the indispensable lithium in terms of abundance and sustainability.

In accordance with the above mentioned low occurrence of cobalt in the earth crust, it was also found out that cobalt is the most valuable metal used in LIBs by far and it is considered a critical resource as ~60 % of the worldwide production in 2018 originated from mines located

in the Democratic Republic of the Congo, where political instability and unethical working conditions are well documented [21]. Especially artisanal and small-scale miners are associated with mining with hand tools and only little protection and safety measures with a high risk for back injury and lung diseases as well as accidents [22]. Combining this knowledge with the fact that cobalt reserves are limited and deficits in cobalt supply are estimated to occur by 2030, there is no alternative but to encouraging further research on cobalt-free cathode materials.

Going one step ahead to the next least available metal one reaches nickel with an abundance of 0.008 % in the earth crust. The momentary use of nickel for battery applications is estimated at 3-4 % of the global nickel consumption [23]. Nickel-rich cathodes like NMC contain between 30-72% of nickel, forecasting that between 2017 and 2025 the use of nickel in batteries will grow with 39 % per year [23]. So also this raw material will become more and more valuable, even if recycling of LIB will not be enforced dramatically. Nickel is furthermore associated with some risks concerning human health, such as allergies, cardiovascular and kidney diseases, lung fibrosis as well as lung and nasal cancer [24]. The molecular mechanisms behind nickel-induced toxicity are not yet completely understood [24].

Though nickel-based cathodes are an interesting and somehow viable alternative or at least supplement to cobalt-based ones, the question of environmental friendliness and harmfulness has to be kept in mind.

In terms of sustainability, the use of heavy metals like cobalt or nickel is at least questionable and should be avoided, even though they are increasing both specific capacity and energy density.

#### 1.3.1.2 Anode active materials

On the anode side, active materials are limited to a quite small number. Graphite is the oldest and most commonly used anode material for its good cycling performance and its ability to reversibly intercalate and release (de-intercalate) lithium ions due to its layered structure. It has a high specific capacity, low redox potential (properties see Table 2) and is both abundant and cheap. The layered crystal structure of graphite is depicted in Figure 3.

Typically one lithium ion per six carbon units can be intercalated, leading to  $\text{LiC}_6$ . Graphite has a high theoretical capacity of  $372 \text{ mAh g}^{-1}$  and exhibits good cycling stability. Its high electric conductivity can easily be described by the chemical structure of graphite: each carbon atom owns four valence electrons where each of them is able to form connections to neighbouring atoms. In graphite, only three of the four valence electrons form bondings, the one electron left is free and is thereby allowing an electrical conductivity of  $2500 \cdot 10^3 \text{ S m}^{-1}$  [25].

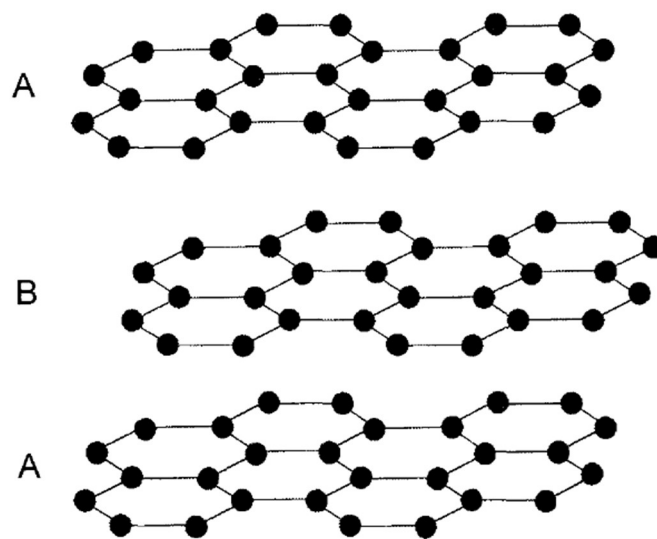
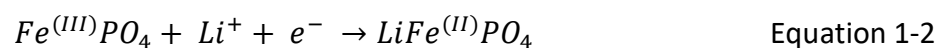


Figure 3: Layered structure of graphite, reprinted from ref. [26] with permission of Springer Nature.

The prismatic surfaces between the layers A and B are open for intercalation reactions [26] according to equation 1-1. During the discharging process, lithium ions are de-intercalated from the graphite electrode and transported to the cathodic side. The electrons are transferred via the outer circuit. Both lithium ions and electrons are incorporated into the cathode, where – exemplary for LFP as cathode material - a reduction of  $\text{Fe(III)}$  to  $\text{Fe(II)}$  takes place according to equation 1-2.



On the surface of the graphite electrode some irreversible reactions resulting in the formation of a SEI take place. This SEI is mainly dependent on the used electrolyte carbonates and should

be both electrically insulating to prevent further decomposition of electrolyte and also be ionically conductive to enable mass transfer of  $\text{Li}^+$  from the electrolyte to the graphite interlayer spaces [27]. The SEI is consisting of precipitates from reduced decomposition of solvents, salts, lithium ions and electrolyte impurities due to its instability at anode potential operating window built upon its outer layer [28], as can be seen in Figure 4. It is mostly formed during the first charging and formation is continuing slowly and gradually until the SEI layer is completely developed [28]. On the one hand the SEI is advantageous as it protects the negative electrode from solvent co-intercalation but on the other hand it consumes lithium inside the battery which is then no longer available for energy storage processes and leads to irreversible capacity losses [29,30]. In combination with the fact that safety concerns like lithium plating and the formation of lithium dendrites are to be addressed, long-term operation reliability of graphite anodes is at least questionable [31].

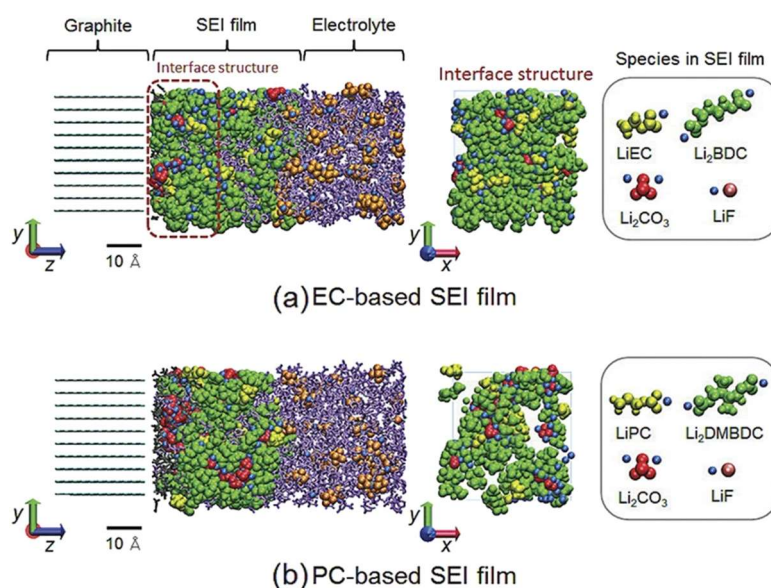


Figure 4: Scheme of graphite electrode covered with an inhomogeneous SEI. Reprinted from ref. [32] under the terms of the Creative Commons CC-BY license.

Battery-grade graphite can be obtained from natural or synthetic graphite, both owning its pros and cons. Natural graphite is a mineral found in nature, formed by shales and limestones at the boundaries of convergent plate margins when subjected to heat and pressure, forming tiny flakes of graphite in the rock [33]. The mining of natural graphite is mainly taking place in China, Korea, India, Brasil and is accompanied by several drawbacks, including the enormous

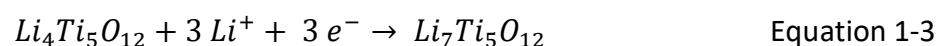
dust generation leading to a decreased lung function and the use of organic acids like hydrofluoric acid for its purification [34].

Synthetic graphite is prepared in different ways depending on its educts. Those are classically unstructured carbons like coal, coke or bituminous coal [35]. High temperature processes like Acheson graphitization and the Desulco<sup>®</sup> process are the most common ones and offer the advantage of a certain influence on the latter graphite properties [36]. Nevertheless, those processes are very energy-intensive walking along with great amounts of emissions. Publications within the last years very often concentrate on possible routes based on biomass or lignocellulose, both implementing a sustainability factor and shifting this topic into the wider field of circular economy [37].

A further promising anode material is lithium titanate,  $\text{Li}_4\text{Ti}_5\text{O}_{12}$ , a spinel owning a lithium insertion voltage of 1.55 V vs  $\text{Li}^+/\text{Li}$ , where the commonly used electrolytes are thermodynamically stable and thus avoids the electrochemical formation of a SEI from ethylene carbonate reduction [38,39]. The rather high lithium insertion voltage of the redox couple  $\text{Ti}^{4+}/\text{Ti}^{3+}$  indicates end-of-charge signalling the onset of oxygen evolution from the cathode material due to overcharge, whereas graphite lacks this safety issue intercalating at a potential close to that of lithium plating [40].

LTO has not only excellent safety characteristics and very long lifetime, but also shows good C-rate capability and fast lithium intercalation, which are the most important advantages of LTO [41]. It can accommodate up to three lithium ions per formula unit in its spinel structure with negligible volume change [42]. Therefore, LTO is considered as a zero-strain material, with a volume increase of 0.2 % for lithiation [43].

The electrochemical reaction corresponding to the accomodation of three lithium ions can be written as follows:



In contrast to the above mentioned advantages, LTO has scarce electrical conductivity and low Li-ion diffusion coefficient [39,44,45]. Its poor electrical conductivity is related to the occupied  $8a$  tetrahedral positions and it can be improved at elevated temperatures due to the transfer of Li-ions from the  $8a$  to the vacant  $16c$  octahedral positions [40]. The aforementioned negative properties result in a rather low theoretical capacity of  $175 \text{ mAh g}^{-1}$  [46].

A number of different approaches has been attempted to overcome these drawbacks. Wang et al. performed a synthesis of LTO and added different amounts of citric acid, which was then pyrolysed and distributed between the LTO particles, thus hindering agglomeration of LTO particles and leading to a retard of the particle growth during the sintering process [47]. The so-prepared carbon-coated LTO resulted in highly improved charge/discharge properties in contrast to pristine LTO.

Chou et al. have synthesized LTO nanoparticles with improved rate capability [38]. Carvalho et al. showed that the use of mild acids as pH-modifier and different polysaccharide binders affect LTO electrode morphology, adhesion and electrochemical properties [48]. Many other binders have been evaluated for their usability in combination with LTO in recent years, e.g. sodium alginate (SA) [41,44,49,50], carboxymethyl cellulose (CMC) [51], acrylic binder LA132 [52], polyethylene glycol (PEG)-based binder [53], polyacrylic acid or bio-derivative rosin [54]. Some further approaches have dealt with the task of doping LTO with metal or non-metal ions in the Li, Ti or O sites [42]. This has been performed as cation or anion doping with  $F^-$ ,  $Cl^-$ ,  $Br^-$  and  $N^{3-}$ , for example as having similar sizes as compared with  $O^{2-}$  with the goal to facilitate the substitution process [55].

Another promising approach to ameliorate LTO performance is the modification of the current collector in such a way that an improved contact with the active material is established and the overall resistance is significantly reduced. Different ways of modification have been under investigation, e.g. a thin layer of graphene applied on the surface of the Cu foil [39], carbon-coating on aluminium current collector [56], a laser structuring with various types of dot patterns [57], laser-assisted processing to the active material itself [58], synthesis of a compact oxide layer upon aluminium current collector [59], different surface morphologies of aluminium current collector [60] and so-called laser-induced periodic surface structures on steel and copper surfaces [61]. A type of modification derived from printed circuit board technology is the so-called nodular treatment. This treatment was established in the 1960s for enhancing the bonding strength of copper foil versus substrates used for printed circuit boards. The goal is to form interlocking structures on the copper surface for the epoxy resin. This is achieved by electrolytic deposition of copper dendrites onto the surface of the foil.

Battery-grade LTO can be synthesized in many different ways including solid-state, hydrothermal and solvothermal methods, just to name a few of them. Depending on the

synthesis route, the obtained LTO may have to be ball-milled to reach the desired, small particle sizes in the range of about 10 or less nanometers.

Silicon is a further possible anode material with a high gravimetric capacity of 3600 mAh g<sup>-1</sup> and several advantages like low toxicity, and high natural abundance [62]. Nevertheless, it suffers from both low conductivity and low initial Coulombic efficiency (CEf) [63]. The most weighty disadvantage is the fact, that a large volume change leads to anode self-pulverization [64] during several cycles of charging and discharging.

Table 2 gives an overview of possible anode materials

*Table 2: Overview on different anode materials for LIBs.*

<b>Anode material</b>	<b>Potential vs Li<sup>+</sup>/Li [V]</b>	<b>Specific theoretical capacity [mAh g<sup>-1</sup>]</b>	<b>SEI</b>	<b>Volumetric volume change</b>
Graphite	0.1	372	Yes	~ 10-13 % [65,66]
LTO	1.55	175	No	0.2-0.3 % [42,43]
Silicon	0.2 [43]	3579	Yes	400 % [67]

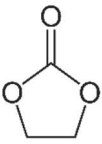
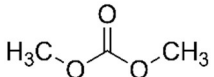
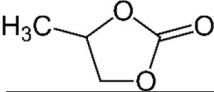
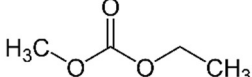
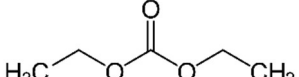
### 1.3.2 Electrolyte

Electrolytes act as a medium for ion transfer within the battery and consist both of a solvent and a salt. In general, they are in liquid state to ensure good wetting of the composite electrodes solid surface. This is also related to a low impedance across the liquid/solid interface resulting in faster charge transport [68]. Requirements for electrolytes are a high ionic conductivity, good chemical and electrochemical stability, safety and of course cost. A high dielectric constant and small viscosity are further favorable properties to ensure quick ionic transport. For traditional LIBs, the use of aqueous solutions is not feasible because the electrode reactions occur out of the aqueous electrolyte stability window. Therefore, standard electrolytes composed of carbonate solvents (for example ethylene carbonate (EC), dimethyl carbonate (DMC), propylene carbonate (PC), ethyl methyl carbonate (EMC) or diethyl carbonate (DEC) and a lithium salt have emerged as suitable combinations. The use of further additives like vinylene carbonate (VC) to improve quality of the SEI or fluoro ethylene carbonate (FEC), to address both SEI formation and low temperature issues, is common practice. The positive effect of FEC – which itself has a melting point at room temperature -

on low-temperature stability is by now not completely understood, but is mainly associated to compositional and morphological changes of the SEI layer on the electrode [69]

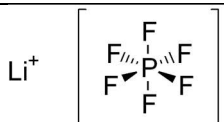
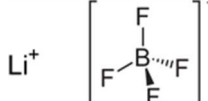
An overview of standardly used electrolyte carbonate solvents and their flash points is given in Table 3. The linear carbonates suffer from a low flash point around room temperature, which appears to be a potential risk concerning battery safety. In order to adjust cyclic electrolytes to standard operating temperatures of batteries, the addition of linear carbonates is necessary. Their low dielectric constant prevents linear carbonates to be used as single solvents.

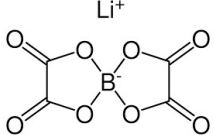
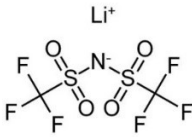
Table 3: Common electrolyte solvents in LIBs.

Compound	Structure	Dielectric constant $\epsilon$ [70]	Flash point
Ethylene carbonate		95.3	160 °C
Dimethyl carbonate		3.08	18 °C
Propylene carbonate		65.5	132 °C
Ethyl methyl carbonate		2.9	27 °C
Diethyl carbonate		2.82	24 °C

A small number of lithium salts is commercially used in electrolytes, which can be found in Table 4.

Table 4: Common electrolyte salts for LIBs.

Compound	Structure
Lithium hexafluorophosphate, LiPF <sub>6</sub>	Li <sup>+</sup> 
Lithium tetrafluoroborate, LiBF <sub>4</sub>	Li <sup>+</sup> 

Lithium bis (oxalato) borate, LiBOB	
Lithium bis (trifluoromethyl sulfonyl) imide, LiTFSI	

Within the last years, several groups have been intensively working on the preparation of water-based LIBs, mostly owed to the fact that the best-performing organic electrolyte salt  $\text{LiPF}_6$  is instable under ambient conditions. It easily decomposes to HF and  $\text{POF}_3$ , both harmful and volatile gases.

Developing water-based electrolytes used in LIBs, one has to keep in mind that water – and therefore aqueous electrolytes, too - have a small electrochemical stability window of 1.23 V. If now the electrodes intercalation potential is outside this stability window, water electrolysis takes places, thereby forming  $\text{H}_2$  and  $\text{O}_2$ . Keeping this fact in mind, the range of possible anode and cathode material gets limited to a small number within this stability window. Among others, the investigated LTO with 1.55 V vs  $\text{Li}^+/\text{Li}$  is beyond this window. Classically, lithium salts like  $\text{Li}_2\text{SO}_4$  or  $\text{LiNO}_3$  are used for aqueous LIBs, but a trend towards so-called “water-in-salt” (WISE) or “ether-in-salt” electrolytes can be observed.

By the use of a newly developed “WISE”-electrolyte  $(\text{Li}_4(\text{TEGDME})(\text{H}_2\text{O})_7)$ , prepared by the introduction of tetraethylene glycol dimethyl ether (TEGDME) in a concentrated aqueous electrolyte, Shang et al could prove that the electrochemical stability window can be increased even up to 4.2 V, thus enabling a broader variety in the choice of anode and cathode materials.

### 1.3.3 Inactive Materials

The inactive materials within a composite battery slurry are defined as any components besides the active material. The most common ones are the separator, conducting additives, current collectors, binders and – in a broader definition – also the interface to the current collector.

### 1.3.3.1 Separator

The main task of the separator is to prevent an electrical short circuit by keeping the positive and negative electrodes apart. On the other hand, it must enable the rapid transport of ionic charge carriers that are needed to complete the path during the passage of current [71] and is therefore a crucial component to maintain stable battery performance. A certain porosity and suitable thickness are crucial properties defining its transportation properties as well as the internal resistance. The separator's thickness needs to be carefully balanced between an ideal amount of electrolyte soaking on the one side and the assurance of mechanical stability on the other side.

Typically used kinds of separators are polyolefins like polyethylene (PE) or polypropylene (PP) – and combinations of those as well-known three-layer-separator composed of PP/PE/PP – or ceramics, both owning a good chemical stability. Those types of separators are the most common ones under use in LIBs. Several different improvements in terms of the incorporation of other advantageous materials have recently been performed.

The most crucial property for polyolefin-based binders is its shrinkage upon elevated temperatures, which is caused by stretching process during production. Shrinkage to a significant extent can lead to a short circuit within the battery cell and thereby completely leave out the original task of a separator, namely to separate anode and cathode materials from each other. To overcome this disadvantage, several attempts have been made to improve polyolefin-based separators. So it is possible to coat polyolefin-based separators by polymer binders with enhanced thermal resistance, like polyimide (PI) or phenolphthalein polyether ketone (PEK) to clearly increase their thermal stability [72].

Ceramics are another alternative to be used as separators owning much higher melting points and thereby not dealing with the shrinkage problem. The most common ones are  $\text{SiO}_2$  and  $\text{Al}_2\text{O}_3$ . Ceramic separators may suffer from a certain degree of brittleness, leading to a more complex processability compared with non-ceramic ones.

Further important properties of separators are its pore size, permeability for lithium ions and wettability as well as the abovementioned mechanical properties like thickness, strength, shrinkage and chemical stability. For reasons of biocompatibility, natural abundance, recyclability and an overall positive environmental impact, a closer look on alternatives for polyolefin separators is worth to mention:

Within the last years, several research groups have dealt with the topic of battery separator sustainability by focusing on preparation methods based on natural polymers like silk fibroin [73,74], poly(L-lactic acid) [75], alginates-based [76,77], bacterial cellulose nanofiber [78] and chitin nanofibers [79], just to name a few of them. These are promising innovations in terms of sustainability, but of course, there are still manifold issues to work on – the thermal stability of cellulose-based separators is by far not satisfactory and the preparation of very dense separators in the case of the large diameter of alginate-based materials will definitely arise further topics to cope with.

### 1.3.3.2 Conducting additives

The commonly used active materials (here: LTO and graphite for anode, LFP and LFMP for cathode) reveal a low electronic conductivity caused by a poor lithium diffusion at the interface in the range  $10^{-5}$  to  $10^{-13}$  S  $\text{cm}^{-1}$ .

*Table 5: Overview on typical active materials and their electronic conductivities.*

<b>Active material</b>	<b>Electronic conductivity [S/cm]</b>
LFP	$10^{-10} - 10^{-5}$ [80]
LFMP	$\sim 2 \cdot 10^{-8}$ [81]
LCO	$7 \cdot 10^{-5}$ [82]
LMO	$4 \cdot 10^{-11}$ [83]
LTO	$10^{-13}$ [84]
Artificial graphite	20-50 [85]

Hence, conductive additives are used to increase the electrical conductivity of the composite electrode without being involved in the electrochemical processes during charging and discharging. CB as the most common used conducting additive is increasing conductivity by filling the free space between the particles of active material and thereby forming a conducting network, where its big surface is of course advantageous. Some other materials like graphene [86], carbon nanotubes or conducting binders [87,88] are under investigation for their use as conducting additives. Although many additives besides CB show promising performance, they cannot outweigh its benefits like low cost, low weight and good availability.

The average mass fraction of conducting additives is in the range of 2.5-4 % for cathodic and 1-10 % for anodic applications.

#### 1.3.3.3 Current collector

The metal foils used to electrically connect the electrodes with an external circuit need to offer a good electrical conductivity combined with an excellent electrochemical stability within the operating potential window of the electrolyte. Typically, they are consisting of copper for the anode side and aluminum for the cathode side, which is a compromise of conductivity, availability and price. Copper is limited by the decomposition of HF on the cathodic side and dissolution into electrolyte on the anodic side [89], so its working potential is limited at a maximum of 3.5 V vs Li/Li<sup>+</sup> [90]. In contrast to copper, aluminum shows an extended voltage window up to 5 V vs Li/Li<sup>+</sup> [89].

It was found out that the weight percentage of current collectors in LIBs has reduced from 18% to 15% over the past two decades [91] arising from a reduction of thickness in order to increase the overall energy density of the battery.

At a first, maybe superficial glance, current collector foils show only little room for improvement in terms of efficiency and sustainability, but a closer look reveals that lots of research activity is taking place in terms of interphase modification, thickness adjustment and porosity optimization. In chapter4 *Improved current collector surfaces for LTO electrodes*, the influence of galvanic structured copper current collector will be discussed thoroughly.

#### 1.3.3.4 Binder

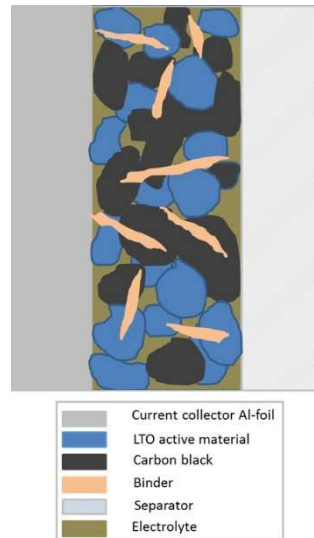


Figure 5: Cross-section scheme of electrode setup. Reprinted from ref. [50] under the terms of the Creative Commons CC-BY license.

One further essential inactive material is a polymeric binder. It enables a connection within the active material as well as a connection to the current collector, the maintenance of the electrodes physical structure and the formation of an electric network between the active material and carbon [92], as can be seen in Figure 5.

In order to be able to perform all of these tasks, binders must fulfil several requirements. The most important ones are a good electrochemical stability, good adhesion properties and a high strength.

A good electrochemical stability is crucial as the binder should not be reduced or oxidised at the very low or very high potentials depending on the voltage window. Furthermore, no corrosion or other electrochemical reactions should take place during cycling. Good adhesion properties are of course necessary to connect the particles with one another but also to enable a good and stable binding with the collector foil. The maintenance of the electrode structure and the formation of an electric network between active material and carbon can be included in the topic of adhesion properties [92]. With repeated charging and discharging, there should be no delamination of the battery slurry from the collector foil, which is then resulting in an elevated cycle life.

In terms of economic sustainability, binders should be soluble and processable in aqueous phase, but also be stable in the presence of lithium salts [93].

Different polymers are currently under use as binders for battery electrodes, where the most commonly used binder systems are described hereinafter.

What is apparent at first glance when considering the different polymeric structures given in Figure 6, is the great difference between the poly vinylidene difluoride (PVDF) and CMC and SA, respectively.

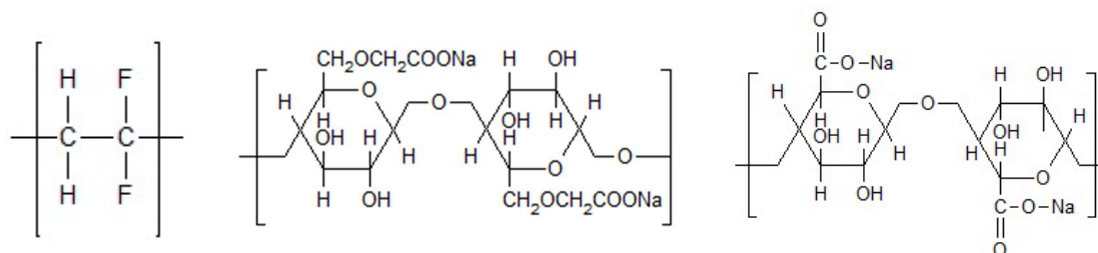


Figure 6: Evaluated binders, from left to right: Poly vinylidene difluoride (PVDF), Sodium carboxymethyl cellulose (Na-CMC) and Sodium alginate (SA).

SA, as a natural polysaccharide extracted from brown algae, contains carboxylic groups in each of the polymeric units [94]. Similarly, CMC is a cellulose derivate with carboxymethyl groups substituting some of the hydroxyl groups of cellulose [95]. These groups enable a great number of hydrogen bonds between the binder and the active electrode material, therefore favouring particle cohesion [96,97]. Its strong hydrophilicity and stable internal network structure are some more advantages of CMC [98]. Different studies have been performed on the swelling ability of SA. Kovalenko et al. found no detectable swelling of SA films, with its behavior similar to that of CMC binder occurring (in contrast to PVDF, which has a change in thickness of 17 % [49] up to 20 % [94]), whereas Samanta et al. claim a high swelling ability of SA hydrogels [99]. In contrast to the binders enabling hydrogen bonds, PVDF interacts with the active material via weak van der Waals forces, only on account of the –C-F functional group [100]. This fails to accommodate large changes in spacing between the particles, which was discovered both for LIBs and silicon anodes [101].

Another difference between the bio-based binders and PVDF is their thermal stability. Cuesta et al. measured the thermal stability of binders via thermogravimetric analysis (TGA) and found that all tested binders proved to be thermally stable at least up to 200 °C, which is roughly the onset temperature of the first decomposition stage of SA. CMC turned out to be slightly more stable with a decomposition onset temperature of 240 °C, whereas PVDF showed a much higher thermal stability up to 400 °C [97].

- N-methyl pyrrolidone-soluble binder systems

PVDF in general is the most commonly used binder in LIB and SIB technology. It is a thermoplastic polymer prepared by the radical polymerization of 1,1-difluoroethylene with excellent electrochemical and thermal stability. Furthermore, it shows good adhesion properties, a reversible capacity and provides reversibility, good wettability and a resistance to oxidation when processed in organic solvents. [102]. All of these advantages have to be put into perspective with the fact that PVDF needs to be dissolved in the organic solvent N-methyl pyrrolidone (NMP), which is known to be toxic and has to cope with several ecological drawbacks during processing. It was found out recently that PVDF can react with lithiated graphite and metal lithium at elevated temperatures by forming lithium fluoride and hydrogen on the electrode surface [103], which can be a drawback for applications under elevated temperatures. Its main drawback was already mentioned above and is listed in nearly every publication – it is the use of the abovementioned flammable and toxic solvent such as NMP [44,48,52,53,96,97,100,104–106],[107],[108]. The problematic use of the organic solvent is not only associated with its toxicity itself, but also points out further disadvantages, especially concerning process safety, the design of explosion-proof machinery, solvent recovery and safety measures for employees.

- Water-soluble binder (systems)

Poly tetrafluoro ethylene (PTFE) suspensions, carboxymethyl cellulose (CMC) and polyacrylic acid (PAA) are the most common aqueous binders for battery applications, but much more others are both under use and under research, as can be seen in the following paragraphs, focusing on LTO anode material:

Several studies have examined the performance of LTO as anode material for LIBs [41,42,48,52,53,95,109,110]. Only some of them concentrate on new water-soluble and environmentally friendly binders to be used for LTO anode material, despite the well-known and well-established CMC. A PEG-based binder was investigated by Tran et al., with the resulting LTO delivering 4.2 mAh cm<sup>-2</sup> at C/2 rate [53]. With the acrylic aqueous binder LA132 studied by Karuppiyah et al. [52], LTO delivered a total theoretical capacity of 175 mAh g<sup>-1</sup> at C/2 after cycling up to 20 C. Carvalho et al. investigated guar gum and pectin, which showed higher discharge capacities up to 5 C compared to a standard formulation using CMC [48]. De Giorgio et al. studied SA as a possible binder for LTO anodes displaying

high specific capacities in the range of 145 mAh g<sup>-1</sup> at 10 C [41]. No reports on the use of water-based PVDF binder for LTO electrodes have been found whereas many studies on cellulose-like binders, such as CMC and PVDF binder in organic solvent, have been performed.

The use of a novel PVDF binder in aqueous dispersion and without the need of NMP as solvent, is evaluated for different anode materials and further discussed in chapters 3.1

*Graphite with PVDF binder and 3.3 LTO with mixed binders: comparison between PVDF/SA and PVDF/CMC.* The combination of LTO with SA as binder was examined resulting in good mechanical and electrochemical stability up to 5C, but also found out that the combination showed a quick de-mixing of the materials in slurry [50], which was evaluated further in chapter 3.2 *LTO with sodium alginate binder.*

Each one of the binders presented in chapter 3 *Anode formulations with water-based binders* and shown in Figure 6 is eco-friendly, and the whole processing can be performed without the use of organic solvents. Though binders themselves are electrochemically inactive components, their chemical and physical nature definitely affects battery performance, especially capacity retention and cycle life [96]. The investigated binders are CMC, SA as well as a novel PVDF binder in aqueous dispersion, which has been introduced by Solvay Specialty Polymers, Italy, and has recently been investigated as a binder for graphite anodes by our group [49].

The replacement of synthetic and fluoride-containing binders like PVDF or PTFE by natural polymers showing properties like sustainability, biodegradability and low or no toxicity, will be a major future task for technical applications.

- Influence of polymeric structure on binder properties

For polymers, the following hierarchical concepts are often used to describe the molecular architecture: composition (identity and quantity of elements), constitution (connectivity), configuration (stereo-chemical arrangement) as well as conformation (spatial arrangement). Polymers consisting of a backbone with substituents can show different isomeric structures when changing their position. This leads to the concept of tacticity, where one can distinguish between isotactic, syndiotactic and atactic polymers. Isotactic

polymers are characterised by all side groups on one side of the chain, whereas syndiotactic polymers have their side groups on alternating sides. Atactic polymers show a statistical distribution of their side groups, as can be seen in Figure 7:

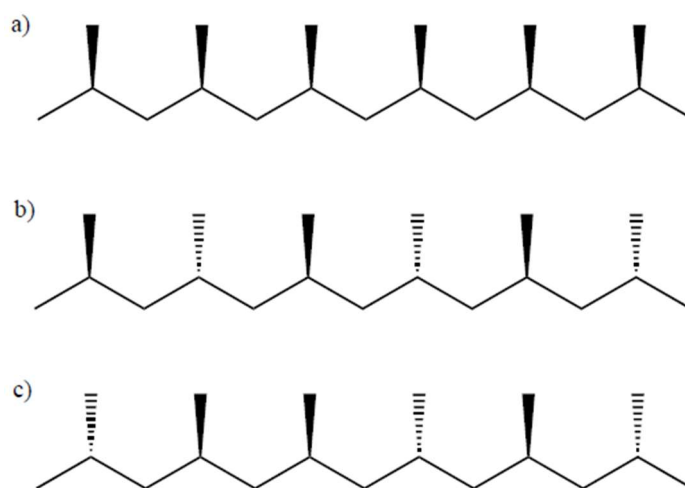


Figure 7: a) isotactic, b) syndiotactic and c) atactic polymer.

Tacticity of a polymer has a big influence on its spatial structure as well as the size of the side groups, stiffness of the chain and its degree of branching.

A further interesting structural property is the crystallinity of a polymer, whose influence is discussed in chapter 3.1.1 *Swelling and capacitance measurement*. According to chain constitution, branching, tacticity and others, a polymer is able to crystallise upon slow cooling down of the melt. Here, ordered regions are formed where chain segments are arranged regularly. In most cases, polymers crystallise neither completely nor perfectly but give semi crystalline materials, containing crystalline regions separated by adjacent amorphous phases. The fraction of crystalline material is called the degree of crystallinity and is an important parameter of semi crystalline materials [111]. In contrast to crystalline modifications, amorphous morphologies show a randomly arranged molecular structure, as can be compared to *spaghetti* [112] which is illustrated in Figure 8. Depending on interaction of the properties like tacticity, side groups and degree of branching, crystallization can be hindered or promoted. The more uniform the polymer structure, the easier it is to crystallize, where ordered regions need to be packed in a regular way. So polymers with iso- or syndiotactic structure are more likely to crystallize than ones with atactic structure. The degree of crystallinity also has an important influence on density and many rheological and mechanical properties.

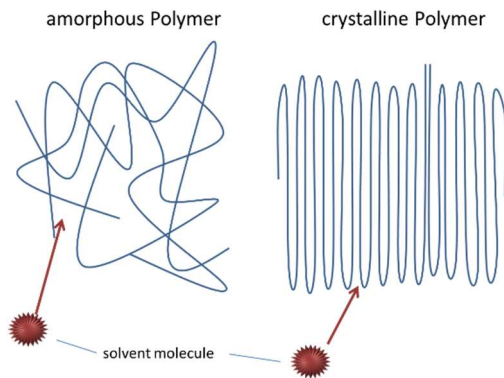


Figure 8: Schematic drawing of chain structure of amorphous (left) and crystalline (right) polymer. Reprinted from ref. [49] under the terms of the Creative Commons CC-BY license.

### 1.3.4 Processing

In terms of processing, there are several points that can increase sustainability during battery electrode preparation. In general, its components like active material, binder(s) and conducting additives are mixed in a solvent, following defined, sequential steps as illustrated in Figure 9. The mixing process is followed by a coating step, where the slurry is coated upon a substrate foil. Afterwards, the solvent is evaporated and the resulting, dry coating upon current collector foil is named electrode.

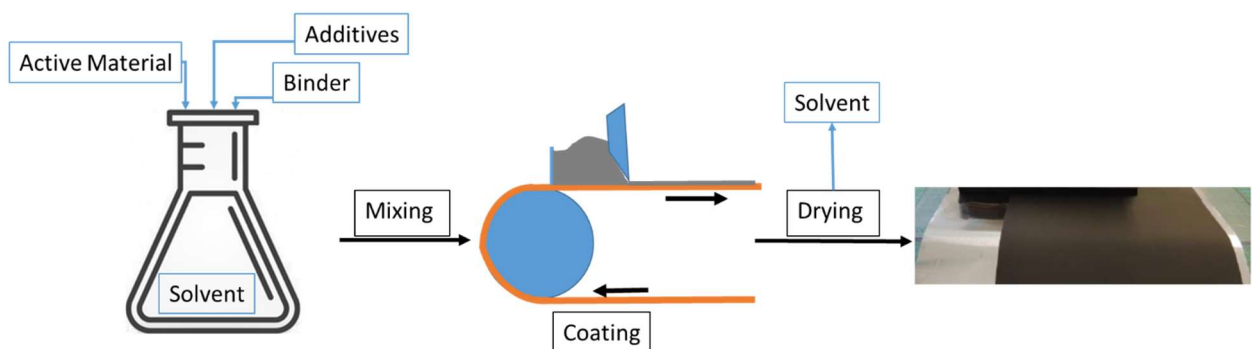


Figure 9: Processing steps for preparation of LIB electrode. Reprinted from [45] under the terms of the Creative Commons CC-BY license.

#### 1.3.4.1 Dry mixing and dispersing

As a first step of electrode processing, the active material needs to be blended with binder, conducting additives and the solvent. A homogeneous mixture with a good connection of the active material with conducting additives and polymeric binder is decisive for all subsequent steps and the resulting both mechanical and electrochemical properties. Depending on the choice of active material and solvent, starting point is whether the dry mixing of powders (for example, NMC cathode material with CB) or the preparation of a stock solution of polymeric binder in the solvent (for example, LTO anode material in water). Especially for cathode with low intrinsic conductivity, the active materials electrical connection is thereby optimized and furthermore, a variety of additional connectivity pathways is created. This is achieved by simultaneous de-agglomeration, grinding and dispersing of CB [113]. Building a framework is also the goal concerning the preparation of a binder stock solution in the desired solvent. These systems can be classified in water-based and (organic) solvent-based systems. For reasons of sustainability, water-based ones are the ones mainly addressed in this thesis. A uniform binder distribution within the electrode sheet is of enormous importance thus ensuring the binding strength of electrode powders and the adhesion strength between electrode sheet and current collector [114]. For the preparation of LTO slurries, the polymeric binder was dissolved in water under gentle stirring and heating up to a maximum of 40 °C. The addition of further materials (active material, CB as conductive additive, second binder) is then performed in a high speed dissolver. As some active materials are shear-sensitive and may disintegrate at application of high stresses, the most feasible way for those materials is a deagglomeration of CB at high energy input followed by addition and gentle processing of these materials. The bad incorporation of CB is one of the most common causes for typical failures like a significant capacity fading in latter electrochemical measurements.

A defined adjustment of slurry viscosity is crucial for performing an efficient subsequent coating step. These properties are of enormous importance and are considered and further highlighted in chapter 3.2.4 *Rheological properties of LTO-SA slurries* and 3.3.3 *Rheological measurements* .

### 1.3.4.2 Coating

To perform the coating step, the electrode slurry is placed upon the current collector foil at a defined thickness, ensuring the application of a continuous battery coating. This processing step is visualized in Figure 10, where the current collector is lead through the coating machine and the slurry is placed on top of it. By leaving a small gap followed by a doctor blade, a defined amount of battery slurry can pass the way further to the heating step. The amount is defined by the gap left by the doctor blade and is typically adjusted at 50 – 200  $\mu\text{m}$ . Several other parameters like belt speed or slurry viscosity are critical and need to be considered here. The aforementioned preparation of the slurry can only render its full contribution when the slurry is absolutely homogeneous and big particles are completely deagglomerated, otherwise getting entangled in the coating gap leading to scratches or cavities in the electrode sheet.

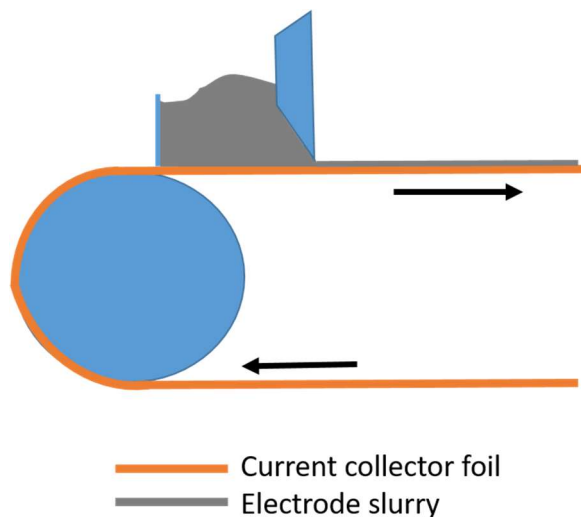


Figure 10: Scheme on continuous coating of battery slurry upon current collector foil.

Figure 10 depicts the typical doctor blade coating process, which is also the chosen method for electrode preparation, as described in chapters 3.1 *Graphite with PVDF binder* and 4 *Improved current collector surfaces for LTO electrodes*. A manual doctor knife process based on the same principle with a squeegee box was used for electrode preparation in chapters 3.2 *LTO with sodium alginate binder* and 3.3 *LTO with mixed binders: comparison between PVDF/SA and PVDF/CMC*.

Several other techniques are in use, for example slot-die or comma bar coating. Schällicke et al. proposed a novel, solvent-free manufacturing procedure including fluidization and transfer

of powder mixture upon the current collector by inducing a high voltage [115], thus being able to work independent from solvents.

#### 1.3.4.3 Drying

Electrode drying is conducted directly after the coating step with the drying temperature depending on the used solvent in order to completely evaporate it. So typical drying temperatures are ranging from 60 °C (acetone with boiling point of 56 °C as solvent) up to 150 °C (NMP as solvent). Different drying procedures are utilized, aiming a uniform and complete evaporation of the solvent through the electrode pores. The most common one is the application of heat from the bottom thus ensuring a complete drying by convection and conduction. Drying rate and heat transfer coefficients are the parameters of highest interest. Crucial step during drying is the exhaustive removal of solvent, which is most critical for water-based electrodes. It is commonly known that during drying step, diffusion processes of binder and CB are taking place, thereby affecting electrode morphology.

#### 1.3.4.4 Calandering

The ripressing of electrodes after drying is an optional step in electrode preparation, where cavities are compressed. Here, a maximum packing density of the active materials is pursued. An adequate porosity between 20 and 30 % is needed to ensure fast ionic transport in the electrolyte [116]. Calandering can be advantageous if any coating failures like an uneven distribution are occurring, but it will not be able to completely eliminate, but rather mitigate them [117].

#### 1.3.4.5 Combination to half-cell or full cell

To be able to analyze thoroughly anode or cathode parameters, the preparation of so-called half-cells is an indispensable procedure. In this set-up, as described in Figure 11, the prepared working electrode (WE) is combined with metal lithium as both reference electrode (RE) and counter electrode (CE).

The potential at the WE is set and the resulting potential at the CE is measured. A RE is included in three-electrode arrangement to ensure a suitable current distribution between the electrodes. With the use of a CE comprising of metal lithium, an unlimited amount of lithium is provided and can thereby establish the needed currents for material investigation and give detailed insights into relevant properties of the WE, such as its rate capability and capacity.

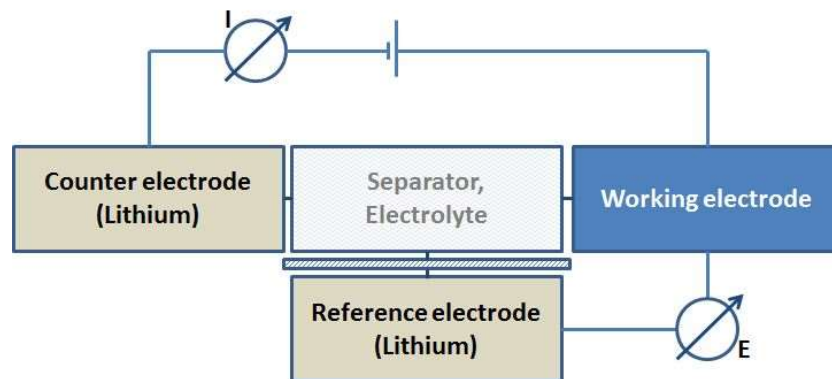


Figure 11: Schematic set-up of Swagelok (R) three-electrode arrangement. Reprinted from ref. [49] under the terms of the Creative Commons CC-BY license.

In practice, the assembly of a half cell is taking place in a glovebox filled with inert gas and is described in a more detailed way in chapter 2 *Materials and methods*.

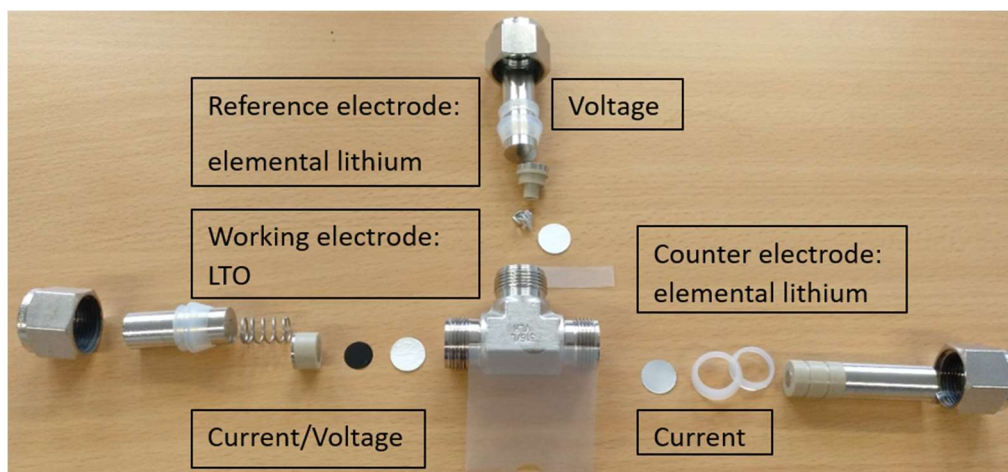


Figure 12: Set-up of Swagelok (R) three-electrode arrangement. Reprinted from ref. [29] under the terms of the Creative Commons CC-BY license.

Full cells, comprising of several stacks of anode, cathode, separator and electrolyte, are what is originally meant by the term “lithium ion battery”. In industrial scale, the solid materials are wound upon round or prismatic cores or cut into single pieces and stacked upon each other.

Industrial LIB cells are sold in three different housing types: round cells (welding of electrodes and separator upon round core), prismatic cells (welding upon prismatic core) and pouch- or coffee bag-cells (stacked components in flexible envelop).

For laboratory scale, the latter preparation technique was used, being able to work with small amounts of material on the one hand and being flexible with the use of different components on the other hand.

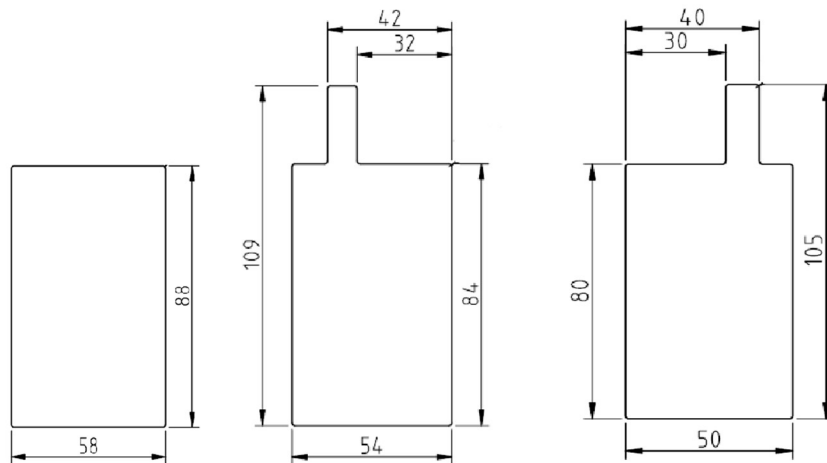


Figure 13: Dimensions of separator (left), anode (middle) and cathode (right) for lab-scale cell preparation.

The electrode sheets, prepared in full cells as described in chapter 3.1 *Graphite with PVDF binder*, are cut into single electrodes as well as the separator with a handheld punch. Dimensions are described in Figure 13. The separator, of course, is owning the largest surface, as to efficiently separate anode from cathode. The anode size is bigger than cathode to ensure that all lithium ions originating from the cathode can be placed within the anode host structure. The prepared cell is placed in a laminator, where the components are pressed together under application of both elevated temperature and pressure. In a next step, the cell is equipped with welding tabs and closed in a flexible pouch foil, followed by electrolyte filling in a glovebox.

#### 1.3.4.6 Calculation of electrode capacity

LIBs are charged in constant current/constant voltage (CC-CV) mode where the amount of current is limited to a defined level until the cell reaches a defined maximum charging voltage level. In the constant voltage step, the charging voltage is held constant and the charging current decreased over time until the cell is fully charged. With this charging system, a rather fast charging without the risk of over-charging can be maintained. Because of its simplicity and efficiency, this is the most common charging profile for LIBs.

An integration of the electrical current flow  $I$  over time leads to the amount of charge according

$$\Delta Q = I \cdot \Delta t \quad \text{Equation 1-4}$$

The amount of charge  $\Delta Q$  on the used mass of active material  $m$  then allows calculation of the specific capacity  $C_{spec}$  in  $\text{mAh g}^{-1}$ :

$$C_{spec} = \frac{\Delta Q_{max}}{m} \quad \text{Equation 1-5}$$

To be able to measure the maximum usable capacity, the step called formation is indispensable: few (two or three) cycles of formation are the beginning of every test procedure of a freshly prepared cell. Here, the cell is charged and discharged at very low C-rate. Calculation of appropriate C-rate is at first depending on the theoretical specific capacity of the material and in further steps done on the basis of discharge capacity after the very first formation.

#### 1.3.5 End-of-Life/Second-Life

By now, no standard approaches have been developed to deal with battery waste in relevant amounts according to the large volumes being proposed when looking at the massively increasing number of EVs. To prevent tons of accumulating waste batteries, one has to think in advance about possible strategies concerning the end of life of batteries.

To ensure a maximum efficiency of batteries, several strategies have emerged concerning recycling strategies on the one hand and so-called "second-life" use on the other.

With increasing amounts of produced batteries, the main cost factor is shifted from processing to raw materials. Raw material prices are strongly influenced by the worldwide demand, which is assumed to highly increase with continued expansion of transport electrification. This potential price increase can be cushioned at least to a certain amount by a fast implementation of a circular economy and sustainable recycling solutions.

#### 1.3.5.1 Recycling of batteries

Due to the fact that LIB contain both precious and harmful substances and, also in terms of economic efficiency, a suitable recycling strategy is indispensable. One further fact complicating the recycling issue is both the big variety of possible active materials combination and the plenty of different battery housings. Typically, commercially available LIBs are to be found in three different forms: cylindrical cell (formats like 18650 or 26650, for example), prismatic cell or pouch cell (the so-called coffee-bag). This variety of formats and sizes makes small- and medium scale automated battery recycling a challenging task, as different disassembling steps have to be performed. After a first, physical process including dismantling, crushing, separation, washing and further treatment, a chemical process is initiated [118], where the hydrometallurgical process is the most common one. During this chemical process, precious metals like copper, cobalt, lithium and manganese can be recovered – at least partly, depending on the used process. The key step for the recovery of valuable metals is leaching, where metals in the cathode material are processed to ions in solution which are subsequently recovered by precipitation, solvent extraction or electrolytic decomposition [119]. Typically, inorganic and organic acids or alkali or bacteria solutions act as leaching media. [119].

#### 1.3.5.2 Second-life strategies

The production of LIBs is associated with high costs, especially when being compared to other energy sources. Re-using of EV batteries after reaching a critical capacity (conventionally, in the range of about 80 % of the initial capacity) for stationary applications like home- or off-grid-storage systems is a very cheap way to increase the lifetime of a battery and thereby reduce its ecologic footprint. Even with a reduced capacity, the batteries are still able to store

and deliver energy – in the optimum case for any kind of application, where energy density and size are of subordinate interest.

With an increasing amount of EV on the streets, an emerging need for suitable charging infrastructure was identified. For an economical operation of charging stations, one can rather add renewable energy sources such as photovoltaics as auxiliary electricity sources in fast-charging stations to reduce overall power consumption from the grid. [120]. Another possibility to improve charging station efficiency is the addition of a battery storage system which is even cheaper when second life batteries are used [120].

In order to re-use LIBs and ensure their safe operation, one has to perform a thorough analysis of battery performance and their State of Health (SOH), where electrochemical models and analyses are used to simulate internal battery properties [121] [122].

## 1.4 Sodium Ion Batteries

Due to an ongoing increase in LIB production capacities combined with a high demand, a realistic estimation of the future cost development for LIB electrode materials is nearly impossible. Both suppliers and customers are thereby left with the risks of demand-supply mismatch and the increasingly environmental and social challenges associated with the mass production of LIBs [1,123]. Sodium is the sixth most abundant element on earth, appearing both in the earth crust and oceans at a high percentage.

Sodium ion batteries (SIB) seem to be an alternative at least for stationary applications and have numerous advantages over lithium-based systems:

- they are based on a similar working principle with well-known set-up
- they consist of significantly cheaper and more abundant materials
- they are associated with less critical sourcing

In general, the LIB processing and set-up can quite easily be adopted for SIB technology, but the equivalent concept is combined with several varying chemical properties, as a given host structure will interact in another way depending on the intercalated material [124]. A different ionic radius ( $r = 102 \text{ pm}$ , coordination number (CN) = 6 for  $\text{Na}^+$  and  $r = 59 \text{ pm}$ , CN = 4 for  $\text{Li}^+$ ) and different polarizability highly affect the phase behavior and diffusion properties [124]. As

the sodium ion is both bigger and heavier compared to the lithium ion, a sodium-based battery is not expected to reach the LIB energy density, but can act as a suitable alternative for stationary applications. Nevertheless, the basic mechanic set-up like coating techniques, collector foils and assembly are comparable or even simpler and can be adopted in an easier way than for a completely different technology, like metal/air, flow battery systems or fuel-cell technologies. A variety of different active materials is currently under research for sodium ion batteries. Comparable to LIB technology, a stable framework is necessary to reversibly intercalate sodium ions into the host lattice. Typical active materials are partly adopted from lithium-ion technology and partly developed for sodium ion technologies. From a sustainability perspective, the abundance of raw materials is one of the biggest issue and the most significant disadvantage of lithium ion technology.

### 1.5 Strategies to improve economic sustainability of sodium ion batteries

Parallel to the development of LIBs in the 1970s and 1980s, SIBs were intensively studied, but lost in the race for high energy density and got somehow forgotten. Nevertheless, within the last years and facing towards a growing scarcity of LIB raw materials, research and commercialization of SIBs are re-emerging fastly.

Hirsh et al. depicted raw material price fluctuations and found out that the prices of  $\text{Na}_2\text{CO}_3$  as main educt are approximately two orders of magnitude lower than its lithium counterparts, with  $\text{Li}_2\text{CO}_3$  at \$13 000 per metric ton compared to  $\text{Na}_2\text{CO}_3$  at \$150 per metric ton in 2020 [125]. The dynamic characteristics of these fluctuations are further emphasized by the fact that  $\text{Li}_2\text{CO}_3$  prices rose up to \$ 26 000 in September 2021 [126].

At a first glance, sodium ion batteries seem as the embodiment of sustainability, which is for sure true when relating it to LIB technology, as nearly all electrode materials are based on naturally high abundant, non-toxic resources and all this at economically feasible prices. Same as for LIB, most valuable parts of a SIB are its cathode and anode materials. Nevertheless, one also has to think about cell components besides electrode materials, like current collector and housing and from a sustainable point of view, battery design should be thought the different way around: starting from a highly abundant technology with the possibility to be recycled to a high degree with less possible release of waste.

As these topics would go beyond the scope of this thesis, I am solely concentrating on electrode materials and current collectors.

### 1.5.1 Active Materials

#### 1.5.1.1 Cathode active materials

Comparable to LIBs, cathode materials need to be able to stably and reversibly insert sodium ions. Several materials and combinations have emerged owning good sodium-ion intercalation properties and one group of them has gained a lot of attention, which are sodium super ionic conductors (NASICON), based on compounds with the general chemical formula  $\text{Na}_y\text{MM}'(\text{XO}_4)_3$  with ( $\text{M}=\text{V}, \text{Ti}, \text{Fe}, \text{Tr}, \text{or Nb etc}; \text{X}=\text{P or S}, x=0-4$ ) [127]. Their framework structure is constructed by corner-shared groups, providing pronounced  $\text{Na}^+$  diffusion channels which can be used as cathodes:  $\text{Na}_3\text{V}_2(\text{PO}_4)_3$ ,  $\text{Na}_3\text{V}_2(\text{PO}_4)_2\text{F}_3$ ,  $\text{Na}_{1.5}\text{VPO}_4\text{F}_{0.5}$ ,  $\text{Na}_2\text{FeTi}(\text{PO}_4)_3$ , and  $\text{Fe}_2(\text{MoO}_4)_3$  have been well investigated [127]. Further typically used cathode materials are layered metal oxides with the formula  $\text{Na}_x\text{MO}_2$  ( $\text{M} = \text{Fe}, \text{Co}, \text{Mn}, \text{Ni}, \text{Cu}, \dots$ ), polyanion-type materials [128] and prussian blue analogues [129]. More and more, Prussian white – being the fully reduced and sodiated form of Prussian blue – is emerging as another promising cathode material for SIBs. Cathode materials are often associated with a high fading rate, as the large expansion of Na layers and the co-insertion of electrolyte solvents induce irreversible structural changes within the material [130].

#### 1.5.1.2 Anode active materials

Similar to LIB anodes, a host structure with preferable low charging/discharging voltage is required for SIB anodes. Therefore, active materials for SIBs are partly adopted and modified from lithium ion technology, as for example  $\text{Li}_4\text{Ti}_5\text{O}_{12}$ ,  $\text{Na}_4\text{Ti}_5\text{O}_{12}$  or  $\text{Na}_3\text{LiTi}_5\text{O}_{12}$  [131]. Graphite as standardly-used LIB anode material is not feasible for SIBs as the sodium ion is too large to fit into its layered structure. However, other carbon-containing components like expanded graphite or hard carbons can be utilized as anode materials for SIBs.

In addition to this already existing alternatives, typical NASICON materials analogue to those explained in section 1.5.1.1 *Cathode active materials* used as anodes are  $\text{NaTi}_2(\text{PO}_4)_3$ ,  $\text{NaZr}_2(\text{PO}_4)_3$ ,  $\text{NaV}_2(\text{PO}_4)_3$  and  $\text{Na}_3\text{MnTi}(\text{PO}_4)_3$  [127].

To increase the batteries energy density, a maximum voltage gap should lie between anode and cathode materials.

All of these anode (and cathode, respectively) materials are free of rare earth elements as lithium, cobalt or nickel and can thereby be categorized as suitable and sustainable alternative to LIB systems. For a closer look and detailed life-cycle analysis of these materials, there are by now not enough data available to be able to compare critical factors like rate capability, cycle life and its end-of-life in terms of recyclability.

## 1.5.2 Electrolyte

Both non-aqueous and aqueous electrolytes are reported for sodium ion batteries, resulting in different stabilities and application windows. Non-aqueous electrolytes are mostly based on the use of  $\text{NaPF}_6$  equivalently to  $\text{LiPF}_6$  in LIBs as salt and vary from propylene carbonate (PC), DMC, EC [132,133] and trimethyl phosphate (TMP) to rather unknown ones like  $\gamma$ -butyrolactone and  $\gamma$ -valerolactone [132]. Several other sodium salts are also under use for SIBs, for example  $\text{NaClO}_4$ ,  $\text{NaBF}_4$ , sodium bis(trifluoromethanesulfonyl)imide (NaTFSI) or sodium fluoromethanesulfonylimide (NaFSI), just to name a few of them. As long as the electrochemical stability range is not exceeded, high energy densities can be reached with non-aqueous electrolytes.

Having a closer look at aqueous electrolytes for SIBs, one can clearly see that they are limited by the electrochemical stability window of water at 1.23 V. Newer research is focusing on so-called “water-in-salt” (WiSE) electrolytes thereby reaching increased voltage windows in the range of 2.5 V – analogue to water-based electrolytes for LIB, as already discussed in chapter 1.3.2 Electrolyte. Some kinds of those WiSE electrolytes are based on sodium trifluoromethane sulfonate ( $\text{NaCF}_3\text{SO}_3$ , NaOTF) or lithium bis(trifluoromethanesulfonyl)imide (LiTFSI) [134], several others are currently under research. Han et al even proposed a fluoride-free dual cation highly concentrated electrolyte containing potassium acetate (KAc) and

sodium acetate (NaAc), leading to a Na<sup>+</sup> conducting SEI and being able to expand the useable electrochemical window up to 2.5 V [135]. These findings clearly indicate what has to be done to further go into the direction of environmentally-friendly, water-based electrolytes for application in SIBs.

### 1.5.3 Inactive Materials

Comparable to LIBs, inactive materials for SIBs should share the same basically required chemical and/or mechanical properties.

#### 1.5.3.1 Separators

Separator requirements are rather similar to those for LIBs; its main task is to ensure a physical barrier between the two electrodes thereby avoiding short circuit. Its basic requirements like a good thermal stability, suitable pore size and electrochemical stability are assumed. Commercial polyethylene (PE) and polypropylene (PP) separators, as used for LIBs, are also widely used for SIBs, mainly due to their good electrochemical stability and mechanical strength [136]. Unfortunately, they show a bad wettability performance for SIB electrolytes with high viscosity solvents, which is subsequently leading to increased interface resistance and reduced ion transfer rate [137]. These high viscosity solvents require both an increased chemical stability and improved wettability [137]. Wettability issue of this kind of separators was tried to overcome by a surface modification with nanoparticles like TiO<sub>2</sub>, SiO<sub>2</sub> or Al<sub>2</sub>O<sub>3</sub>, but this subsequently lowered power rate by an additional interfacial resistance [136]. Newer research is focusing on naturally abundant materials as a basis for separator development, namely cellulose derivatives like CMC, hydroxyethyl cellulose (HEC), agarose-PVA or cellulose-acetate based ones [136,138,139].

Furthermore and also determined by elevated sustainability of SIBs over LIBs, a certain degree of eco-friendliness concerning separator raw materials is required. Additionally, and for the sake of economic efficiency, its cost should not surpass prices for standard LIB separators.

### 1.5.3.2 Conducting additives

Complementary to LIB technology, particles with small size and high electronic conductivity are required as additives to enhance the overall bad conductivity of anode and cathode active materials. Graphitic materials with low crystallinity like CB have emerged as the main conducting additives not only for LIBs but also for SIBs. Depending on anodic and cathodic properties, some others like graphene, carbon nanotubes, copper or  $Ti_2P$  can be incorporated or/and added as conducting additives [140].

### 1.5.3.3 Current collectors

Aluminium and copper as the most widely used current collectors for LIBs have attracted much interest as for the use in SIBs. Aluminium, being the cheaper one, is at first sight the medium of choice there. It is known to form alloys with lithium at potential below 0.1 V vs  $Li/Li^+$ , therefore it cannot be used on the anodic side of LIBs. This fact is indicating its suitability for SIBs, as sodium does not form alloys with aluminium, or at least at much lower potential of around 0.01 V vs  $Na/Na^+$  [141].

Depending on the used electrolyte, electrolytic solutions of metallic salts like  $NaClO_4$  or  $NaPF_6$  are not able to protect aluminium from oxidative dissolution, leading to poor cycling stability [142]. This dissolution reaction is not yet fully understood, but in most cases the formation of a protective layer is suggested, also being dependent on the salt concentration [142].

Going one step ahead, one can also claim stainless steel as current collector. It is known from LIB technology to suffer from different dissolution processes due to its complex composition including elements such as chromium and nickel [143]. Depending on a good combination of active materials and electrolytes, its application within SIBs would be feasible.

### 1.5.3.4 Binders

Same as for LIB technology, binders are used to combine active materials with conductive additives and current collectors. They are generally electrochemically inactive and insulating,

thus reducing the overall low energy density of SIBs [144]. Therefore, some studies are concentrating on the preparation of binder-free SIBs [144].

#### 1.5.4 Processing

SIBs can be processed quite similarly to LIBs. Due to the fact that a significantly lower energy density and a lack of mechanical stability requires a higher electrode thicknesses, average thicknesses of 2-4 mm for SIB electrodes are common practice. Compared to a medium electrode thickness of 50-200  $\mu\text{m}$  for LIB, it is clear that not all technologies and approaches can directly be adopted.

#### 1.5.5 End-of-Life/Second-Life

Due to the young commercialization period of SIBs, there are by now no concepts available concerning its end-of-life or second-life use. Recycling processes may be easier in contrast to LIB systems, but though a differentiation between water-based and solvent-based systems has to be implemented. Just as for processing, water-based systems are lacking the use of volatile and/or hazardous solvents and do therefore not need that variety for downstream processes.

#### 1.6 Characterization techniques

There is a great variety of different battery characterization techniques. Besides structural characterization obtained via scanning electron microscopy (SEM), X-ray diffraction (XRD) or spectroscopic methods, electrochemical characterization techniques are the most reasonable when examining electrochemical systems.

### 1.6.1 Cycling tests

The preparation of charge/discharge curves, where voltage and current are plotted versus time, is one possible characterization tool in battery development, thereby being able to evaluate specific cell properties. Charging of a cell is performed by a constant current (CC) phase followed by a constant voltage step, whereas discharging is only taking place in CC mode, which was performed for all tested cells. Two different types of tests are common, namely power tests, evaluating the cells properties during charging and discharging at defined C-rate(s) and a rate test method, where the cell is cycled at one defined C-rate for many (several hundred up to even thousand) cycles. By plotting voltage and current versus time, voltage limits and cycle times are quite clear at first sight. Additionally, capacity, CEf and several more parameters can be calculated from these data. Power tests are plotted in a form of charge or discharge capacity versus cycle number at same or different C-rates. Thereby, information like a materials capability to high currents can easily be extracted.

### 1.6.2 Cyclovoltammetric measurements

Cyclic voltammetry (CyV) is an electrochemical technique combining voltage - which is applied to a cell - and amperometry by measuring a current response of the investigated cell. By the help of CyV it is possible to detect the potential at which oxidation or reduction reactions take place and if a chemical reaction is reversible or not [145]. Scanning in both directions allows the interpretation of electrochemical behavior of any species which are generated at the electrodes. One of the most important parameters in CyV is the scan rate, which allows a more distinct observation of oxidation or reduction processes.

### 1.6.3 Electrochemical impedance spectroscopy

Electrochemical impedance spectroscopy (EIS) is a powerful tool to investigate physical and chemical processes within an electrochemical cell. It is based on the model of equivalent circuits describing the complex behavior of real world properties, like charge transfer or diffusion. The application of an AC potential results in a phase-shifted current response which can then be written as follows:

$$Z = \frac{E(t)}{I(t)} = \frac{|E| \sin(\omega t)}{|I| \sin(\omega t + \theta)} = |Z| \frac{\sin(\omega t)}{\sin(\omega t + \theta)} \quad \text{Equation 1-6}$$

With the help of Eulers formula, equation 1-6 can be re-written by using complex numbers leading to the following formula:

$$Z = |Z|e^{j\theta} = \frac{|E|e^{j\omega t}}{|I|e^{j\omega t + \theta}} \quad \text{Equation 1-7}$$

with imaginary number  $j$ , phase angle  $\theta$ , voltage signal amplitude  $|E|$  and current response amplitude  $|I|$ .

#### 1.6.4 Capacitance measurement

Tests to evaluate the swelling ability of electrodes are performed by a capacitive displacement measurement method.

This technique is based on the simple model of an ideal plate capacitor: a sensing electrode is placed opposite to a conducting object, thus forming a plate capacitor. The distance between the sensor and sample electrode is directly deduced from an impedance measurement of the capacitor, since the impedance of a plate capacitor is directly proportional to distance between its electrodes.

The capacitance  $C$  of a plate capacitor is given by

$$C = \varepsilon \frac{A}{d} \quad \text{Equation 1-8}$$

where

$$\varepsilon = \varepsilon_0 \varepsilon_r \quad \text{Equation 1-9}$$

is the permittivity of the material between the plates, composed of the permittivity of vacuum  $\varepsilon_0$  and the relative permittivity of the material  $\varepsilon_r$ .  $A$  is the area of the electrode and  $d$  is the distance of the electrode to the sensor. The impedance of the system is measured in order to determine the capacitance of the sample. The magnitude of the impedance of an ideal plate capacitor is

$$Z = \frac{U}{I} = \frac{1}{\omega C} \quad \text{Equation 1-10}$$

where  $I$  and  $\omega$  are the magnitude and the angular frequency of the applied current and  $U$  is the magnitude of the voltage drop across the capacitor. The distance  $d$  can now be obtained by combining the above equations:

$$d = \varepsilon\omega A \frac{U}{I} \quad \text{Equation 1-11}$$

Thus, the distance is directly proportional to the sensor voltage, if the current through the system is held constant. The above theory is based on the assumption that the plate capacitor is ideal. This means that the electric field between its plates is absolutely homogeneous.

Guard electrode can be used to achieve a homogeneous field distribution in a real sensor. The guard electrode surrounds the sensing electrode and maintains the same potential. Therefore, no edge effects occur at the boundary between the two electrodes and the electric field lines are straight across the whole electrode area [146]. A scheme of the set-up can be seen in Figure 14. The coated copper foil (in our experiments is the graphite anode) is placed upon a seating and closed with a PE foil to hinder evaporation of the solvent during the test procedure. A hole in the foil allows the syringe to cast a drop of solvent directly upon the electrode surface and is analysed by the capacitance sensor. The syringe is connected to a pump so a defined amount of solvent can be placed on the coating within a defined time span. The capacitance sensor is placed 1 cm next to the syringe tip and measures the change in thickness of the coating with time.

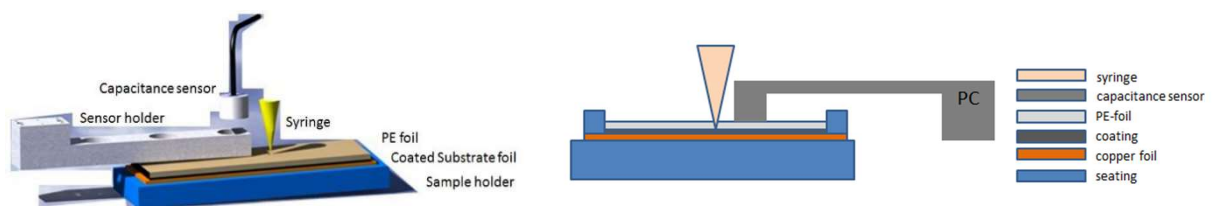


Figure 14: Schematic set-up of capacitance measurement. Reprinted from ref. [49] under the terms of the Creative Commons CC-BY license.

### 1.6.5 Rheological properties

Flow characteristics of a slurry are essential properties for its ability to be processed in an optimum way. It is crucial mainly for the coating step, where the prepared paste is applied upon the current collector foil.

Rheological properties are evaluated in forms of a viscosity test and frequency sweep test with a rheometer. Double-gap geometry is used, where the measurement capability at low stresses is higher than for standard cylinder geometry.

Rheology can describe flow behavior and deformation of fluids depending on their physical properties. Shear stress  $\tau$  is defined as

$$\tau = \frac{F}{A} \quad \text{Equation 1-12}$$

representing a specific shear force  $F$  applied on the area  $A$ .

Shear rate  $\dot{\gamma}$  is defined as

$$\dot{\gamma} = \frac{v}{h} \quad \text{Equation 1-13}$$

with velocity  $v$  and shear gap  $h$ .

Flow curves are typically prepared by plotting viscosity versus shear rate, as can be seen in Figure 15, representing three different, easily distinguishable kinds of fluids.

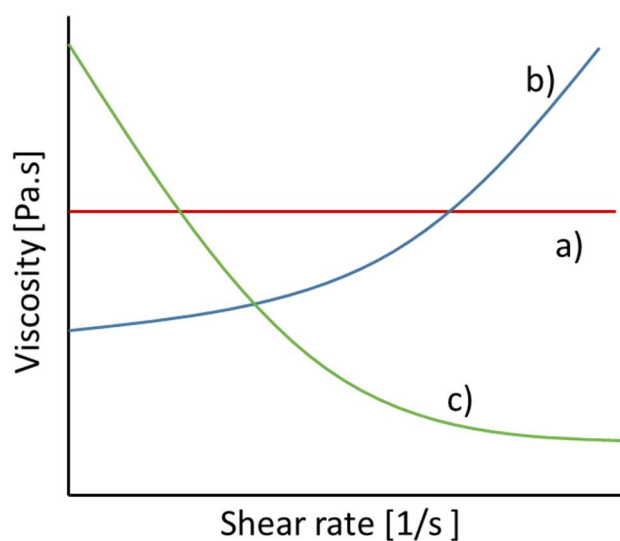


Figure 15: Viscosity curve for different kinds of fluids, a) ideal viscous, b) shear-thinning and c) shear-thickening.

Storage and loss modulus are some further properties of interest, evaluating the amount of stored (storage modulus,  $G'$ ) or dissipated (loss modulus,  $G''$ ) energy within the material. Mechanical energy can be stored in forms of an elastic deformation, leading to the name of storage modulus. The loss modulus describes the loss of energy within viscous liquids. The ratio between loss modulus and storage modulus is named the loss factor ( $\tan \delta$ ). Assuming an elastic solid,  $\tan \delta$  is zero, whereas it would be infinite for a viscous liquid. Determination of yield strength is performed by an evaluation of the intersection between  $G'$  and  $G''$ , which is a characteristic material property.

#### 1.6.6 Life cycle analysis

LCA is a very useful tool for the evaluation and comparison between different technologies and in most of the cases, it is based on multiple parameters, making it both a powerful but very complex tool. Material flow analysis, carbon footprint and ecological assessment are the most common tools to evaluate its ecological impact. A product life cycle consists of different phases, starting from raw material mining, processing, transport and use phase up to its end of life.

The sole consideration of natural polymers or materials with no or low toxicity is of course not sufficient to completely evaluate its sustainability. Therefore, there is the need to complete every evaluation by an in-depth performed LCA, thus numerically stating its eco-friendliness. A successfully performed LCA is aiming to produce operational conclusions, for example how high are emissions of the product (compared to others) or what are the biggest contributions to lower its impact?

## 2 Materials and methods

### 2.1 Chemicals

To evaluate graphite anode swelling properties, as discussed in 3.1.1 *Swelling and capacitance measurement*, commercially available battery grade anode material graphite (MAGD, Hitachi Chemical, Japan) and cathode material  $\text{LiNi}_{1/3}\text{Mn}_{1/3}\text{Co}_{1/3}\text{O}_2$  (NMC-3102, BASF, Germany) were used as active materials. Conductive carbon (Super C65, Timcal, Belgium), also generally indicated as CB and conductive graphite (KS6L, Timcal, Belgium) were used as conductive additives. For associated cathode preparation, PVDF (Solef 5130, Solvay Specialty Polymers, Italy) was used as binder. For anode preparation, a mixture of CMC (Sunrose MAC 200 HC, NPI, Japan) and styrene butadiene rubber (SBR) binder (ZEON BM451, ZEON, Japan) or PVDF binder (different degrees of crystallinity, Solvay Specialty Polymers, Italy) were used. The used emulsions are stored at room temperature and homogenized before usage. The binder crystallinity was determined by differential scanning calorimetry (DSC) and found out to be 12 % (low crystallinity PVDF), 30 % (medium crystallinity PVDF) and 40 % (high crystallinity PVDF).

For the evaluation of modified copper current collector, graphite anodes were prepared with commercially available battery grade graphite (MAGE, D50 22.8 mm, Hitachi Chemical), CMC (Sunrose MAC200 HC, NPI, Japan), SBR (SBR BM 451B, ZEON, Japan) and CB (Super C65, Imerys, Switzerland). LTO electrodes were prepared with LTO (GN-LTO1, GelonLIB, particle size  $D_{10}$  0.1-0.5  $\mu\text{m}$ ,  $D_{50}$  0.7-1.6  $\mu\text{m}$ , tap density  $\geq 0.65 \text{ g cm}^{-3}$ , specific surface area  $\leq 16.0 \text{ m}^2 \text{ g}^{-1}$ ), PVDF binder (Solef 5130, Solvay, Italy), conductive carbon (Super C65, Imerys, Switzerland) and conductive additive graphite (SFG6L, Imerys, Switzerland).

N-methyl-pyrrolidone (Overlack, 99.8 %, Sigma-Aldrich, Germany) was used as a solvent for the cathode, whereas deionized water was used as a solvent for the anode. 1M  $\text{LiPF}_6$  in EC and vinylene carbonate (Selectilyte RD1001, BASF, Germany) was used as electrolyte for both graphite and LTO cells. For half cells, a glass-fiber Separator (Sartorius, Germany) was used, whereas for preparation of full cells, an inorganic-filled PVDF-separator was used.

Besides evaluation of modified current collector, all of the other LTO-based electrodes were prepared with commercial LTO (90 wt. %, LTO Toda Kogyo, Hiroshima, Japan) and conductive

carbon (6 wt. %, Super C65, Timcal, Switzerland). Sodium alginate (SA, Sigma-Aldrich, Germany) was either used as sole binder (see chapter LTO-SA) or combined with CMC (Sunrose MAC 200 HC, NPI, Japan) and a water-based PVDF binder (Solvay, Italy) - used in different weight ratios to obtain a total binder amount of 4%. Binder evaluation from chapter 3.1 *Graphite with PVDF binder* resulted in best electrochemical and mechanical properties for the medium-crystallinity PVDF binder, which was then used for further tests. The used emulsion of water-based PVDF binder was stored at room temperature and homogenized before usage. Deionized water was used as a solvent for anode preparation.

For the evaluation of rheological properties, LTO-slurries were prepared without and with detergent. The following commercial available detergents were used:

FC4430 (3M, Burgkirchen, Germany) – non-ionic, CO<sub>2</sub>-philic dispersant, a combination of 90% polymeric fluorochemical and 8% non-fluorochemical actives in 2% co-solvent (DPM, toluene) and AA4040 (BASF, Ludwigshafen, Germany) – anionic dispersant, with PAA and ammonium salt as active ingredient in water.

For the preparation of SIBs at different routes, commercially available educts NaH<sub>2</sub>PO<sub>4</sub> · 2 H<sub>2</sub>O (Caesar & Loretz GmbH), TiO<sub>2</sub> (Sigma-Aldrich, ≥ 99.5 %), (NH<sub>4</sub>)<sub>2</sub>HPO<sub>4</sub> (Sigma-Aldrich, ≥ 99.0 %) and Super P (Erachem Comilog N.V.) were used. In the first synthesis route, the NaTi<sub>2</sub>(PO<sub>4</sub>)<sub>3</sub> (NTP) was prepared by a solid state method comprised on the synthesis route given by Zhang et al. [211]. Stoichiometric amounts of the educts were mixed in a planetary mill (Pulverisette 6, Fritsch) using tungsten carbide balls in acetone for 2 h, followed by a drying and sintering step at 500 °C for 5 h in air. One further sintering step was performed at 900 °C for 24 h under ambient conditions. The synthesized NTP was blended with glucose in a mass ratio of 9:1 in deionized water to perform a carbon-coating. The final product was then sintered at 800 °C for 3 h under Argon atmosphere in a tubular oven (Carbolite, MTF 12/25/250).

The second synthesis was performed following the route proposed by Delmas et al. [208] and Cao et al. [213]. The educts NaH<sub>2</sub>PO<sub>4</sub>, TiO<sub>2</sub> and (NH<sub>4</sub>)<sub>2</sub>HPO<sub>4</sub> were ball-milled in a planetary mill in the molar ratio 1:2:2. After 10 minutes of mixing, 1.5 % of CB and 2.5 % of expanded graphite were added and further mixed for 60 minutes at 350 rpm. A final sintering step at 700 °C for 2 h under Argon atmosphere is conducted.

The synthesis of  $\lambda$ -MnO<sub>2</sub> was performed based on the route described by Hunter et al. [68]. A sample of LiMn<sub>2</sub>O<sub>4</sub> was placed in a beaker with water and a solution of dilute acid was added under stirring and pH monitoring. After pH stabilization the solution was stirred for 45 minutes, it was decanted, filtered in a sintered glass and dried at 80 °C in air.

The second  $\lambda$ -MnO<sub>2</sub> synthesis was based on the simple leaching technique route proposed by Yuan et al. [214]. 5 mg of LiMn<sub>2</sub>O<sub>4</sub> was added in 100 cm<sup>3</sup> 0.56 mol dm<sup>-3</sup> H<sub>2</sub>SO<sub>4</sub> at 50 °C for 12 h to get an amaranthine suspension liquid which was ultrasound cleaned for 4 h, then separated, washed and dried at 100 °C in the vacuum oven for 12 h [214].

The NTP anodes were prepared by mixing NTP (70%), CB (20 %) and PVDF (10 %), with NMP solvent to have a solid content of 40 % in a mortar. The anode slurries were casted by a Mini Coater (H-20, Hohsen Corp., Japan) upon a Cu-foil current collector and dried in-line in an oven (Büchi B-585, Büchi GmbH, Germany) at 80 °C for two hours. The average dry electrode thickness was 140  $\mu$ m. As electrolyte, between 400 and 600  $\mu$ L of 1M NaPF<sub>6</sub> in PC:FEC (95:5) was used. Additionally, a volume between 100 and 200  $\mu$ L of LP30 (1M LiPF<sub>6</sub> in EC:DMC) was joined in the part where the metallic lithium RE was placed.

## 2.2 Characterization techniques and equipment

### Formulations and mixing

For the evaluation of swelling properties of graphite anodes (as described in chapter 3.1 *Graphite with PVDF binder*), the following formulations were tested as a referee electrode according to Table 6, starting with a standard formulation.

Table 6: Formulations for reference graphite electrode.

Formulation	Solids [%]	content within solids [%]							comment
		Graphite	CMC	SBR	High cryst. binder	Medium cryst. binder	Low cryst. binder	CB	
002_02	40	95	1.33	2.67	-	-	-	1	No CB predispersion
002_03	40	95	1.33	2.67	-	-	-	1	CB predispersion
003_01	40	95	2	2	-	-	-	1	CMC:SBR = 1:1
004_01	45	95	1.33	2.67	-	-	-	1	CMC:SBR = 1:2
005_01	45	95	2.67	1.33	-	-	-	1	CMC:SBR = 2:1

Formulation 004\_01 resulted in best slurry stability and mechanical properties and was therefore chosen as referee electrode.

Three more different electrode formulations were prepared with the three different water-based PVDF binders, namely those with low, medium and high crystallinity, according to Table 7.

Table 7: Formulation for graphite electrodes containing water-based PVDF binder.

Formulation	Solids content [%]	content within solids [%]									
		Graphite	CMC	SBR	High cryst. binder	Medium cryst. binder	Low cryst. binder	CB			
006_01	45	95	1.33	-	2.67	-	-	-	1		
007_01	45	95	1.33	-	-	2.67	-	-	1		
008_01	45	95	1.33	-	-	-	-2.67	-	1		

The anodes were prepared by mixing graphite (95 %), CB (1%), CMC binder (1.33 %), SBR binder (2.67 %) or respectively an amount of 2.67 % of PVDF binder with different crystallinity and SuperC65 CB with deionised water to have a solid content of 45 %. The anodes were prepared in a high-speed dissolver (Dispermat CV3-plus, VMA-Getzmann GmbH). Viscosity of graphite anode slurries was measured with a Brookfield DV3T viscosimeter and resulted in values between 7675 and 8038 mPa s. The graphite anode slurries were casted by a doctor-blade coater in a roll-to-roll process coating machine on a Cu-foil current collector and dried in-line in a two-step drying tunnel at a temperature range of 95 – 115 °C. The average mass loading was 1.35 – 1.50 mAh cm<sup>-2</sup>. The corresponding cathodes were prepared by mixing NMC (93%), PVDF (3%), Super C65 (3%) and KS6L graphite (1%) with NMP solvent to have a solid content of 60%. The cathode was prepared in a planetary mixer (Thinky Mixer AR-250-C3). Cathode slurries were casted single-sided in a doctor-blade coating process on an aluminium current collector foil and dried in-line in a two-step drying tunnel at a temperature range of 135 – 150 °C.

LTO electrode formulation for the evaluation of current collector modification was prepared by mixing 83 wt-% spherical LTO, 10 wt-% CB and 7 wt-% PVDF in a high-speed dissolver. Graphite electrodes were prepared by mixing 93 wt-% of graphite, 1.33 wt-% CMC, 2.67 wt-% SBR, 2 wt-% CB and 1 wt-% KS6L (graphite) in a planetary mixer. Both graphite and LTO electrodes were casted in a roll-to-roll process coating machine on a standard Cu foil as well as on a galvanically structured Cu foil. The slurry was dried in-line in a four-step drying tunnel at a temperature range of 90 °C – 110 °C – 130 °C – 150 °C. The average loading of the as-prepared LTO anodes was 0.35 mAh cm<sup>-2</sup>, compared to 2.1 mAh cm<sup>-2</sup> for the graphite anodes, which is close to the standard capacity of 2.4 to 2.5 mAh cm<sup>-2</sup> [147,148] used to evaluate mass transport phenomena. Electrochemical measurements were conducted in three-electrode mode using LP 572 (1M LiPF<sub>6</sub> in EC/EMC 3/7 plus 2 % VC) as electrolyte.

The mass loading of LTO anodes was based on a scientific approach to eliminate limitations of mass transport which is known to affect C-rate capability. Least possible limitation of mass transport requires a low coating thickness, whereas least possible electronic limitation needs a high amount of Super C as conducting agent. Both of these steps are not standardly integrated in slurry and electrode preparation.

The LTO electrode formulations for further tests are reported in Table 8.

The processing was carried out by mixing LTO active material (90%), conductive carbon (6%) and the different amounts of binder with deionized water to produce a solids content of 40% in a high-speed dissolver (Dispermat CV3-plus, VMA-Getzmann GmbH). The mixing was performed at 2000 rpm for 120 minutes.

Viscosity of LTO anode slurries was measured with a Brookfield DV3T viscometer and resulted in values between 3917 and 7873 mPa·s. Another viscosity test was performed 1 and 7 days after mixing. The LTO slurries were manually casted on a carbon-coated Al-foil current collector and dried in a two-step drying tunnel at a temperature range of 90 – 100 °C. The average areal capacity of the electrodes was 0.35 – 0.50 mAh cm<sup>-2</sup>. The water-processed electrodes were cut into round pieces with a diameter of 12 mm and dried at 110°C for 24 h under vacuum.

Table 8: Formulation of LTO electrodes

Composition	LTO-SA	LTO-PVDF/CMC	LTO-PVDF/SA
LTO active material	90	90	90
Super C	6	6	6
Sodium alginate	4	-	2.67
CMC	-	2.67	-
PVDF	-	1.33	1.33

Both detergents for the evaluation of slurry rheology were taken from a pre-prepared solution of 10% dissolved in deionized water and diluted further in deionized water to reach a total concentration of 0.5%. The slurries were prepared in the following order:

Table 9: Slurry characteristics and composition for rheological experiments.

Description	Code	Composition [%SA/LTO/CB/Detergent]
SA-H <sub>2</sub> O	SA1	4/0/0/0
SA-H <sub>2</sub> O-CB	SA2	4/0/6/0
SA-H <sub>2</sub> O-CB-LTO	SA3	4/90/6/0
SA-H <sub>2</sub> O-CB-LTO-Dispex	SAD1	4/90/6/+0.5 Dispex
SA-H <sub>2</sub> O-CB-LTO-FC4430	SAD2	4/90/6/+0.5 FC4430

The rheological measurements have been performed in forms of a viscosity test, amplitude sweep and frequency sweep with a MCR 502 Rheometer (Anton Paar, Graz, Austria) using double gap geometry (DG26.7). Rheological measurements were taken from slurries 24 hours after preparation, but with a homogenizing step before measurements. Amplitude sweep tests in a range of amplitude  $\gamma = 0.001 - 1\%$  and an angular frequency of  $10 \text{ rad s}^{-1}$ . Frequency sweep tests have been conducted using an amplitude  $\gamma = 0.01 \%$  and an angular frequency  $\Omega = 0.1 - 628 \text{ rad s}^{-1}$ . Temperature was varied from 20 to 50 °C with an increment of 10 °C each.

Contact angle (CA) measurements were performed with a CA System OCA from Data Physics Instruments (Filderstadt, Germany). A sample drop of 1  $\mu\text{L}$  was placed on a piece of aluminium foil (sessile drop method) at room temperature and ambient conditions. It was immediately measured and a photograph was taken by a camera. The optical measurement was evaluated by the Laplace-Young method. Each slurry was measured three times and the average was used as overall resulting CA.

### **SEM/EDX measurements**

A field emission scanning electron microscope (FE-SEM) (Merlin Compact, Zeiss, Germany) with energy dispersive X-ray spectroscopy (EDX) was used to take EDX element mapping images to check binder distribution of graphite anodes. With this device, also micrographs of the fresh and cycled LTO-electrodes were taken. In order to remove electrolyte residues, the cycled LTO-electrodes were rinsed before analysis.

A Zeiss Auriga 40 focus ion beam (FIB)/SEM electron microscope was used to take micrographs of modified current collector and the color figures were prepared from a FIB/SEM tomography using an energy selective backscatter detector (EsB). The stack of EsB images was then segmented and processed with the image processing software Dragonfly 4.1 to create the colored images and also a 3D tomography.

Brunauer-Emmett-Teller (BET) surface area measurements were taken with a Quantachrome Monosorb rapid surface area analyser.

Calculation of the roughness factor (RF) of the untreated and dendritic copper current collector in order to estimate the degree of physical surface enlargement was performed by the following equations:

$$m_{\text{Cu-sample}} = \frac{\rho_{\text{Cu}}}{A_{\text{geometric}} \cdot d_{\text{Cu-foil}}} \quad \text{Equation 2-1}$$

$$A_{\text{true}} = BET_{\text{Cu-fo}} \cdot m_{\text{Cu-sample}} = BET_{\text{Cu-foil}} \cdot \frac{\rho_{\text{Cu}}}{A_{\text{geometric}} \cdot d_{\text{Cu-sample}}} \quad \text{Equation 2-2}$$

$$RF = \frac{A_{\text{true}}}{A_{\text{geometric}}} = \frac{BET_{\text{Cu-fo}} \cdot \rho_{\text{Cu}}}{d_{\text{Cu-sample}}} \quad \text{Equation 2-3}$$

## Electrochemical characterization

Sodium ion cells were assembled to T-cells in three-electrode mode and subjected to electrochemical tests in forms of cyclic voltammetry (CyV) and cycling tests with a multichannel potentiostat (VMP, Perkin Elmer).

The electrochemical characterization was performed with a battery tester (CTS-lab, BaSyTec), using galvanostatic (CC) and potentiostatic (CV) modes for charging and CC mode for discharging step. Potential setting and monitoring is done by a pseudo-reference electrode consisting of elementary Lithium. The CE also consists of elementary lithium, whereas as WE the anodes to be investigated are used.

Half-cell measurements were performed by combining the different anodes with elementary Lithium. For evaluation in Swagelok® three-electrode-cells - as schematically depicted in Figure 11 and graphically in Figure 12 - the anodes were cut in into round pieces and dried at 110 °C for 24 h under vacuum. The Swagelok setup was assembled in an argon filled glove box (MB20, H<sub>2</sub>O and O<sub>2</sub> < 1 ppm).

Lithium CE disks were cut from elemental lithium. A lithium disk was placed on the stamp located in the cell. Two separator disks were placed on the lithium electrode. Additionally,

lithium was punched with the smallest stamp of the half-cell components, which was used as RE. The separators were filled with 100  $\mu\text{L}$  of the electrolyte. The LTO electrode was placed on the separator. At the upper opening, a separator was placed and wetted with the corresponding electrolyte. The lithium reference was placed on the separator and fixed with a sealed stamp and a screw cap. For all measurements, three cells were assembled with a similar weight loading of the LTO working electrodes.

For half-cell measurements of the graphite anode, the voltage range was adjusted to 0.02 – 1.5 V and for full cell measurements, the voltage range was adjusted to 3.0 – 4.2 V. Formation was done for both graphite half and full cells by two cycles of C/10, which was calculated by the active material weight and theoretical capacities of NMC of  $168 \text{ mAh}\cdot\text{g}^{-1}$  and graphite of  $372 \text{ mAh}\cdot\text{g}^{-1}$ . For half-cell measurements of LTO anode, the voltage was ranging from 1.0 – 2.2 V. Formation of LTO cells was performed by three cycles of C/3, calculated by active material weight and theoretical capacity of  $175 \text{ mAh}\cdot\text{g}^{-1}$ .

The LTO electrodes described in chapter 4 *Improved current collector surfaces for LTO electrodes* were punched into circular samples with a handheld punch (Nogamigiken Co., Ltd., Tokyo, Japan) with a size of 10 mm in diameter and dried in a drying chamber at  $110^\circ\text{C}$  for 12 h under vacuum (Binder, APT.line™ VDL 115 vacuum drying chamber with microprocessor-programme controller).

A battery tester (CTS-LAB, BasyTec, Asselfingen, Germany) and a potentiostat (PGSTAT204, Metrohm, Filderstadt, Germany) were used to evaluate electrochemical properties of electrodes on modified current collector. Formation was performed by applying two cycles at C/3. For subsequent EIS analysis along state of charge (SOC), cells were first delithiated to 2.2 V at C/3 rate after formation. Hence, the cells were lithiated up to each point of investigation by applying C/3 rate for 30 min. Final EIS analysis was performed after reaching the lower voltage limit of 1.0 V. EIS measurements were carried out at  $25^\circ\text{C}$  (INCU-Line IL 68 R, VWR, Ismanning, Germany) after 2h rest at OCV, in the frequency range of 100 kHz – 10 mHz (potentiostatic mode) using  $5 \text{ mV}_{\text{rms}}$ . Equivalent circuit fit analysis of EIS data was performed using the Z-fit protocol within a MatLAB environment. EIS measurements were performed in three-electrode mode, where voltage was measured at the RE and current at the CE.

Measurement of internal resistance  $R_{AC}$  was performed as a measurement of IR-drop in a ten minute relaxation period between each charging and discharging step.  $R_{ac}$  describes the ohm part of the internal resistance and is calculated by the first measurement of the actual program step and the last measurement of the previous program step according to the following formula:

$$R_{ac} = \frac{\Delta U}{\Delta I} = \frac{U_2 - U_1}{I_2 - I_1} \quad \text{Equation 2-4}$$

To ensure reproducibility of the study, each test has been carried out in triplicate.

Full cell tests were performed by combining the prepared graphite anodes with NCM cathodes. Full cell measurements were performed in pouch foil with active areas of anode and cathode of  $5.4 \times 8.4 \text{ cm}^2$  and  $5.0 \times 8.0 \text{ cm}^2$  respectively. All parts were laminated with the help of a laminator at a line force of  $157 \text{ N cm}^{-1}$  in a temperature range of  $110 - 120 \text{ }^\circ\text{C}$ . The stacks were then dried at  $110 \text{ }^\circ\text{C}$  for 24 h under vacuum and then placed in an argon filled glovebox (MB20,  $\text{H}_2\text{O}$  and  $\text{O}_2 < 1 \text{ ppm}$ ), where the electrolyte was filled in and the cell was sealed. The cell was tempered at  $60 \text{ }^\circ\text{C}$  for 4 h before starting of the electrochemical characterization.

To study the electrochemical performance of the anode without having any influence from cathode, the oversized cathode  $\sim 30\%$  is used in pouch cell format.

### **Peeling/adhesion/bending/swelling tests**

Peeling tests of graphite and LTO electrodes were performed by cutting specimens from each coating thickness with a size of  $50 \times 80 \text{ mm}$  and stuck with a double-sided adhesive tape upon the supporting surface. A  $19 \text{ mm}$  adhesive tape was pressed upon the coating and then tried to peel it off with a Peel-off Force Special Test Stand (TPE 50, Sauter GmbH) orthogonal to the supporting surface. The maximum resulting force was recorded as peel-off force and the optical result described.

A self-constructed pull-off test bench was selected in order to measure the adhesion and cohesion of the anodes. The vertical movement to approach the sample to be investigated was carried out by a linear axis (CKK-145-NN-1) manufactured by Bosch Rexroth AG (Lohr am Main, Germany) and the force measurement was performed by  $2.0 \text{ kN}$  load cell (F2210) with

a sampling rate of 5000 Hz from Tecsis GmbH (Offenbach, Germany). For the adhesion measurements, round samples were punched out with a handheld punch ( $\varnothing$  15 mm), placed between two sample holders and fixed with a polyacrylate double-sided adhesive tape (tesafix 5696, extra strong from Tesa SE). At the end of the test procedure, an analysis of the failure mode was performed. The failure mode (either adhesive or cohesive) was determined using the definition proposed by DIN EN ISO 4624 and DIN EN ISO 10365. More details regarding the measurement method used can be found in [149] The fractions of cohesive and adhesive breaking were calculated using an image-based MatLAB script.

Bending tests for graphite and LTO electrodes were performed by bending the coated foil around a roll with a diameter of 1 cm. Adhesive or cohesive breaking is evaluator assessed.

To perform swelling tests, graphite anodes were cut into pieces of 10 cm x 16 cm and placed on the measurement table. In order to prevent from solvent evaporation, the set-up was covered by PE foil and a syringe was placed through a small hole in the PE foil, so that solvent can directly drop on the coated electrode. The defined amount of solvent in a certain time span was controlled by a syringe pump. The capacitance sensor (capaNC DT SERIE 6100, Micro-Epsilon) was placed 1 cm next to the syringe to measure the change in coated thickness with time. For swelling test, electrolyte containing a mixture of EC and DMC in a weight ratio of 5:1 but without  $\text{LiPF}_6$  conducting salt is used. These tests have been performed under normal atmosphere, so due to the danger of a decomposition of the conducting salt only a mixture of EC:DMC was used. The amount of electrolyte, 250  $\mu\text{L}$ , was applied at a rate of 100  $\mu\text{L min}^{-1}$ . Due to the set-up, I was only concentrating on the time shortly after solvent addition, as the set-up allows a redistribution as well as evaporation of the electrolyte. Here only the sudden soaking of electrolyte into the electrode framework is studied.

### **Galvanical structuring**

The galvanic structuring of the current collector Cu foil discussed in chapter 4 *Improved current collector surfaces for LTO electrodes* was achieved by a reel-to-reel plating line consisting of an electrolytic degreasing bath, an acidic activation bath containing diluted sulphuric acid (5 wt-%), a deposition tank and a chromate passivation with intermediate rinsing steps. The copper deposition was done using an acidic copper-sulphate based

electrolyte and applying pulsed current at an average of  $0.06 \text{ A cm}^{-2}$  for 29 seconds. After wet processing the substrate was dried in-line in a hot air oven.

## 3 Anode formulations with water-based binders

### 3.1 Graphite with PVDF binder

Commercial LIBs are mostly using PVDF binder to fabricate the electrodes. The use of harmful and expensive organic solvents such as NMP is required to dissolve the PVDF binder for preparation of the slurry [150]. To overcome these drawbacks especially concerning safety and because of ecological reasons, a novel fluorinated binder in aqueous dispersion has been introduced by Solvay Specialty Polymers, Italy, consisting of nano-sized (~250 nm) primary particles of PVDF in the shape of spheres [151]. Mostly, PVDF aqueous dispersions are produced by a heterogeneous emulsion polymerization [152]. In addition, the particles are modified with polar monomers to promote adhesion. Advantageously, no organic solvent is required to dissolve this PVDF dispersion. Lithium Cobalt Oxide electrodes have already been prepared in this kind of aqueous PVDF binder [153].

Here, a PVDF binder based aqueous electrode fabrication process for the preparation of graphite electrodes is introduced. The study includes a peeling test, swelling test and electrochemical tests in half-cell and full-cell configuration.

Some research groups have reported the swelling behavior of polymeric binders or swelling within the composite electrode, as physical swelling needs to be investigated in a qualitative and quantitative way [154,155]. The swelling of PVDF polymers in a carbonate electrolyte has been measured by using quartz crystal microbalance [154]. Scanning electron microscopy was also used to measure the swelling of a PVDF polymer in an EC:DC electrolyte with 1 M LiPF<sub>6</sub> quantitatively but after applying the electrolyte, the system needs 30 minutes to measure the thickness of polymer [155].

*The Electrochemical Society is acknowledged for the permission to reprint parts of the following publication: C.Toigo, M. Singh, B. Gmeiner, M. Biso, K.-H. Pettinger, "A Method to Measure the Swelling of Water-Soluble PVDF Binder System and Its Electrochemical Performance for Lithium Ion Batteries", J. Electrochem. Soc. 167 020514 (2020)*

Anode swelling has also been investigated by using a selective shielding cathode, where electrodes with high mechanical strength are required in order to stand against the stress during process [156]. This part will concentrate on the physical swelling and implement a measurement technology that can be used rapidly as well as during processing. It is also shown that the swelling measurements on the anode electrodes can be performed with low efforts, on-line and without the necessity of a controlled atmosphere at very high accuracy starting at that time when the first drop of solvent is placed upon the anode surface. This is based on the fact that only the solvent without  $\text{LiPF}_6$  is applied upon the coating. Therefore, no dangerous products from its reaction with air are formed. Furthermore, this method can also be used to receive more detailed information about binder crystallinity.

### 3.1.1 Swelling and capacitance measurement

It is known that the crystallinity of the binder influences the performance of a cell due to swelling occurring by the carbonate based electrolytes [154]. Therefore, the effect of crystallinity on the physical swelling of anode electrodes is investigated. A volumetric expansion of polymers (binders, dispersive agents) after soaking in the electrolyte or the uptake of organic electrolyte due to electrolyte-binder interaction is named physical swelling [156]. The electrode swelling due to lattice expansion during cycling is called electrochemical swelling and is a well-known and well-described phenomenon [156]. The swelling behavior of separators as well as of graphite anode in LIBs have already been investigated [102,155,157,158]. Usually, the swelling behavior is tested by measuring thickness and mechanical properties in different solvent environments. [150,159]. It has been reported that a polymer with high crystallinity shows high solvent resistance, as the crystalline domains are not swollen by a solvent (see Figure 8). For the characterization of mechanical properties of separators and polymers, the swelling test sample is immersed in the typical electrolyte to study the change in mechanical properties in comparison to the dry sample. Separators show a volume expansion coming along with a reduction of mechanical properties resulting from solvent penetration within the polymer host. Subsequently, this leads to an increase of the total thickness of electrodes, separators and cells. Scratch test showed that a higher crystallinity also leads to better adhesion strength [156]. All the above mentioned properties indicate a higher intrinsic stability of high crystallinity materials in contrast to ones with lower

crystallinity. The swelling test is implemented as a measurement method that can be used to detect physical swelling with the main advantages of being used rapidly and during processing. Furthermore, no controlled atmosphere is necessary, the measurement can be carried out with low efforts, works at high accuracy and is starting at that time when the first drop of electrolyte is placed upon the surface. This method is also capable of retrieving information about crystallinity.

### 3.1.1.1 Swelling pre-tests

First swelling tests have been performed using solely ethanol as swelling agent in order to evaluate the order of magnitude and to get familiar with the handling of the equipment. The results are visible in Figure 16 and show a volume expansion of round about 30 % (31.1 % for 45  $\mu\text{m}$  coating and 27.3 % for 99  $\mu\text{m}$  coating).

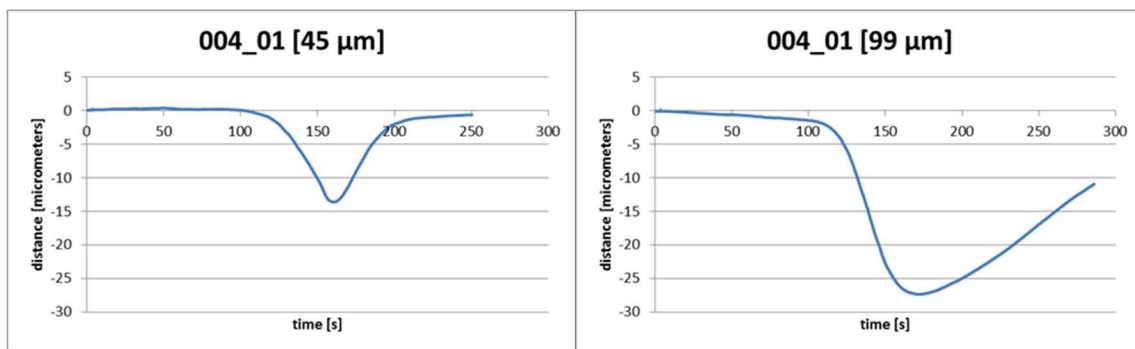


Figure 16: Swelling measurement with ethanol at different dry thicknesses. Reprinted from ref. [49] under the terms of the Creative Commons CC-BY license.

This shows clearly that the distance between the electrode and the sensor decreases after soaking the solvent into the electrode. The expansion caused by swelling can be calculated as follows:

$$expansion (\%) = \frac{max.distance (\mu m)}{coating thickness (\mu m)} \quad \text{Equation 3-1}$$

### 3.1.1.2 Swelling tests with EC/DMC

In a next step, the swelling solvent was changed from ethanol to a mixture of EC and DMC in a weight ratio of 5:1 without the conducting salt  $\text{LiPF}_6$ . As the tests have been performed under ambient atmosphere, the danger of a decomposition of the conducting salt had been avoided.

The results for different binder crystallinity can be seen in Figure 17. The crystalline binder does not show swelling behavior at all. After 220 s, even a non-conductive layer of electrolyte can be found upon the surface which is not soaked up. In contrast to the binder with high crystallinity, the binder with low crystallinity shows an uptake of 17 % compared to its original thickness. The binder with medium crystallinity revealed an expansion of 12 % from its original thickness.

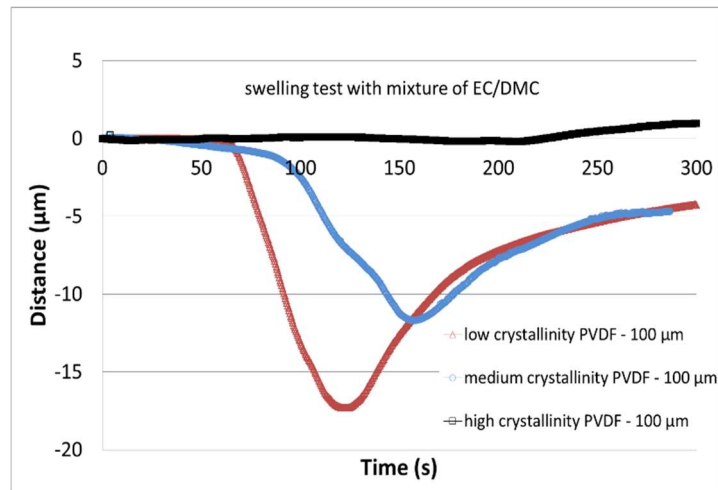


Figure 17: Swelling tests of binders with different crystallinities with mixture of EC/DMC. Reprinted from ref. [49] under the terms of the Creative Commons CC-BY license.

Obviously, soaking of the electrolyte into high- and medium crystallinity binders containing anodes is not as intensive as into low crystallinity binder containing anodes. This can be explained by the polymeric microstructure from Figure 8. Due to the highly ordered structure of a crystalline polymer, solvent molecules cannot penetrate it as easily as into the disordered structure of an amorphous polymer. Polymer microstructure also gives some possible explanations on the causes for different electrochemical performance of system with different crystallinity. On the one hand it means that in a highly crystalline polymer only small amounts of the binder are able to perform swelling, as this only occurs in amorphous regions [92]. Here, the less swollen binder has a good ability to share electrical conductivity with the active material. On the other hand, a binder with low crystallinity has a higher amount of amorphous regions where higher amounts of electrolyte can penetrate into the composite electrode to ensure good ion transport.

Figure 18 demonstrates the swelling test procedure, for visibility reasons without the upper polyethylene foil. The electrolyte is dropping upon the electrode within a defined distance to

the capacitance sensor. Already during application, the electrolyte is soaked up within the electrode material and distributes according to electrode structure. As visible, the soaking is not perfectly uniform as electrode structure is neither. For an ideal electrode and perfectly plane underground, the distribution should take place in a round shape.



Figure 18: Swelling test – practical procedure.

### 3.1.2 Mechanical and physicochemical measurements

Besides the newly developed swelling tests, some standard mechanical and physicochemical tests have been performed to evaluate relevant mechanical properties

#### 3.1.2.1 EDX spectroscopy

As a method to verify binder distribution at the surface of the composite electrode, EDX spectra have been recorded, which can be seen in Figure 19. Fluorine is used as a marker to

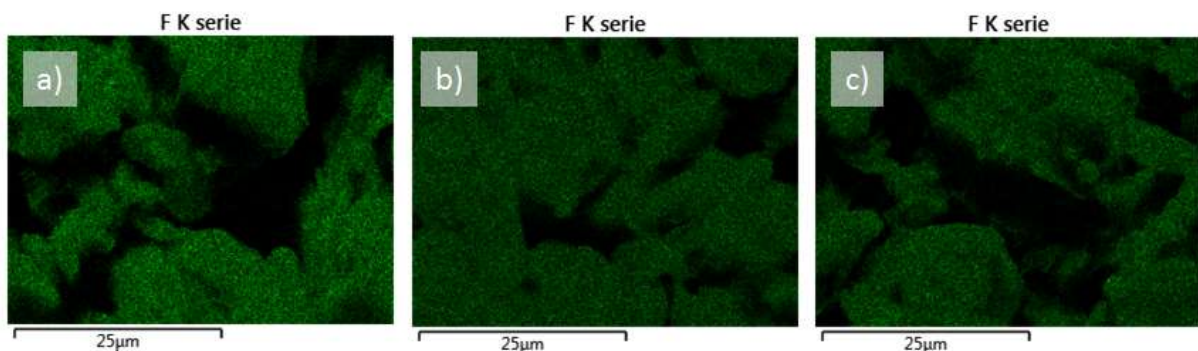


Figure 19: EDX image of a) low, b) medium, c) high crystallinity PVDF. Reprinted from ref. [49] under the terms of the Creative Commons CC-BY license.

indicate the existence of binder PVDF. Binder distribution seems to be very homogeneous for all types of used PVDF. The morphologies like particle size and distribution of the samples are similar leading to the assumption that a comparable electrode preparation was successful.

#### 3.1.2.2 Peeling test

In order to quantitatively measure the adhesion strength of the electrode coating and cohesion of the particles throughout the coating, a peeling test is performed. Figure 20a depicts the schematic set-up of the peeling test stand. The resulting forces are measured and are shown in Figure 21. Adhesive (electrode coating partially delaminated) and/or cohesive (electrode coating damaged) breakings are observed. A reduced peeling force that is required to peel off the adhesive tape is observed upon increasing the electrode thickness. Reference and medium crystallinity PVDF containing anodes required highest peeling force in comparison to the other anodes in a thickness range from 50  $\mu\text{m}$  to 100  $\mu\text{m}$ , whereas all anodes showed similar peeling force at a thickness of 125  $\mu\text{m}$ . Typical results, like a mostly adhesive (between electrode and current collector) and cohesive (within electrode) breaking are exemplary shown in Figure 20b and c.

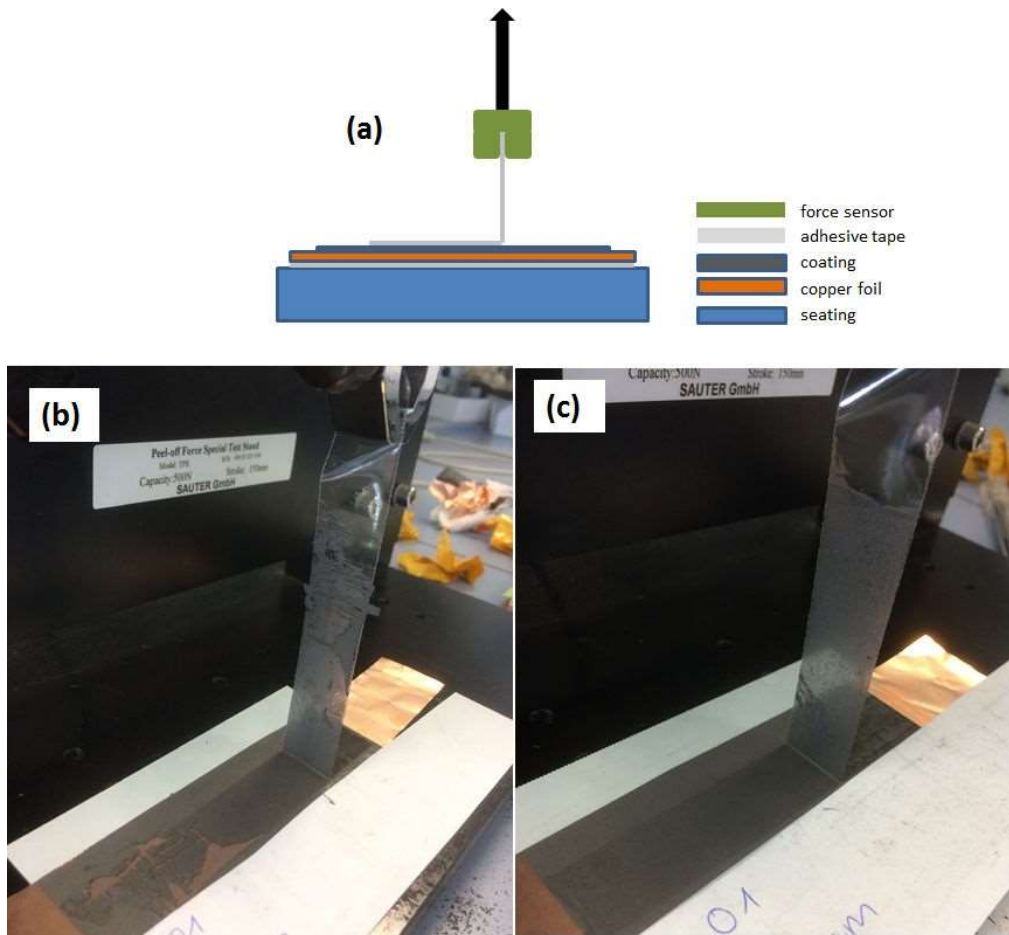


Figure 20: Schematic set-up of peeling test (a), typical results: mostly adhesive (b) and cohesive (c) breaking. Reprinted from ref. [49] under the terms of the Creative Commons CC-BY license.

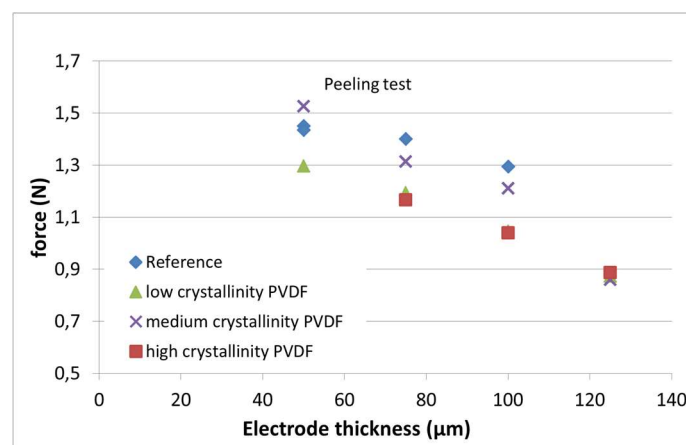


Figure 21: Results of peeling test for different crystallinities and electrode thicknesses. Reprinted from ref. [49] under the terms of the Creative Commons CC-BY license.

Binder crystallinity is known to have an effect on mechanical strength. It is reported that higher crystallinity exhibits higher scratch adhesion strength [157]. In contrast to this statement, the adhesion for medium crystallinity binder is found to be higher than for the one

with high crystallinity. Because of the used latex form it has to be completely melted to reach the best intrinsic adhesion. This is the case for the binder system with medium crystallinity, while the highly crystalline binder system is reasonably not melted due to its higher melting point. Compared to the low crystallinity binder system, the medium crystalline system has higher intrinsic adhesion properties on the basis of its higher crystallinity.

### 3.1.2.3 Bending test

Bending tests are performed by winding the coated electrode around a roll of 1 cm diameter. It was found that the electrodes showed no delamination and cracks up to the thickness of 125  $\mu\text{m}$ . Figure 22 gives an example on delamination failure during bending test and Figure 23 shows how well-formulated electrode coatings are bent around the roll without the appearance of delamination or cracks.

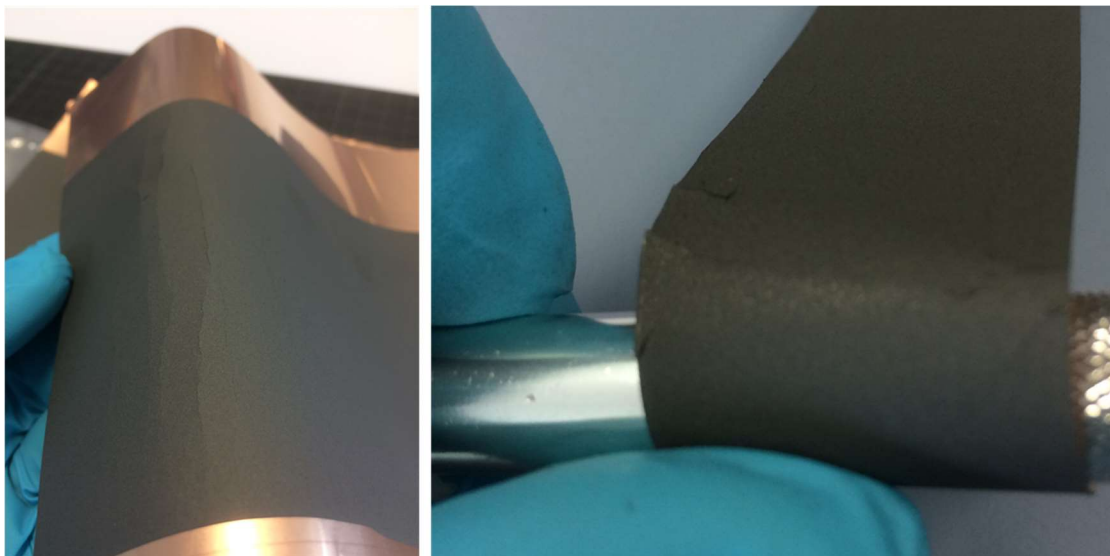


*Figure 22: Result of bending test - example delamination.*



Figure 23: Result of bending test - no delamination. Reprinted from ref. [49] under the terms of the Creative Commons CC-BY license.

Table 10: Result of bending tests for all electrode formulations and thicknesses.

formulation	dry coating thickness [ $\mu\text{m}$ ]							
	38	41	44	48	56	72	102	131
002_02	-	ok	ok	ok	ok	-	-	-
002_03	-	ok	-	ok	ok	adh. break	-	-
003_01	-	-	-	-	ok	ok	ok	adh. break
003_02	-	ok	ok	ok	-	-	-	-
004_01	ok	-	-	ok	-	ok	-	ok
005_01	ok	-	-	ok	-	adh. break	-	adh. break
006_01	-	-	-	-	-	ok	ok	adh. break
007_01	-	-	-	ok	-	ok	ok	adh. break
008_01	-	-	-	ok	-	ok	ok	adh. break

In

Table 10, all bending test results are collected both from formulations used for electrochemical tests and other test formulations with slightly different composition. All of them are showing a good bending stability for nearly all formulations up to an electrode thickness of 131  $\mu\text{m}$ .

### 3.1.3 Electrochemical measurements of graphite anodes

The prepared electrodes have been subjected to half cell and full cell tests. The half cell has been assembled with graphite electrode as WE and Li foil as CE and RE. For the evaluation in full cell in pouch format, the graphite electrodes are combined with NCM cathodes.

### 3.1.3.1 Half cell tests

Figure 24 shows the charge-discharge curves of graphite anodes at different C-rates in the voltage range of 0.02-1.5 V, calculated on base of the nominal capacity given by the supplier. Anode in half cells delivered discharge capacities of 362 mAh/g (100 %), 367 mAh/g (101 %), 357 mAh/g (99 %) and 309 mAh/g (85 %) after second formation cycle at 0.1 C with reference (SBR/CMC), medium, low and high crystallinity PVDF binders, respectively.

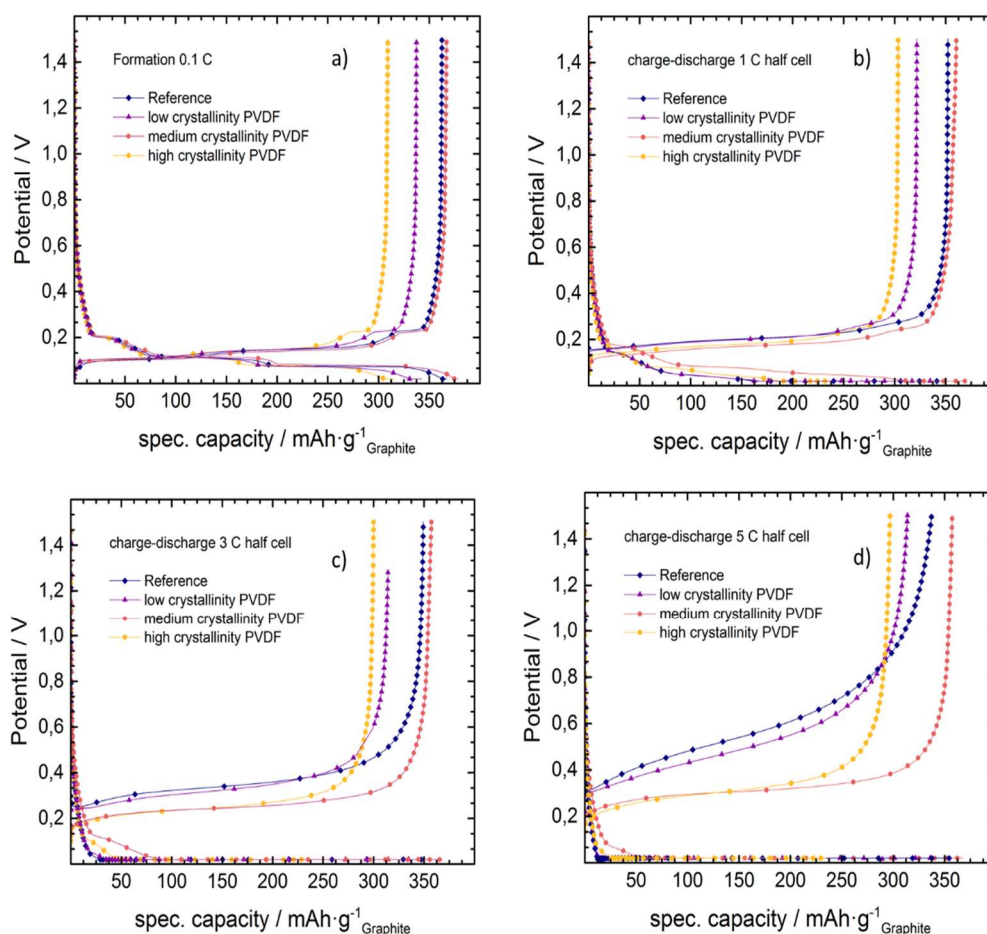


Figure 24: Charge-discharge profiles of graphite anodes containing different types of water-based PVDF binder at different C-rates: a) 0.1 C b) 1 C c) 3C d) 5C rate. Reprinted from ref. [49] under the terms of the Creative Commons CC-BY license.

The values between parentheses indicate the percentage in comparison with the first formation cycle. PVDF binder with medium crystallinity exhibited a slightly higher discharge capacity in comparison to the conventional water-based CMC binder and other PVDF binder systems. Binder crystallinity showed a critical role in the electrochemical performance of LIBs.

The performance of PVDF with that of amorphous poly-N-vinylformamide (PNVF) reported in literature [160] is compared. Amorphous PNVF binder reported a discharge capacity between 130 and 190 mAh g<sup>-1</sup> at 5C and between 80 and 130 mAh g<sup>-1</sup> at 10C rate [160]. These values are quite far away from the measured values of amorphous PVDF/CMC binder system with discharge capacities of 295 mAh g<sup>-1</sup> at 5C and 273 mAh g<sup>-1</sup> at 10C (both medium values), as reported in figure 25. The use of PVDF as binder with NMC and graphite active materials is an established and well-known technology [161].

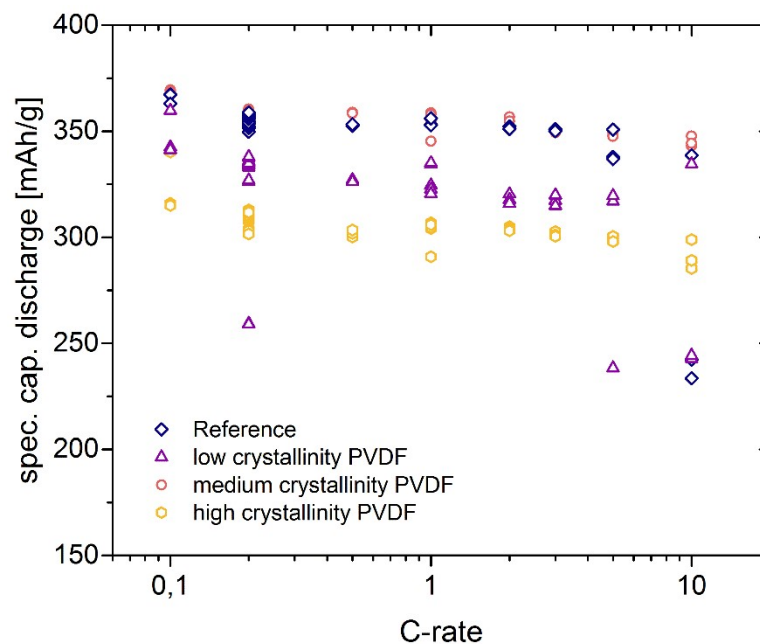


figure 25: Result of half-cell C-rate test. Reprinted from ref. [49] under the terms of the Creative Commons CC-BY license.

A water-soluble binder system is a very promising option regarding capacity retention, mechanical strength and the positive environmental impact. From the results it is clear that dispersed PVDF binder system with medium crystallinity exhibits good adhesion to electrode materials and current collectors as well as a high electrochemical stability during cycling, as can be seen in Figure 25. Looking at the three different types of binder systems, the performance of the medium-crystalline system is boosted by the compromise between adhesion and swelling. Several studies on NMP based PVDF binders can be found, resulting in capacities of 332 mAh g<sup>-1</sup> (0.1C), 324 mAh g<sup>-1</sup>(0.2C) [161] and 350-361 mAh g<sup>-1</sup> (0.2C) [162]. Compared to these results, the medium-crystalline binder delivered the discharge capacity in the same range (see figure 25).

When charged and discharged repeatedly, the water based binders show stable capacities over the course of several cycles at each C-rate from 0.1C to 10C. Half-cell tests of the investigated PVDF binder system showed promising results concerning C-rate stability – especially from the medium-crystallinity binder. Low crystallinity binder resulted in a big variation in the capacity and capacity also decreased with increasing C-rate. The binder with high crystallinity resulted in significant capacity retention at high C-rates, but showed the lowest capacities at different C-rates in comparison to other binder formulations. C-rate test indicates that the reference and medium crystallinity PVDF binder delivered the similar capacity  $>350 \text{ mAh g}^{-1}$ , while high and low crystallinity binders showed slightly lower capacity  $>300 \text{ mAh g}^{-1}$  up to 5C rate.

### 3.1.3.2 Full cell tests

Figure 26a) shows the galvanostatic charge-discharge profiles of full cells containing water-soluble binders at 0.1 C rate. Full cells delivered discharge capacities of  $167 \text{ mAh g}^{-1}$  (100 %),  $142 \text{ mAh g}^{-1}$  (85 %),  $137 \text{ mAh g}^{-1}$  (82 %) and  $129 \text{ mAh g}^{-1}$  (77 %) with reference, medium, low and high crystallinity binder systems respectively. As expected from the half-cell measurements, the full cells also delivered a comparable capacity with respect to reference binder systems.

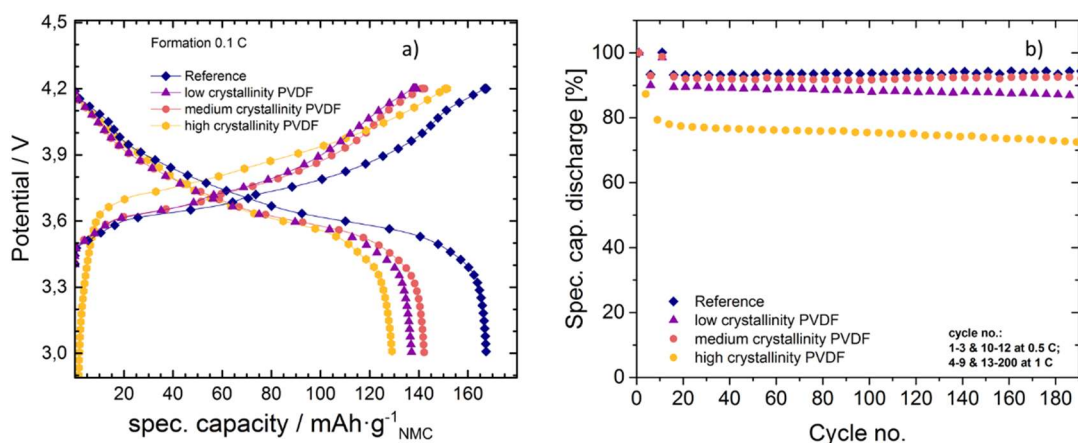


Figure 26: Electrochemical performance of full cells (a) charge-discharge profiles at 0.1 C rate; (b) discharge capacity data at different C-rates. Reprinted from ref. [49] under the terms of the Creative Commons CC-BY license.

Medium crystallinity binder exhibited the highest capacity in comparison to other water-soluble PVDF binders. The cycling data of full cells is compared in Figure 26b. From the relative capacity graphs, it can be seen that the reference and medium crystallinity PVDF binders showed negligible capacity retention over 200 cycles. The low and high crystallinity ones showed 95 % and 80 % lower capacity than the binder with medium crystallinity after 150 cycles. The capacity-fading rate is varying corresponding to the crystallinity of the binder. The binder with high crystallinity showed 72 % capacity fade after 200 cycles. The results are comparable to reported values obtained from a stable electrode-separator interface by lamination techniques [163]. It is worth to mention here that lamination technique applied during the preparation of cells with water-soluble binders delivered similar discharge capacity, as has been reported [92,163,164], by using NMP soluble PVDF binder.

Comparing the values of remaining capacity after the second formation cycle showed least formation losses for the formulation using medium crystallinity binder followed by reference formulation (see Figure 27). The values have been calculated as the difference between initial capacity and remaining capacity after the second formation cycle. The cells prepared with high and low crystallinity PVDF binder resulted in high formation losses.

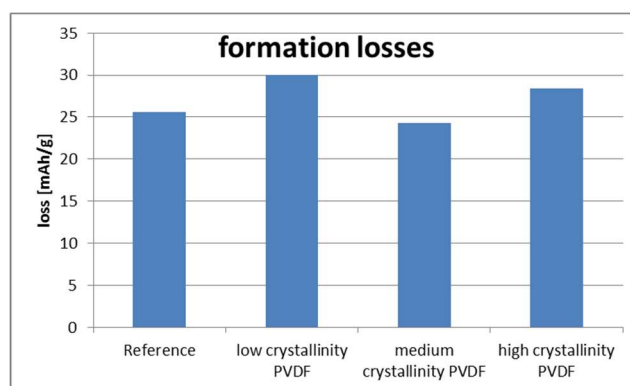


Figure 27: Irreversible capacity losses during formation of full cells. Reprinted from ref. [49] under the terms of the Creative Commons CC-BY license.

Due to the results of electrochemical measurements, it was suggested that the influence of good electrical conductivity (highly crystalline material) is little less important than a good ion transport due to good electrolyte penetration. The semicrystalline material benefits from both influence factors and therefore shows best results for electrochemical tests.

### 3.1.4 Conclusion

Graphite anodes with water-soluble CMC/SBR and CMC/PVDF binder systems are successfully coated on a copper foil using conventional slurry and electrode roll to roll coating techniques. PVDF binders with three different crystallinity were evaluated. The prepared electrodes were tested mechanically by peeling test and scratch test and electrochemically in half-cell and full cell configuration. Anode with medium crystallinity binder system showed an overall highly mechanical stable coating comparable to RE. Neither cycling stability nor power capability resulted in significant disadvantages compared to reference formulation.

The CMC/PVDF binder system is an environmental friendly method with all the advantages of PVDF binder, but no explosion-proof requirements during dispersion or mixing. Further advantages covering the whole production and recycling processes as well as safety issues during operation are encouraging to do deeper research in this area.

A novel and unique capacitance measurement method was introduced for quantification of electrode swelling which is combining several advantages like on-line measurement with direct response, easy handling and accuracy in micrometer-range. The percentage change of dry thickness in relation to the swollen thickness could be verified and showed a direct relationship between chemical structure and functionality – different crystallinity are depicted by showing a varying degree of physical swelling. This method can also be used for characterization during the processing of anodes and cathodes as well as for swelling experiments of separators, for example.

## 3.2 LTO with sodium alginate binder

*MDPI is acknowledged for the permission to reprint parts of the following publications:*

C. Toigo, M. Biso, K.-H. Pettinger, C. Arbizzani, "Study on Different Water-Based Binders for  $\text{Li}_4\text{Ti}_5\text{O}_{12}$  Electrodes" *Molecules*, 25, 2443 (2020)

C.Toigo, M.Krakalik, E.Bradt, K.-H.Pettinger, C.Arbizzani, "Rheological properties of aqueous sodium alginate slurries for LTO battery electrodes" *Polymers*, 13, 3582 (2021)

### 3.2.1 Bio-based polymers for battery applications

A huge variety of different binder (systems) is available for LIBs and SIBs. Ranging from well-established and standardly used ones like PVDF, PTFE, the combination of CMC/SBR to PAA, PVA and PEG, there is also the trend to utilize bio-based polymers as binders for battery applications. For example, guar gum, chitosan and SA are currently under research, offering good binding abilities at high availability, low prices and non-toxicity.

This intensive research is mainly induced by an increased awareness on ecological and economical aspects, like material sustainability, ethical mining or a good relation of cost and benefit. Furthermore, safety aspects are more and more of a concern for both people and companies, thus moving from small- or middle-scale applications like mobile phones or laptops towards large-scale applications in EVs and home or industry storage systems. So a significant higher amount of energy is stored, thus encouraging to go deeper into the topic of battery safety, which can be further enabled by bio-based polymers. Therefore, a trend towards further intensive research on the functionalization, modification and development of suitable bio-based polymers is clearly visible.

### 3.2.2 Chemical properties and application fields of sodium alginate

SA, depicted in Figure 28, is a linear copolymer composed of  $\beta$ -D-mannuronic acid and  $\alpha$ -L-guluronic acid monomers linked by a  $\beta$ -(1-4) glycosidic bond and are therefore classified as polysaccharide [165].

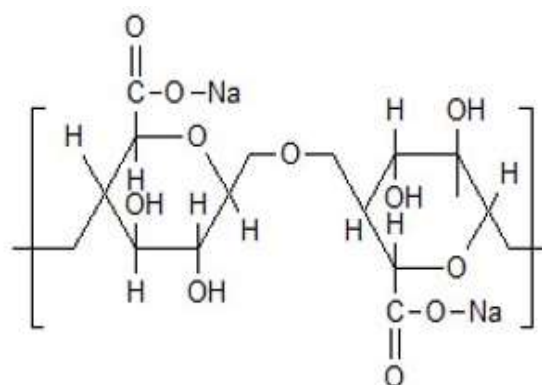


Figure 28: Chemical structure of SA.

SA is extracted as sodium salt from the cell wall of brown algae and has already had a great variety of application field before utilizing it for battery applications. It has mainly been used for textile (as dye color pulp or to enhance textile antibacterial properties), in cosmetics (emulsions, hydrogels), in food (food additive E401 thickening agent, packaging, modification of food texture) and biomedical applications (wound dressing, artificial skin, drug delivery). Its good gelling ability, stabilizing properties and high viscosity in water make it an attractive candidate for complex applications [166].

SA is a typical polyelectrolyte, it contains negative charges on its backbone which strongly influence its rheological behavior in solution [167]. The so-called “polyelectrolyte effect” is known to cause the typical upward bending of reduced viscosity versus concentration plot by intra-chain electrostatic repulsion of charges [168]. Several other properties, like spinnability are negatively influenced by this effect and have been tried to overcome by the addition of  $\text{Ca}^{2+}$  cations [169]. It was assumed that chain entanglement as intermolecular interaction could be improved by hydrogen bonds or electrostatic forces [169]. Typically, the polyelectrolyte dissociates in aqueous medium to form an anionic polymer in the case of SA. The rather rigid chain – caused by repulsion of negatively charged groups – is entangled with increasing salt concentration in solution. Figure 29 shows how the polyelectrolyte forms a rather rigid chain in a salt-free environment and a random coil in a salt-containing environment, arranging in sterically optimized position.

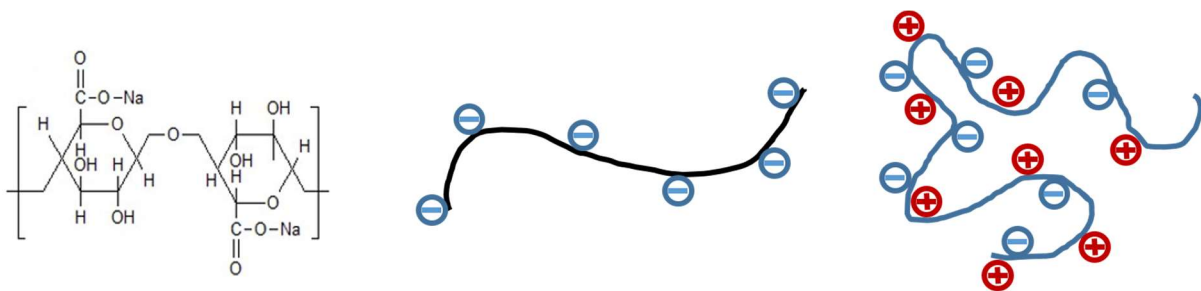


Figure 29: Chemical structure of SA (left) and its polyelectrolyte structure in salt-free (middle) and salt-containing environment (right). Reprinted from ref. [45] under the terms of the Creative Commons CC-BY license.

SA is under use as additive or main component in the broad field of batteries in a variety of different applications ranging from binder, separator, electrolyte up to membrane for fuel cells and many others.

The use of SA as electrolyte additive is by now limited to systems based on sodium, zinc, magnesium and aluminium, where in most cases SA hosts as a polymer network for the corresponding ions according to the type of battery.

As SA can both be woven and electrospun, the application as porous separator or membrane is somehow predestined. By now, nonwoven separators based on calcium alginate are even commercially available. Alginate-based fiber separators can be produced by standard fiber dissociators and sheet-forming machines [76], resulting in strong, thermally stable and environmentally friendly membranes. Its excellent thermal stability is a big advantage when comparing it to polyolefin-based ones, which tend to shrink at elevated temperatures, thus leading to the danger of short circuits within the battery.

### 3.2.3 Physicochemical and mechanical measurements

Figure 30 clearly visualizes the hydrophobic nature of CB, as its particles can be observed on the water surface – directly after and even during the mixing process. This is a known effect for water-based battery slurries [170].

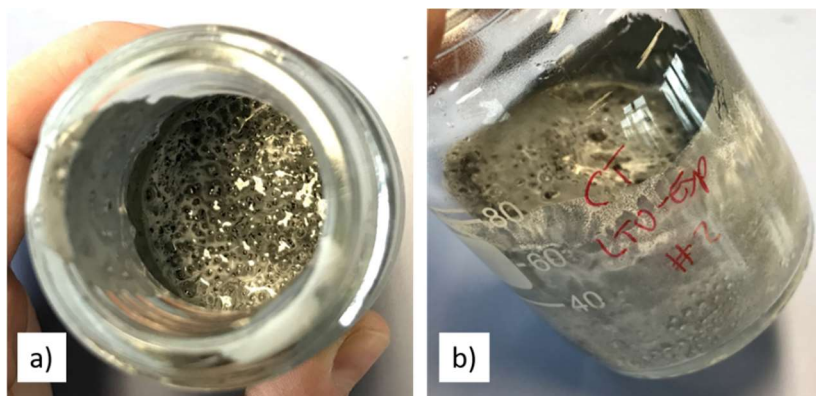


Figure 30: Photograph of de-mixing slurry with small particles of CB on water surface – directly after mixing. Reprinted from ref. [45] under the terms of the Creative Commons CC-BY license.

LTO obtains a quite low surface energy of less than  $2 \text{ J m}^{-2}$ , indicating very little elastic strain energy associated with coherent interfaces [171]. In contrast to this, for example LFP is known to own surface energies of  $219 \text{ mJ m}^{-2}$  which can in combination with its hydrophilicity lead to water capture in its voids and agglomerates and thereby also affect slurry viscosity [172].

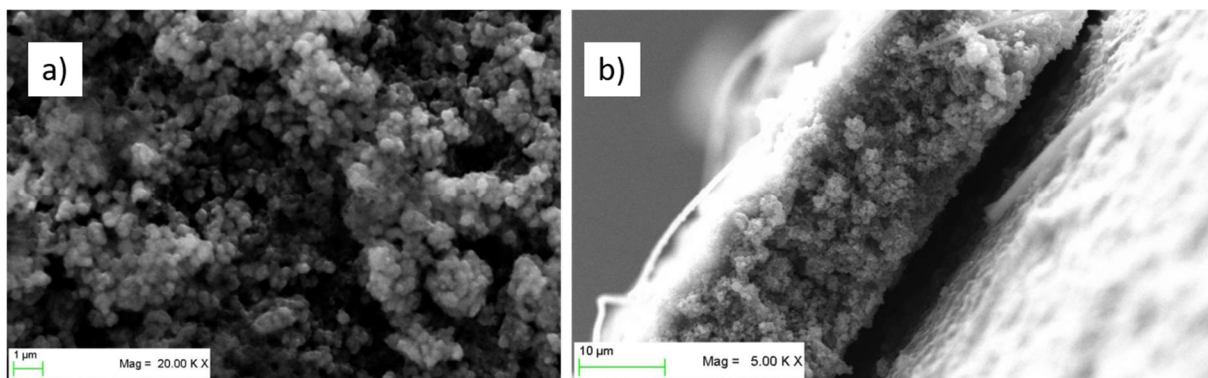


Figure 31: SEM images of LTO-SA electrode in pristine state (a) and after 80 cycles (b). Reprinted from ref. [50] under the terms of the Creative Commons CC-BY license.

Figure 31 shows the SEM images of LTO electrode containing solely SA as binder. The electrode appears well-mixed and shows a homogeneous material distribution without agglomerates.

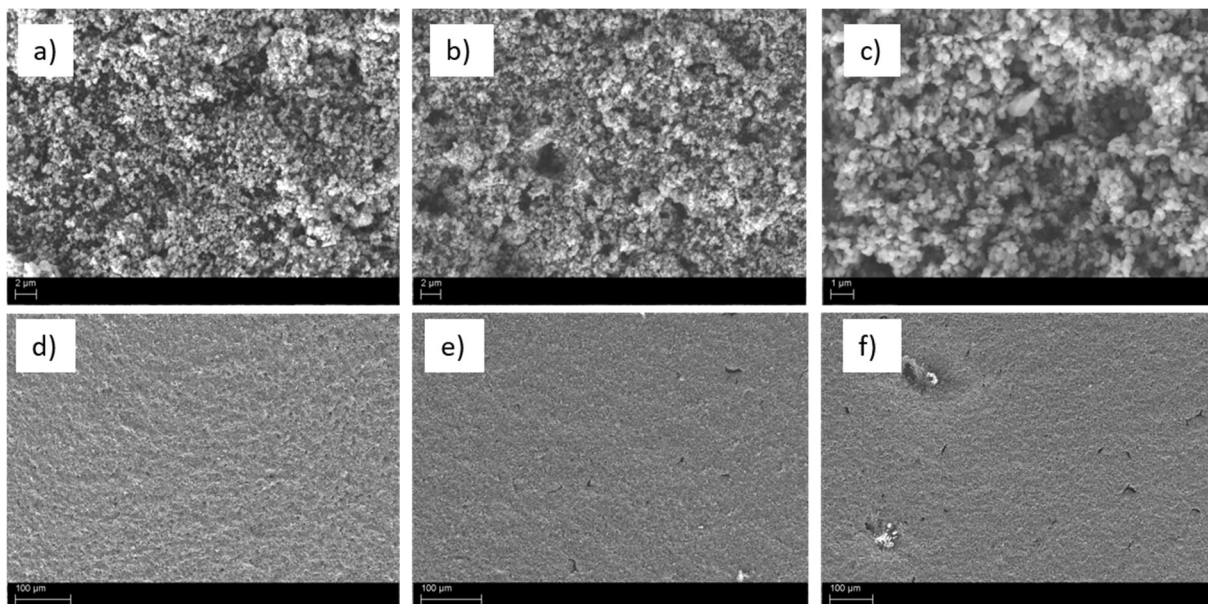


Figure 32: SEM pictures of SA3 (a,d), SAD1 (b,e) and SAD2 (c,f). Reprinted from ref. [45] under the terms of the Creative Commons CC-BY license.

SEM images of recipes SA3, SAD1 and SAD2 are performed to evaluate if there is an apparent difference in morphology between the recipe without (SA3) and with the two different dispersants (SAD1 and SAD2) and are displayed in Figure 32. Detailed images (a,b,c) did not reveal any morphological difference, but a closer look at the overview images (d,e,f) uncovers a difference in coated structure: coated electrodes containing one of the dispersants reveal a clearly smoother and more uniform surface in comparison to the electrode without.

A scheme on the general influence of detergent on active material particles is given in Figure 33, showing the stabilizing effect of the detergent due to particle separation, leading to a lower degree of agglomeration. Due to its bad electric conductivity, LTO implicitly needs a good and uniform CB distribution to ensure optimum connection. This can be positively influenced by the use of a detergent.

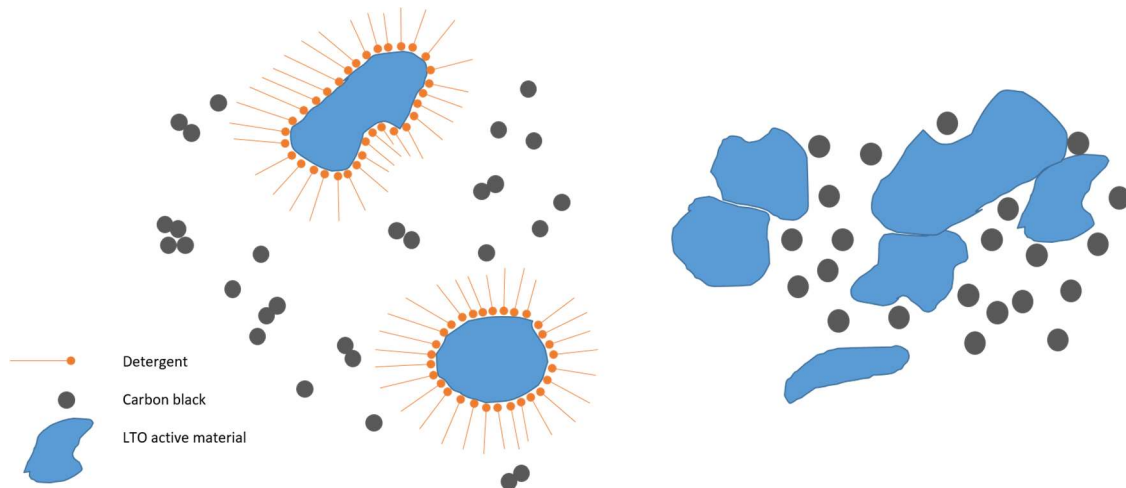


Figure 33: Scheme on detergent influence on active material particles (left: with detergent, right: without detergent). Reprinted from ref. [45] under the terms of the Creative Commons CC-BY license.

Table 11 summarizes mass shares of the detected element in the investigated electrodes; as presumed, high amounts of titanium, oxygen and carbon were found in comparable quantities for all three electrodes, contributing around 98 % of the detected mass share. Small amounts in the range of 0.39-0.44 % of sodium are originating from SA binder, whereas zirconium can be related to impurities. Figure 34 visualizes this finding, thus revealing no significant differences within the three samples.

Table 11: Mass-shares derived from EDX measurement.

	SA3	SAD1	SAD2
Element	mass-share [%]		
C	8.97	7.48	8.74
O	36.11	39.09	39.47
Na	0.38	0.43	0.44
Al	0.09	0.08	0.09
P	0.11	0.12	0.11
K	0.15	0.15	0.07
Ti	52.98	51.4	49.88
V	0	0	0.12
Zr	1.21	1.25	1.1

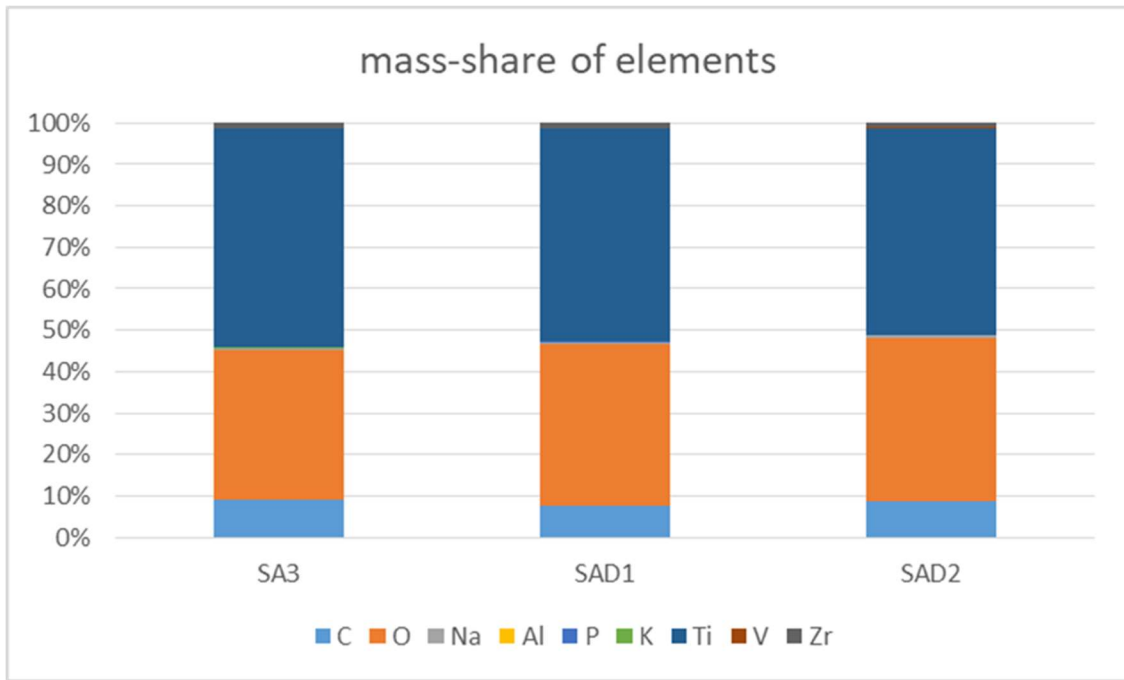


Figure 34: Graphical analysis of elementary mass-shares, derived from EDX-measurements.

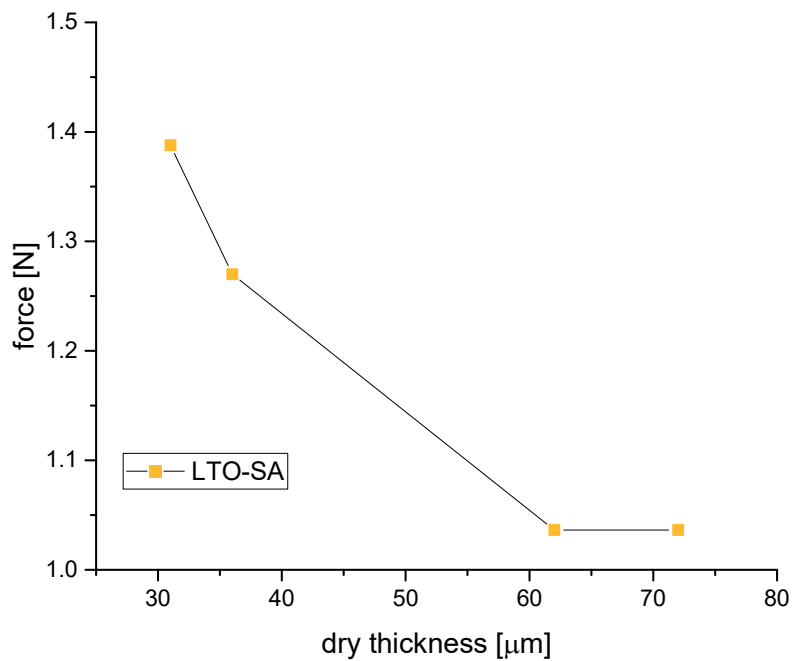


Figure 35: Result of peeling test for LTO-SA at different dry thickness.

Figure 35 gives the result of peeling test, showing some weaknesses at high electrode thickness above 60 μm. In general, a reduction of the required peeling force is observed with increasing electrode thickness. This is a well-known phenomenon based on slower drying due to a higher fluid fraction [173].

CA measurements are the preferred choice to investigate the wettability of surfaces. In general, a CA depends on how a liquid forms boundary with the solid states (substrates). This is mainly dependent on the substrate properties like composition and porosity, but also on the liquids surface tension. As depicted in Figure 36, several different droplet forms on a surface are possible. The droplet on the left, for example, has a very large CA as it does not at all spread over the surface [174], indicating a hydrophobic behavior. The scheme on the right gives a 2D cross-section of a droplet with marked CA.

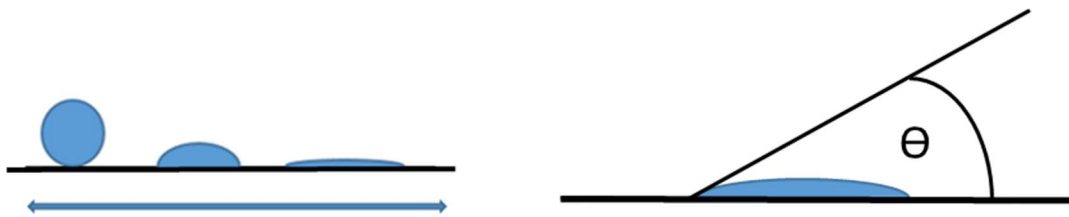


Figure 36: Different droplet forms on substrate (left) and CA measurement (right). Reprinted from ref. [45] under the terms of the Creative Commons CC-BY license.

Depending on the coating process, different viscosities are known to be beneficial. It was found out that a viscosity in the range of 3500 to 8000 mPa s is the optimum range for doctor blade coating processes.

In order to improve slurry stability, two different detergents were added to the battery slurry at a concentration of 0.5 %, namely a polymeric fluorochemical (FC4430, purchased from 3M) and an ammonium salt in water (AA4040, purchased from BASF). The perfluorinated dispersant is known to have a good electrochemical stability [175]. The anionic dispersant is also used to improve lithium-ion battery slurry processing [176].

### 3.2.4 Rheological properties of LTO-SA slurries

Several research groups have evaluated the rheological properties of SA [167,177,178], some with respect to its spinnability for electrospinning [165,169,179]. Rheological characteristics of LIB slurries can be found more frequently [180–183], but none of them deals with SA in combination with LTO as anode material. Both Garcia et al. and Cuesta et al. have studied alginate suspensions as binders for LIBs, but are using graphite as electrode material [97,170].

Phanikumar et al. investigated SA and polyvinyl alcohol as aqueous-based binders for LTO anodes, but did not present rheological properties [184]. As mentioned above, with an increasing demand of LIBs, cell chemistries besides graphite on the anodic side will be of strong interest for future developments.

The preparation of battery slurries is a challenging topic where a huge variety of different processes are combined and need to be coordinated. One crucial property is its optimum rheological behavior for the casting process onto the current collector [170].

The result of the mixing process is a battery slurry paste which is coated on the current collector, namely copper or aluminium foil. These are substantial steps where its rheological properties play an outstanding role, especially the maintenance of a stable battery slurry within time.

In order to gain a deeper understanding, the flow parameters of battery slurries need to be evaluated and balanced with the desired production method. Optimum slurry viscosity is indispensable for battery coating by defining the resulting electrochemical performance. A uniform distribution of materials leads to uniform porosity thus leading to optimized electrolyte penetration which has a decisive influence on electrochemical performance.

As reported in chapter 3.2 *LTO with sodium alginate binder*, the de-mixing of LTO-slurries containing SA as binder or part of the binder system [50] is known to take place. The topic of slurry stability was also addressed by Bauer et al. who investigated nanoscale LFP and micron-size NMP and came to the conclusion that a stabilization of active material particles can only be achieved by a suitable combination of polymeric binder and particulate additives [185]. Obviously, many battery materials are too large to be prevented from settling, even if they are stabilized as individual particles [185]. Ouyang et al. claimed three common strategies to improve the anti-settling stability of the slurry, namely including the application of electrostatic effects or spatial barriers to the particles, secondly, a reduction of the particles mobility by increasing the viscosity and third, the formation of a weakly coagulated state among the solid particles in the slurry [186]. A phase separation was also found by Garcia et al. where agglomerates began to form between CB particles and SA binder [170]. Furthermore, it was also found out that carbon binder from phenolic resin is able to decrease the geometric surface of CB particles as well as the free space of aggregates and agglomerates

[187]. A gel building ability of SA is reported only in the presence of cations, especially Ca<sup>2+</sup> ions which in general facilitate chain aggregation and gelation [188].

Looking at highly dispersed systems containing nanoparticles, one can find three-dimensional networks due to interactions between mineral layers and polymer chains which can be investigated by rotational rheometry in order to evaluate melt elasticity [189]. The used LTO particles are in a dimension of 700 to 1600 nanometers (D<sub>50</sub>), so no longer ascribed as nanoparticles. Nevertheless, the possibility of network formation can be examined by evaluation of slurry viscosity (indicating shear-thinning behavior) and storage modulus curves (indicating the formation of secondary plateaus) [189].

To visualize these effects including the reinforcement level as a result of three-dimensional network between SA polymer chains and LTO, a calculation of cumulative storage factor (CSF), as described by Kracalik [189], was conducted according equation 3-2:

$$CSF = \int_{0.1 \text{ rad/s}}^{628 \text{ rad/s}} G' / \int_{0.1 \text{ rad/s}}^{628 \text{ rad/s}} G'' \quad \text{Equation 3-2}$$

Using this novel analytical approach, internal material enforcement coming from internal molecular friction (change in viscosity, described by cumulative complex viscosity, CCV) can be divided from external reinforcement coming from 3D physical network – described by CSF.

One possible characterization method for the de-mixing of suspensions is the degree of flocculation, where the sedimentation of particles is measured. Due to the fact that LTO active material and graphite are of dark grey and black colour, this method could not be applied for our battery slurry. Therefore, we concentrated on both rheological and CA measurements.

### 3.2.5 Result of rheological measurements

In Figure 37, the results of viscosity test of LTO-SA directly after mixing and 24 hours later are illustrated. LTO-SA comes along with a very high viscosity of nearly 8000 mPa s at lowest shear rate and decreases with increasing shear rate.

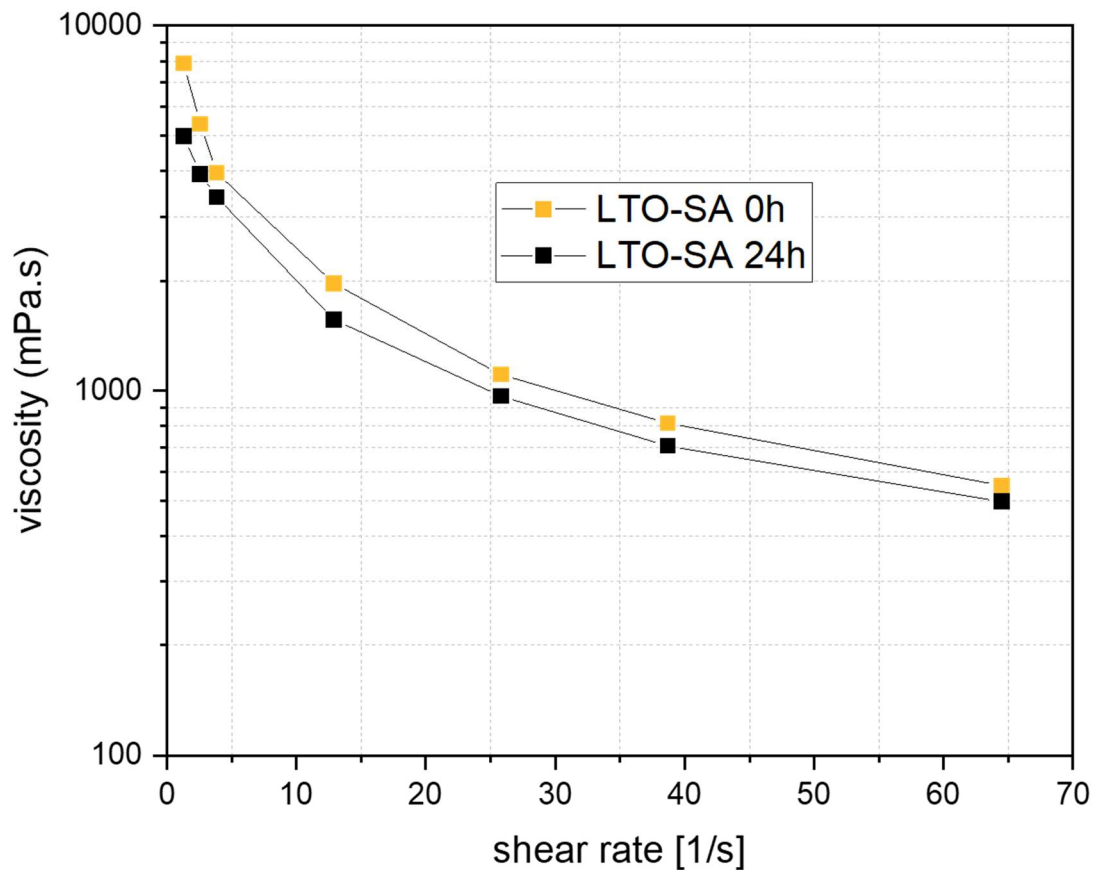


Figure 37: Viscosity as a function of shear rate for LTO-SA slurry directly and 24 hours after mixing.

Figure 38 depicts the three different LTO slurries containing only SA and the two different dispersants in terms of shear rate vs shear stress. The slurries showed dilatant behavior increasing with shear rate. The addition of a dispersant leads to lower shear stresses compared to the bare LTO-SA slurry leading to the suggestion, that both dispersants are able to reduce shear stress within the slurries.

During the experiment, shear stress increased in the following order SAD2 < SAD1 < SA3.

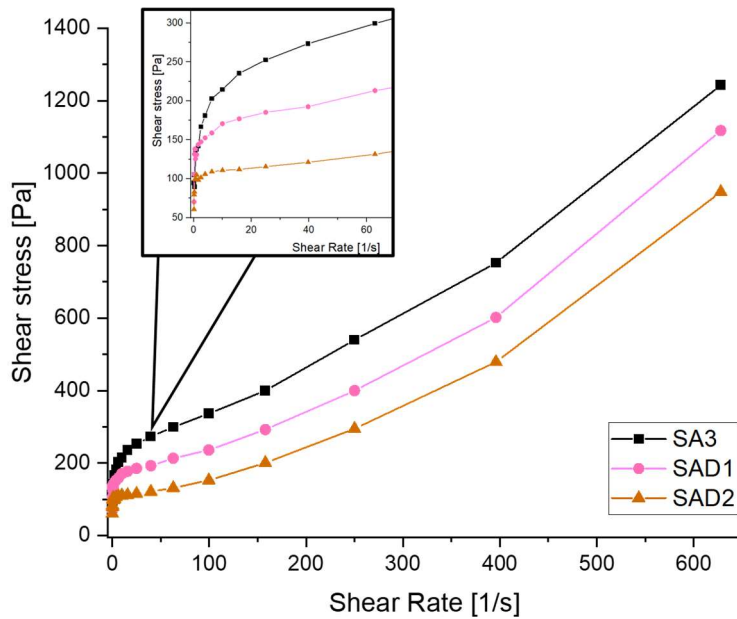


Figure 38: Shear stress vs shear rate for different SA-LTO slurries. Reprinted from ref. [45] under the terms of the Creative Commons CC-BY license.

As shown in double-logarithmic Figure 39, viscosity decreases with increasing shear rate, which is a typical shear-thinning behavior caused by the disentanglement of polymer chains. At elevated shear rate, viscosity is increasing with shear rate – the so-called dilatancy or shear thickening behavior caused by the formation of clusters leading to an increase of viscosity. This behavior is clearly visible for slurries without active material, namely mixtures of SA in water and SA in water with CB.

What is also apparent at first glance is the fact that the addition of CB massively influences slurry viscosity. The critical shear rates for the shift between shear thinning and shear thickening behavior is thereby shifted from  $8 \text{ s}^{-1}$  to  $30 \text{ s}^{-1}$  dependent on temperature. This shift in viscosity is also taking place for more complex slurry compositions showing an overall stable behavior. Compared with the influence of temperature, the detergents seem to have minor influence on slurry viscosity.

Obviously, the detergents do not significantly affect slurry viscosity and show similar results both in the size of magnitude and pseudoplastic feature.

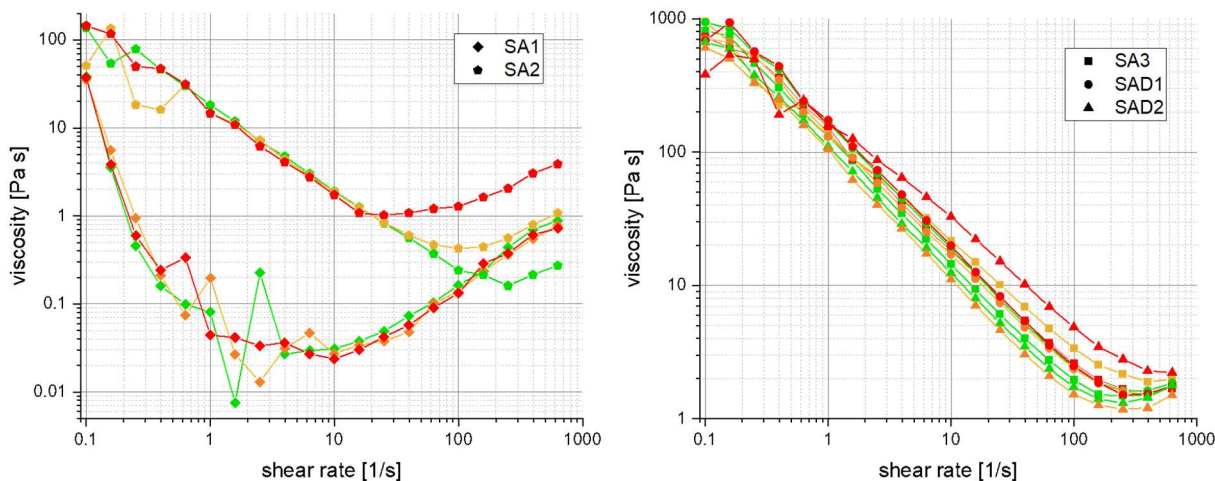


Figure 39: Shear rate vs viscosity for slurries at different temperatures. Green = 20 °C, orange = 30 °C, red = 40 °C. Reprinted from ref. [45] under the terms of the Creative Commons CC-BY license.

For frequency sweep measurements, depicted in Figure 40, the storage modulus  $G'$  dominates over the loss modulus  $G''$ , which is a typical behavior for gel type systems [185], indicating a three-dimensional network within the slurry mixture. Both  $G'$  and  $G''$  reveal highest values for SA3 30 minutes after preparation being the complete LTO-SA slurry without dispersant. Slurries containing FC4430 as dispersant show lowest values both directly after preparation and 30 minutes later.  $G'$  showed rather low slopes up to an angular frequency of about  $100 \text{ s}^{-1}$ , followed by a nearly exponential slope for the samples directly after mixing. This indicates a formation of  $G'$  secondary plateau reflecting a strong physical network in the system, this indicating an interaction of the LTO particles with SA. This so called “rubber like behavior” indicates to which acting force the physical network/gel structure is stable. Defining a yield point as the crossing of  $G'$  and  $G''$  curves leads to the assumption that only SAD1 and SAD2 own a yield point at an angular frequency of about  $400 - 500 \text{ s}^{-1}$ .

In contrast to the exponentially increasing slope of un-settled slurry mixtures storage modulus at angular frequencies above  $100 \text{ s}^{-1}$ , the slopes of dormant samples containing a dispersant (SAD1 and SAD2) dramatically decreased when settled for 30 minutes. Due to a maximum measured angular frequency of  $628 \text{ rad}$ , the behavior of SA3 sample without dispersant cannot be predicted.

In contrast to Figure 39, a dependency of slurry stability on the use of detergents is visible in Figure 40, at least for the measurements after 30 minutes. The decreasing storage factor

evidences a decrease in stability at elevated angular frequencies, assuming a non-beneficial detergent influence.

The frequency-dependent modulus indicates that a gel structure in the slurry does no longer exist above a critical acting force demonstrated in this case as a shear rate [183].

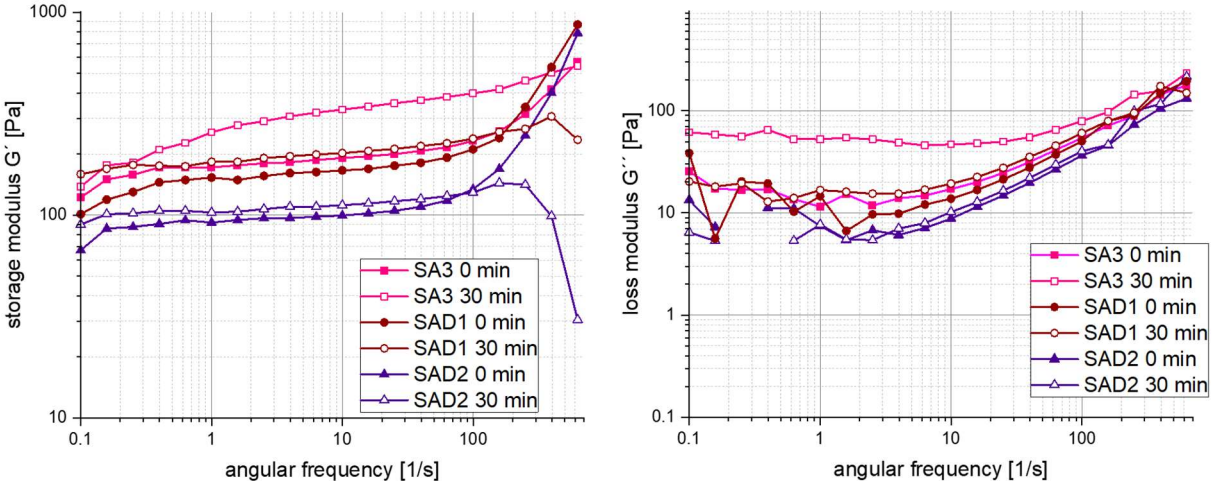


Figure 40: Storage and loss modulus for three different SA-based slurries. Reprinted from ref. [45] under the terms of the Creative Commons CC-BY license.

The results of CSF evaluation by integrating over  $G'$  and  $G''$  according to equation 3-2 are shown in Table 12 and visualized in Figure 41.

Table 12: Cumulative complex viscosity (CCV) and cumulative storage factor (CSF) for all tested slurries.

	Cumulative complex viscosity	Cumulative storage factor [G'/G'']
SA3 30 °C	1814.19	5.095
SA3 40 °C	2428.33	5.372
SA3 50 °C	2091.56	5.146
SAD1 30 °C	2173.85	5.248
SAD1 40 °C	1992.14	5.452
SAD1 50 °C	2182.24	6.270
SAD2 30 °C	1626.29	5.873
SAD2 40 °C	1431.91	5.125
SAD2 50 °C	3176.76	5.696

Plotting CSF over CCV shows a stable regime at medium values of 1800 – 2400 for CCV. In this area, mostly slurries without detergent (SA3) are located, indicating an inverse behavior of the detergent, thereby showing no stabilizing effect. This finding is in accordance with storage and loss modulus evaluation and also confined by shear rate and shear stress results.

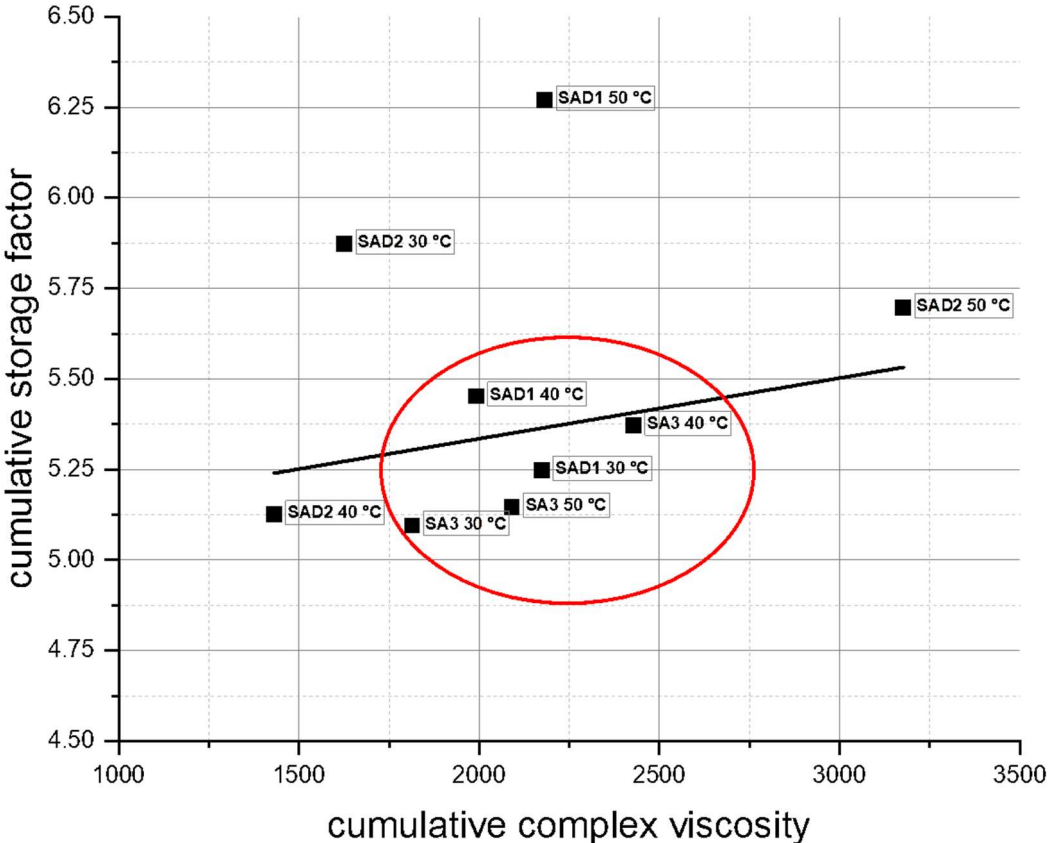


Figure 41: Cumulative complex viscosity vs. cumulative storage factor for all tested slurries. Reprinted from ref. [45] under the terms of the Creative Commons CC-BY license.

### 3.2.6 Result of contact angle measurements

Results of CA measurements of mixtures upon aluminium foil are depicted in Table 13. It can be seen that both detergents have an impact by lowering the CA and can thereby improve slurry stability by lowering viscosity. Figure 42 gives some exemplary measurements upon aluminium foil, also indicating a higher CA for the LTO-slurry without detergents. The sharply decreasing standard deviation, as depicted in Figure 43, for slurries containing detergents is noticeable and clearly indicates a stabilization of slurry properties in general when comparing it to the slurries without detergent.

Table 13: Results of CA measurements

Recipe code	Medium CA [°]	Standard deviation
SA1	63.1	12.5
SA2	60.1	4.8
SA3	74.7	6.8
SAD1	66.26	3.0
SAD2	55.7	2.6



Figure 42: CA measurements, exemplary for SAD2 (54.98 °), SAD3 (66.77 °) and SA3 (74.17 °). Reprinted from ref. [45] under the terms of the Creative Commons CC-BY license.

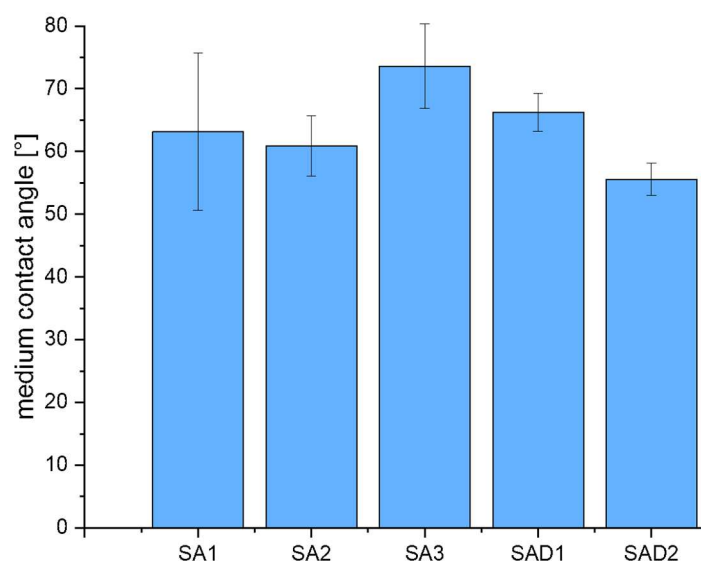


Figure 43: medium CA for different tested slurries, equipped with error bars. Reprinted from ref. [45] under the terms of the Creative Commons CC-BY license.

### 3.2.7 Electrochemical measurements

For the sake of clarity and comparability, these measurements are presented in chapter 3.3.4

*Electrochemical measurements* together with the results of electrochemical measurements for LTO-PVDF/SA and LTO-PVDF/CMC electrodes.

### 3.3 LTO with mixed binders: comparison between PVDF/SA and PVDF/CMC

Evaluating polymer characteristics from chapters 1.3.3.4 *Binder* and 3.1 *Graphite with PVDF binder*, it is suggested that a combination of water-based PVDF binder and either CMC or SA should lead to promising results concerning cyclability and stability of the electrode, by taking advantage of both binder types. Each one of these binders is eco-friendly and the whole processing can be performed without the use of organic solvents.

In this chapter, the use and combination of the different water-based binders mentioned above to prepare LTO electrodes is reported, which were tested in half-cell configuration. The electrodes were successfully coated upon aluminium foil. The prepared electrodes were tested mechanically and electrochemically in 1 M LiPF<sub>6</sub> in EC/DMC 1:1 in half cell vs. Li, and showed an overall stable coating combined with a good cycling stability and rate capability up to 5 C.

*MDPI is acknowledged for the permission to reprint parts of the following publications:*

C. Toigo, M. Biso, K.-H. Pettinger, C. Arbizzani, "Study on Different Water-Based Binders for Li<sub>4</sub>Ti<sub>5</sub>O<sub>12</sub> Electrodes" *Molecules*, 25, 2443 (2020)

C.Toigo, M.Krakalik, E.Bradt, K.-H.Pettinger, C.Arbizzani, "Rheological properties of aqueous sodium alginate slurries for LTO battery electrodes" *Polymers*, 13, 3582 (2021)

### 3.3.1 Chemical properties and application fields of CMC

CMC, as depicted in Figure 44, is a frequently used water-based binder for various battery applications, especially on the cathode side. Based on its structure and to be able to compare it with SA, it is a weak polyacid. It is a cellulose derivative, consisting of  $\beta$ -linked glucopyranose residues with varying levels of carboxymethyl substitution, which is responsible for its aqueous solubility in contrast to insoluble cellulose [190]. It is produced from the insertion of carboxymethyl groups into natural cellulose and has a strong shear-thinning behavior. [191].

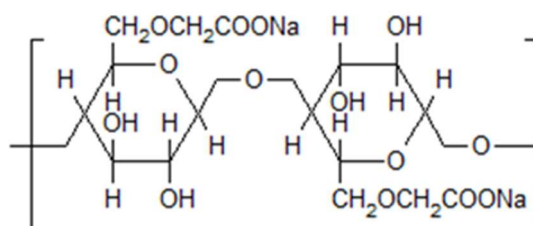


Figure 44: Chemical structure of CMC.

CMC is also known to play a key role as thickening agent to prevent graphite particles from settling during processing, which can be related to its particle size [190]. As CMC is known to be very stiff, it is usually combined with an elastomer like SBR, to provide a suitable flexibility for battery applications.

### 3.3.2 Physicochemical and mechanical measurements

The two types of pristine and cycled LTO electrodes were examined by SEM and the obtained images are shown in Figure 45. The electrodes appear well-mixed and show a homogeneous distribution of the materials in case of the pristine electrodes.

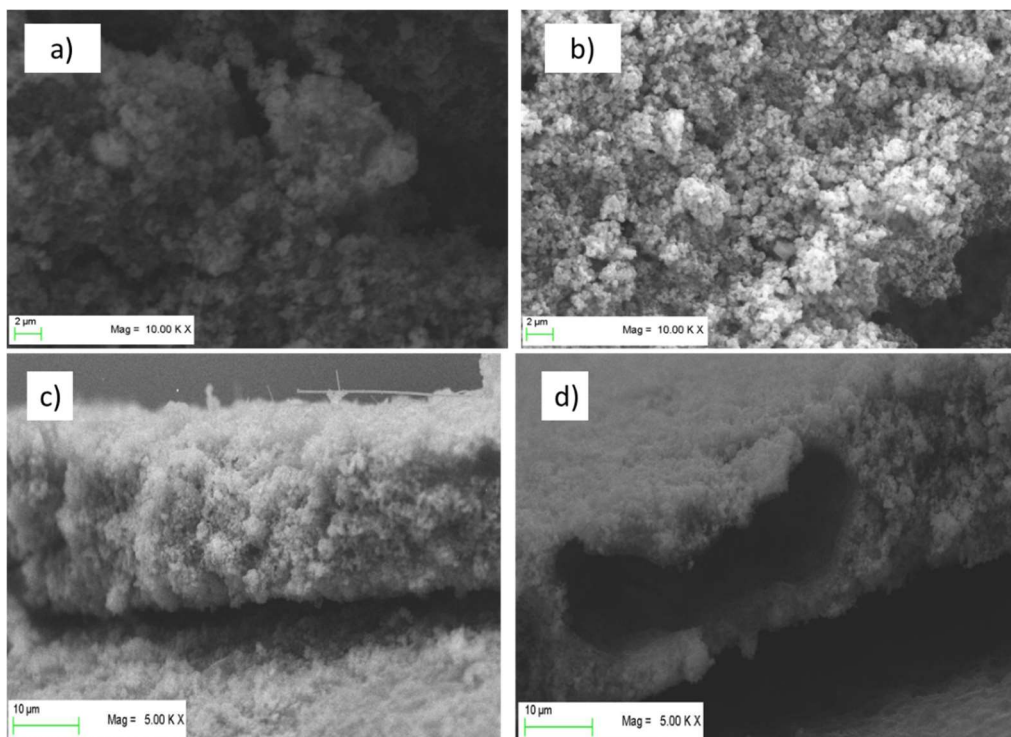


Figure 45: SEM images of the two types of pristine electrodes: (a,c) LTO/PVDF-CMC and (b,d) LTO/PVDF-SA. Reprinted from ref. [50] under the terms of the Creative Commons CC-BY license.

Furthermore, no agglomerates of materials are visible. Although the electrodes showed very good mechanical stability during processing (punching and placing in half-cell apparatus), this was tested further by cross-section SEM and a peeling test.

While LTO-PVDF/CMC electrode shows a homogeneous distribution of the particles for recipes, LTO-PVDF/SA displays an enormous hole in the dimensions of about  $8\ \mu\text{m} \times 20\ \mu\text{m}$ . Holes of this dimension were only found for this recipe and are suspected to be caused by insufficient degassing before the coating step combined with a very active swelling behavior of both PVDF and SA binders, leading to a worse interconnection between active material and binder up to a complete contact loss within the electrode. The SEM images also display residues of the glass fiber separator on the electrode surface due to the tight packing within the half-cell arrangement.

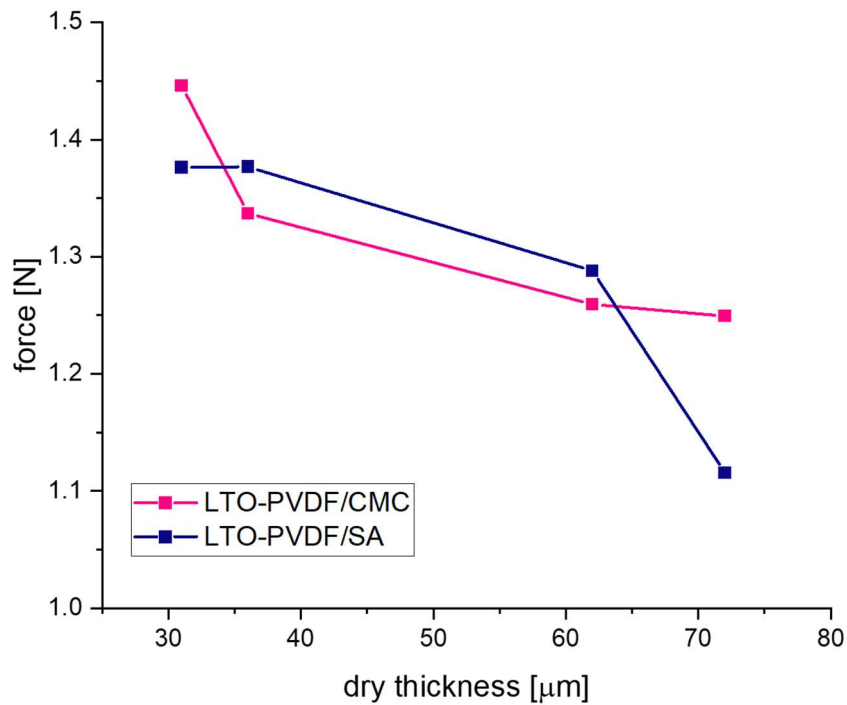


Figure 46: Result of peeling test for LTO-PVDF/SA and -PVDF/CMC electrodes at different dry thickness

Peeling tests reveal the strength of blended binder mixtures in comparison to pure SA, as can be seen in Figure 35 and Figure 46. Both combined binder systems perform remarkably better at dry thickness of more than 35 microns. In general, a reduction of the required peeling force is observed with an increase of the electrode thickness, which is a well-known phenomenon based on slower drying since the slurry contains a higher fluid fraction [173]. The addition of PVDF binder improves the adhesive and cohesive binding properties, leading to mechanically more stable electrodes.

### 3.3.3 Rheological measurements

To evaluate slurry stability, a viscosity test was performed for all slurries in different time ranges: after mixing, 24 h after mixing and seven days after mixing, as depicted in Figure 48. The results are displayed in Figure 47 and show some very interesting properties, especially when comparing it with pure SA binder, as can be seen in Figure 37. The viscosity of SA slurries was higher than any of the PVDF mixtures for shear rates between 1 and 10  $s^{-1}$ . Quite similar viscosity values for all slurries are reached for shear rates above 10  $s^{-1}$  up to 65  $s^{-1}$ . One interesting aspect is the difference in viscosity after 24 hours: it decreased for all different types of slurry and it has to be mentioned that this effect is mostly visible at low shear rates. The SA-containing slurries displayed a much higher change in viscosity than the one without SA, probably caused by a slight de-mixing, as can be seen in Figure 48. In general, a higher viscosity is known to prevent LTO particles from sedimentation and aggregation during electrode fabrication when water is evaporating. This leads to a high uniformity of the slurry [94].

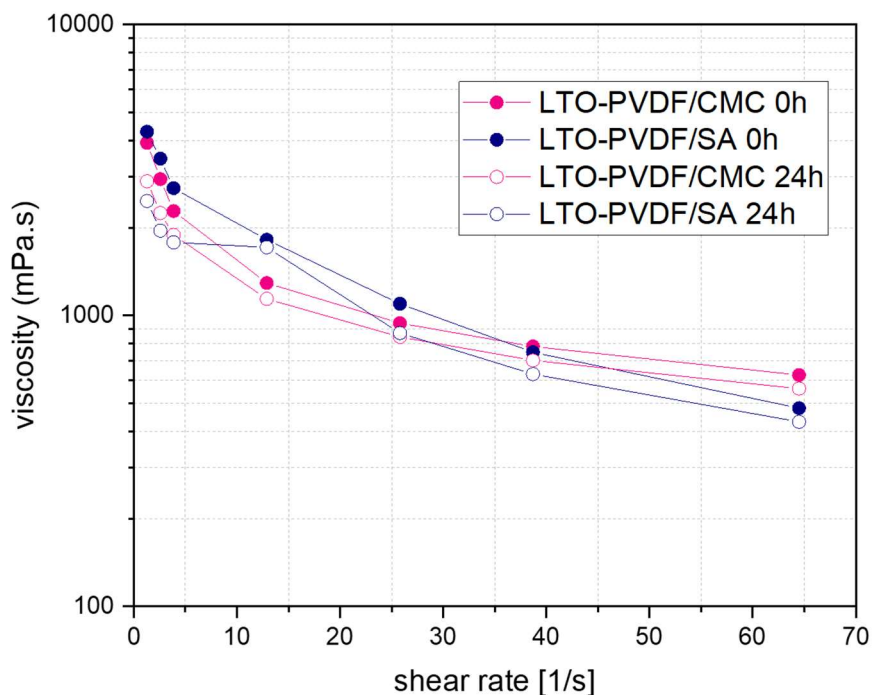


Figure 47: Viscosity as a function of the shear rate for different slurries: (a) directly after mixing and (b) 24 hours after mixing.

The higher viscosity of the SA-slurries at low shear rates appears as an indicator for a good network structure, but the effect is relativized at higher shear rates which are necessary for

coating. Concerning the coating procedure, a higher slurry viscosity requires lower coating speeds in order to establish a better contact between the slurry and the current collector foil. Furthermore, alginate macromolecules are much more polar than the CMC polymer chains, which can ensure better interfacial interaction between the polymer binder and the particles [94]. On the contrary, the results of peeling tests show a very different picture, most likely caused by high shear rates during coating.

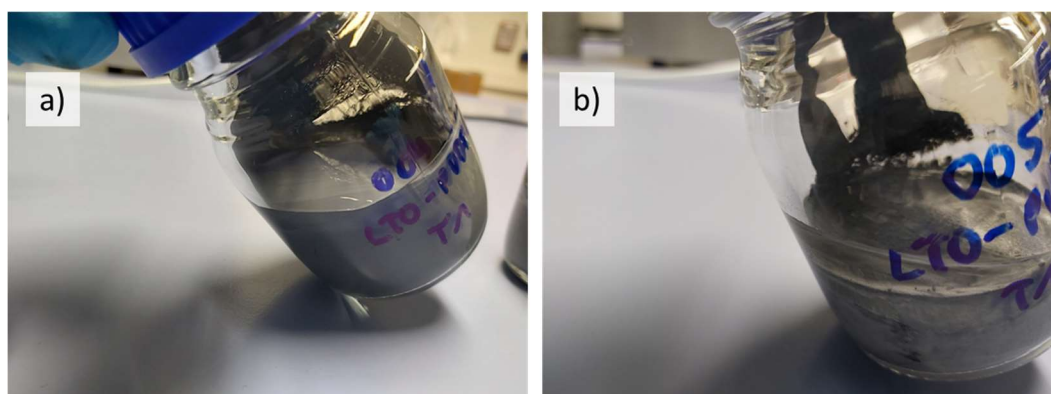


Figure 48: Difference between the slurries seven days after mixing containing (a) LTO-PVDF/CMC and (b) LTO-PVDF/SA binder systems. Reprinted from ref. [50] under the terms of the Creative Commons CC-BY license.

Charge-discharge profiles of the different electrodes show a weak performance of the LTO-SA binder system at high C-rates. Furthermore, we assume local pH incompatibilities between PVDF and SA leading also to the strong fading behavior in electrochemical tests.

### 3.3.4 Electrochemical measurements

Figure 49 shows the charge-discharge curves of LTO anodes at different C-rates in the voltage range of 1.0-2.2 V, where 1C equals the theoretical capacity of  $175 \text{ mAh g}^{-1}$ . Furthermore, the delivered discharge capacities of LTO anode half cells are clearly visible and show up with 162 (92.6 % of the theoretical capacity), 149 (85.1 %) and 145 (82.9 %)  $\text{mAh g}^{-1}$  at 0.333 C-rate with PVDF-CMC, SA and PVDF-SA binders, respectively. When charged and discharged repeatedly, the different water-based electrodes show stable capacities up to 5 C, but a quite considerable fading occurs when the PVDF/SA binder (Figure 50b) is observed. Figure 49a shows a combined C-Rate and cycling test starting with each three galvanostatic cycles at 0.33/0.5/1/3/5 and 10C followed by 80 cycles at 1C. Indeed, the binder containing PVDF/SA is

retrieving significant fading at 84.8 % of the initial capacity for 50 cycles and 73.9 % for 100 cycles taking the very first one as reference cycle. Having a look at Figure 45, one can assume that the bad electrochemical behavior is caused by the poor electrode structure and the associated bad electrical conductivity, probably resulting in a contact loss between electrode and current collector.

From the electrochemical point of view, the combination of PVDF/CMC produces electrodes that deliver the best results both for cycling stability and C-rate capability. This result means that some reasons for the different behavior of PVDF/CMC and PVDF/SA have to be considered. On the one hand one might expect a similar behavior due to the fact that CMC and SA have a quite similar structure and are combined with the same fluoropolymer. On the other hand, one has to consider that for CMC, the presence of the carboxymethyl groups is responsible for the aqueous solubility. It is a weak polyacid exhibiting pH-dependent dissociation forming anionic carboxylate functional groups [190]. With an increasing percentage of SA within a mixture, the swelling ratio increases, probably attributed to an increase in electrostatic repulsive force in the network because of negatively charged carboxylate functional groups [99], which can lead to a less sufficient binder-particle connection. The stiffness and swelling ability of SA also depends on the sequence and composition of the alginate chain due to the differences in the stereochemistry of mannuric and guluronic acid monomers, as well as on the electrostatic interactions with cations in solution [188]. Due to a higher polarity of SA compared to CMC polymer chains, a hindering of both binders in the combination PVDF/SA is another possible mechanism leading to the bad electrochemical results of this recipe [94].

Therefore a negative interaction of PVDF with SA is suggested, regarding their swelling behavior. The medium crystallinity of the used PVDF binder (30% of polymer chains) means that 70 % of the binder's polymer chains are in amorphous state and are therefore able to perform swelling. In these swollen regions, the electrolyte can easily penetrate into the composite electrode and ensure a good ion transport. This leads to the suggestion that a crystallinity of 30% results in smaller proportions of the binder having the ability to share electrical conductivity with the active material, since swelling only occurs in amorphous regions [49,96]. The high electrolyte uptake of PVDF due to its flexible linear chains [192] and long-term soaking of the electrolyte during battery storage and cycling [100], combined with

the good swelling ability of SA in water, leads to worse electrochemical results. Firstly, it can hinder the interaction of the binder with the active material and secondly, cause the particles to lose contact within operation of the battery, leading to a lower conductivity and a degradation of battery performance.

In contrast, a combination of PVDF and CMC shows very promising results. PVDF with its good wettability toward polar electrolyte solutions easily performs the Li ion transport [193]. Furthermore, the strong hydrogen bonding of the carboxyl and hydroxyl groups in CMC with the active material and the current collector seems to be a perfect complement for the PVDF binder, which only forms weak hydrogen bonds [95].

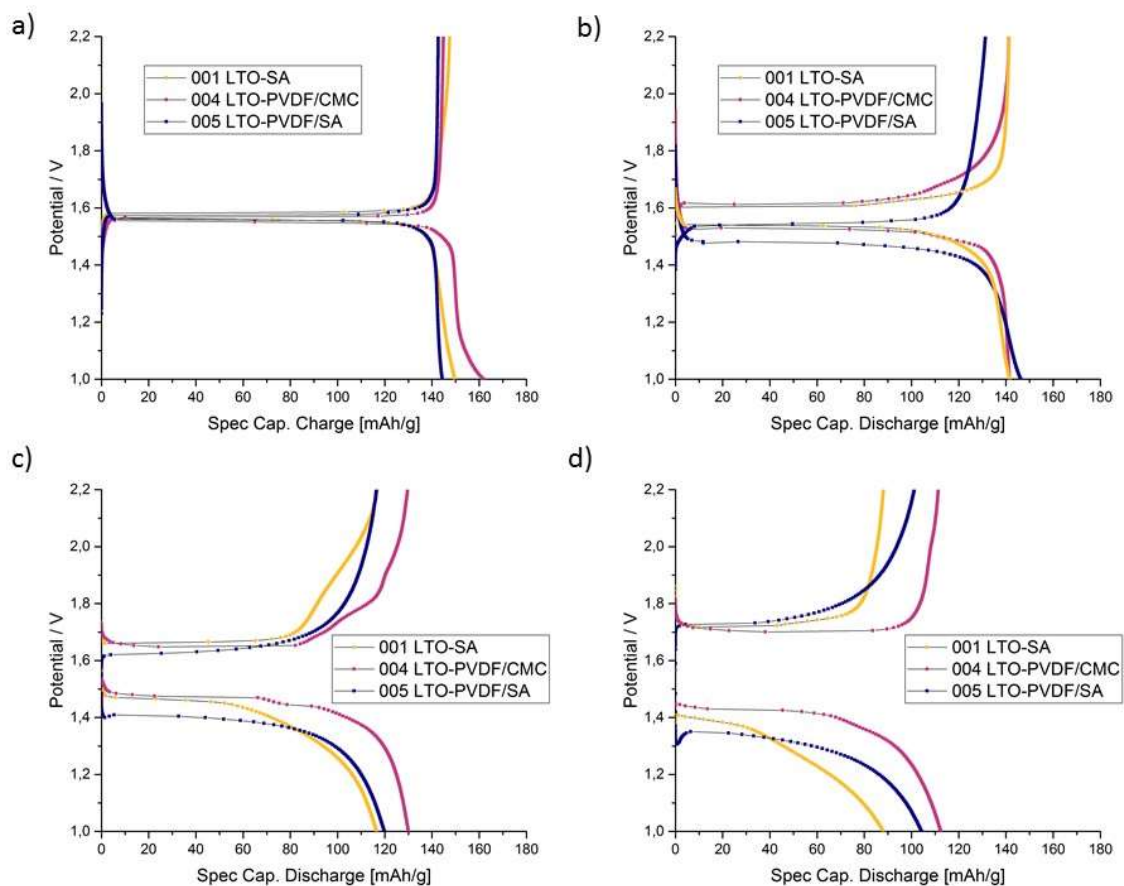


Figure 49: Charge-discharge profiles of LTO anodes at (a) 0.33 C, (b) 1 C, (c) 5 C and (d) 10 C. Reprinted from ref. [50] under the terms of the Creative Commons CC-BY license.

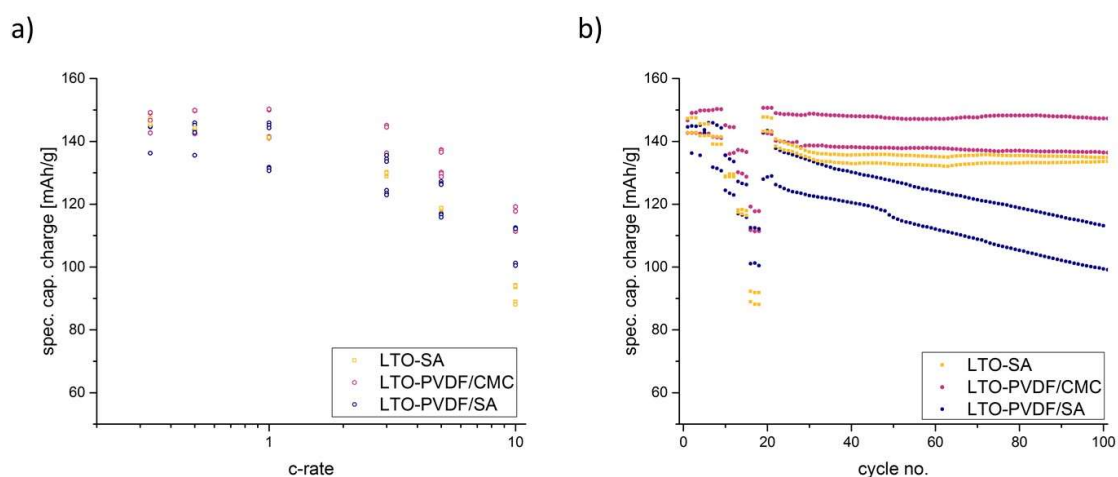


Figure 50: Electrochemical performance during C-rate test (a) and charge capacities for each of 2 exemplary electrodes (b). Reprinted from ref. [50] under the terms of the Creative Commons CC-BY license.

### 3.3.5 Electrode fading

The high and nearly linear fading of LTO-PVDF/SA (as can be seen in Figure 50b) can also be a hint for a bad adhesion of the electrode upon the collector foil, thus resulting in worse capacity cycle by cycle. Moreover, a kinetic difference is indicated between the PVDF and CMC binders; electrodes containing solely CMC binder have a much lower charge transfer resistance, a lower apparent activation energy and a lower apparent diffusion activation energy than electrodes containing PVDF binder [194].

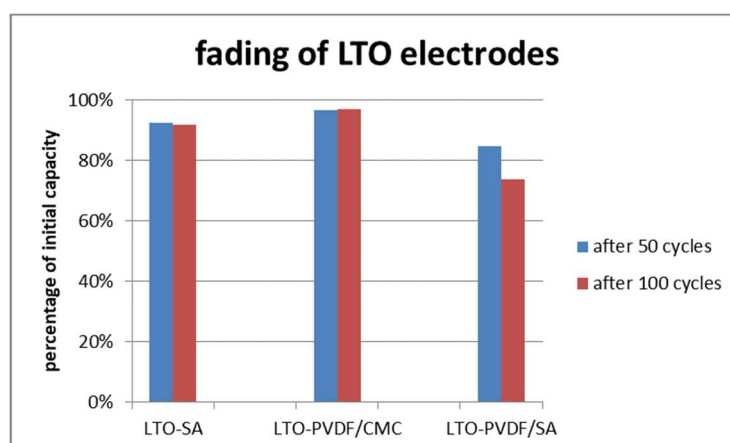


Figure 51: Fading of LTO electrodes with different binders. Reprinted from ref. [50] under the terms of the Creative Commons CC-BY license.

### 3.3.6 Conclusion

The tested electrodes were prepared by a completely water-based, environmentally friendly method. LTO anodes with SA, PVDF/CMC and PVDF/SA binder systems were successfully coated upon aluminium foil using conventional slurry and electrode coating techniques. The prepared electrodes were tested mechanically (peeling test and bending test) and electrochemically in half-cell configuration. LTO anode with PVDF/CMC binder system showed an overall highly stable coating. Neither cycling stability nor rate capability resulted in significant differences for C-rates up to 1C, whereas for high C-rates the advantages of PVDF/CMC binder systems are showing up clearly. This promising processing of completely water-based binder systems shows a possible way for the production of ecologically safer batteries.

## 4 Improved current collector surfaces for LTO electrodes

The effect of a galvanically structured copper current collector foil (SeCu58 with treatment) on the performance of LTO electrodes in comparison with a non-treated copper foil (SeCu58 blanc) is reported. The recipes' frame parameters (10 % of conducting additives, 7 % of binder, low loading of 0.5 mAh cm<sup>-2</sup>, and viscosity below 2000 mPa s) have been adopted to the question of whether an improvement in general can be achieved. So it is likely to minimize possible external influence factors like a limitation by electrical conductivity within the electrode coating or a limitation by Li-ion-diffusion.

*Elsevier is acknowledged for the permission to reprint parts of the following publications:*

C. Toigo, M. Frankenberger, N. Billot, C. Pscherer, B. Stumper, F. Distelrath, J. Schubert, K.-H. Pettinger, C. Arbizzani, „Improved LTO electrodes by modified current collector surfaces” *Electrochimica Acta* 392, 138978 (2021)

## 4.1 Influence of active material size

First results showed that platelet-shaped graphite with a particle size (D50) in the range of 22.8 microns is not the ideal material to be applied upon this type of galvanically structured current collector. This finding is mainly based on the fact that the nodule structure of the copper foil is taking place in a dimension of 200 nanometers which is clearly smaller than the particle size of 22.8  $\mu\text{m}$  of the graphite. This fact is illustrated by Figure 51. Therefore experiments have been carried out with (nano-sized) LTO as anode material with a particle size D90 below 10 microns.

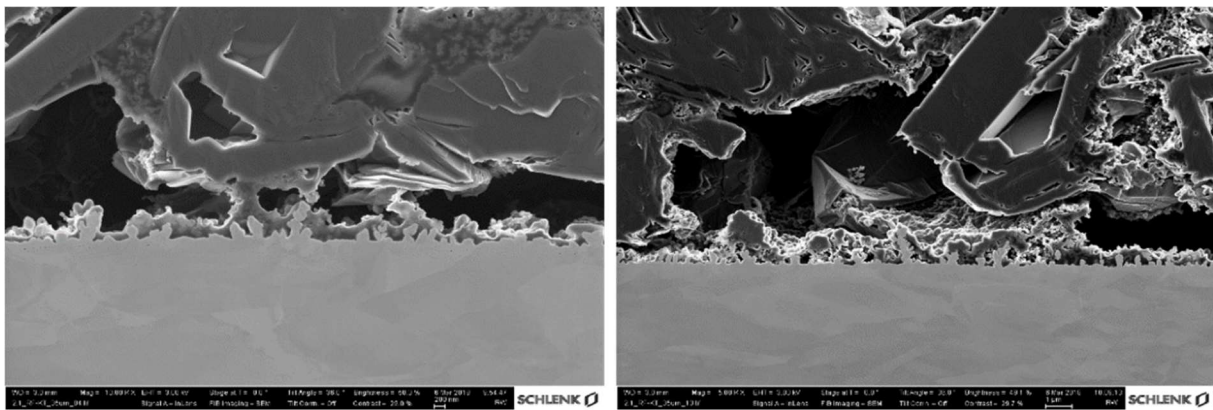


Figure 51: SEM of dendritic foil covered with graphite particles. Reprinted from ref. [29] under the terms of the Creative Commons CC-BY license.

## 4.2 Physicochemical and mechanical measurements

The copper foils coated with the electrode slurry were examined by FIB/SEM and the obtained images are shown in Figure 52. The untreated copper foil has a very smooth and clearly defined surface, whereas the modified foil shows distinct copper dendrites. A significantly improved connection between the LTO particles and dendritic copper foil is visible at first sight. The false colour image clearly confirms and illustrates this fact. It appears that the small LTO particles allow a higher amount of binder and CB to reach the treated foil and thereby enable some sort of mechanical anchoring. The particles marked in green represent binder and conductive additives and seem homogeneously dispersed within the composite

electrode. The blue marked active material LTO is in good contact with binder/conductive additives and the copper collector foil.

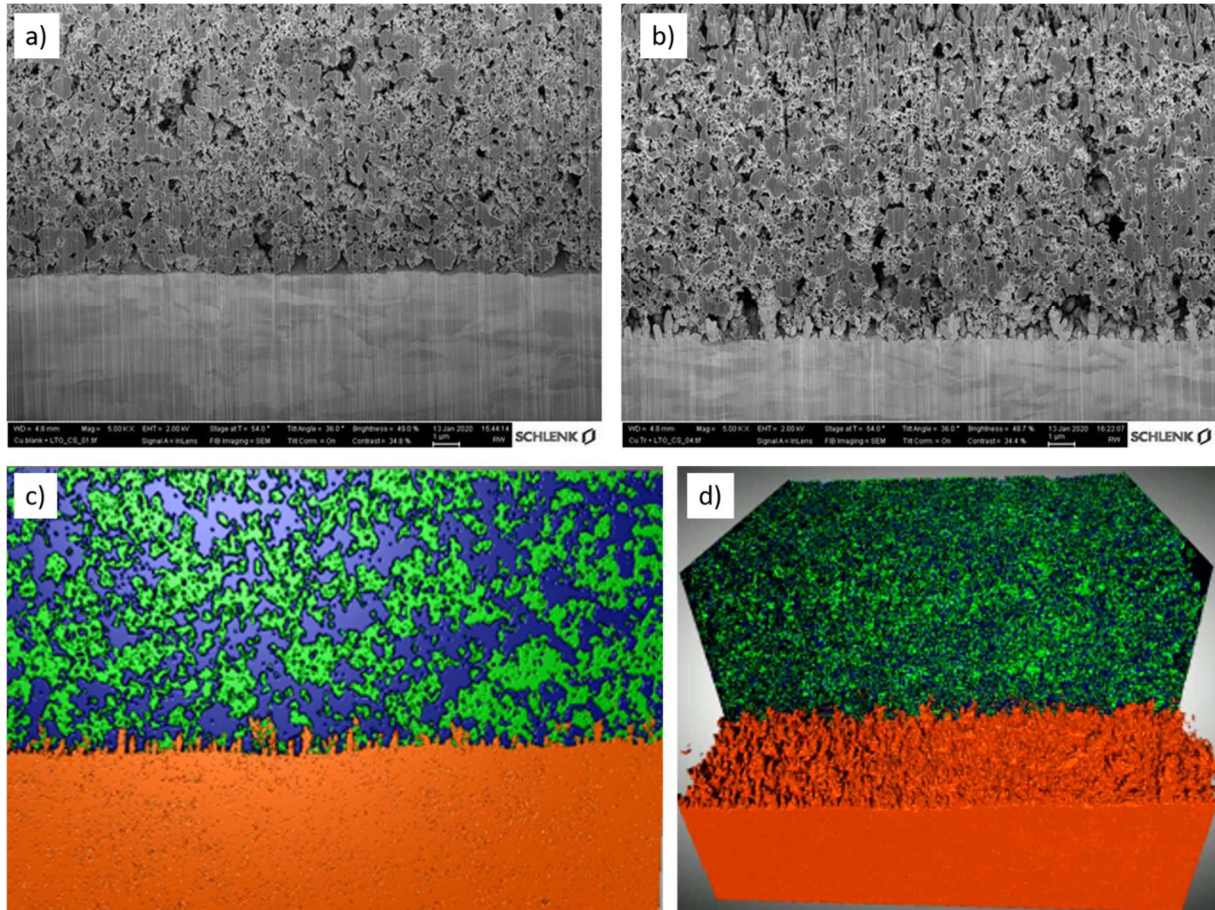


Figure 52: FIB-SEM images of untreated (a) and dendritic (b-d) copper foil. Colour map false colour images (c) and d): orange = copper, blue = LTO, green = binder and conductive additive. Reprinted from ref. [29] under the terms of the Creative Commons CC-BY license.

To evaluate the effect of different morphology and dimensions, both active material flakes of graphite and nano-sized LTO were used and examined by FIB-SEM, as depicted in Figure 52.

Figure 53 schematically shows how different particle sizes are able to connect with the treated copper foil. Obviously, the graphite active material in micrometer-range is too large to fit into the dendritic structure, and therefore mainly the binder attaches the copper surface - the over-sized active material can only reach the tips of the dendrites. Thus, no increased contact area between LTO particles and Cu foil is generated. Lowering the particle size of the active material down to sub-micron range results in highly improved contacts between both the active material and inactive materials like binder and conductive additives with the structured

collector foil. Due to this improved contact, higher adhesion forces and a significantly reduced internal resistance should be reached.

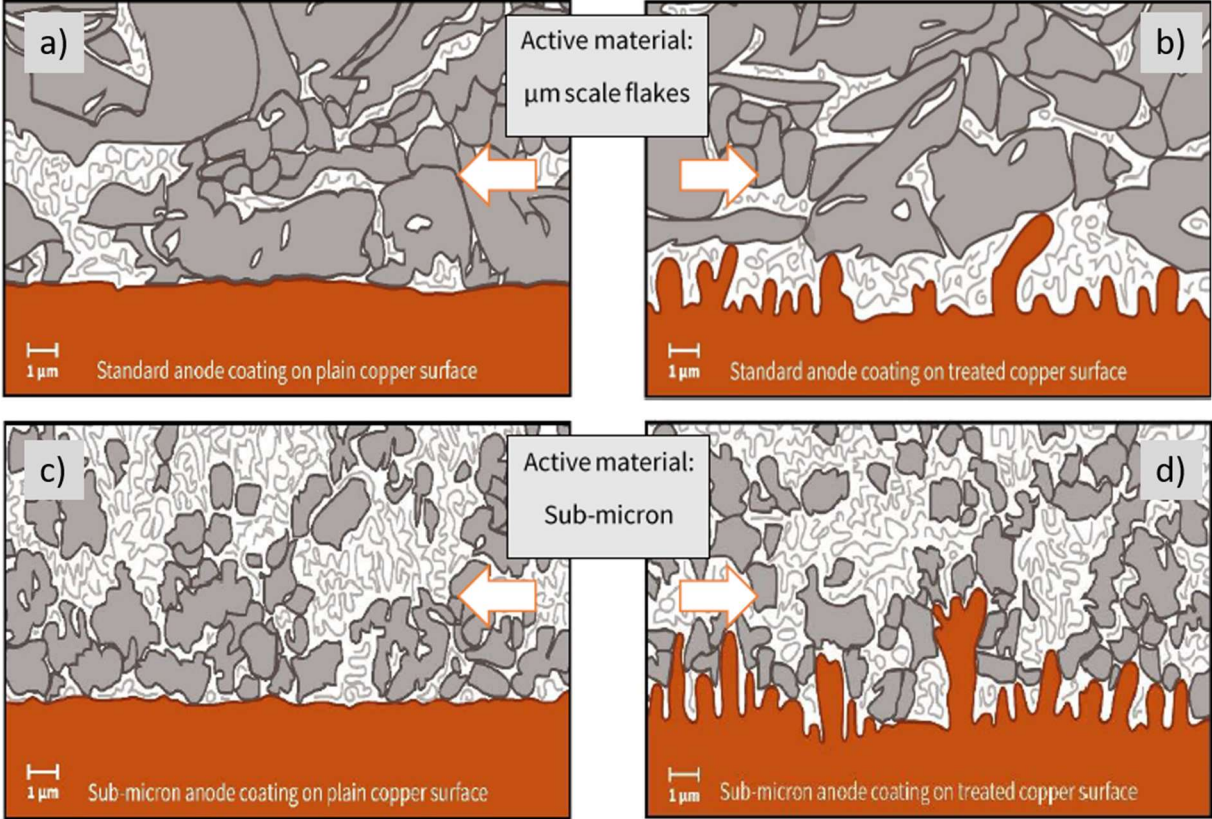


Figure 53: Scheme on connectivity of particles at different sizes; micrometer-scale flakes on plain (a) and treated (b) copper surface and sub-micron particles on plain (c) and treated (d) copper surface. Reprinted from ref. [29] under the terms of the Creative Commons CC-BY license.

BET measurement of dendritic copper foil resulted in a surface area of  $0.03 \text{ m}^2 \text{ g}^{-1}$ . The calculation of RF with equations 2-1 to 2-3 ended up with the fact that the dendritic copper foil owns an 8-fold larger surface compared to the untreated foil (assumption: RF of 1 in the case of uniformity).

Figure 54 a compares the different failure mechanisms – adhesive breaking at the interphase between active material and current collector and cohesive breaking within the active material – for untreated and dendritic current collector. It can be clearly seen that the degree of adhesive breaking is shifted to higher values for the dendritic current collector, meaning that a higher amount of adhesive breaking is taking place when using the dendritic one. Obviously, there is a disproportion between the particle size of the used LTO and the

morphological structure of the dendritic current collector. Due to a lack of formation of a planar connection between the LTO particle and the current collector, the weakest point of the bonding joint is thus located at the edge between the coating and the Cu collector, which further leads to a higher percentage of adhesive failure for the dendritic current collector compared to the untreated situation. A possible solution to this problem would be to use the electrochemical benefit of the dendritic current collector by preparing a coating with even smaller LTO particles in order to enhance the interlocking of the LTO in the pores of the Cu foil. With a smaller LTO particle size, the stresses applied to the electrode can be more widely distributed at the interface between the electrode material and the current collector. This would enable more plastic energy dissipation to occur and lead to an increase in adhesion strength thus decreasing the percentage of adhesive failure. In order to exploit the real benefit of the surface foil preparation the size ratio between substrate pores and active material particle size should be considered.

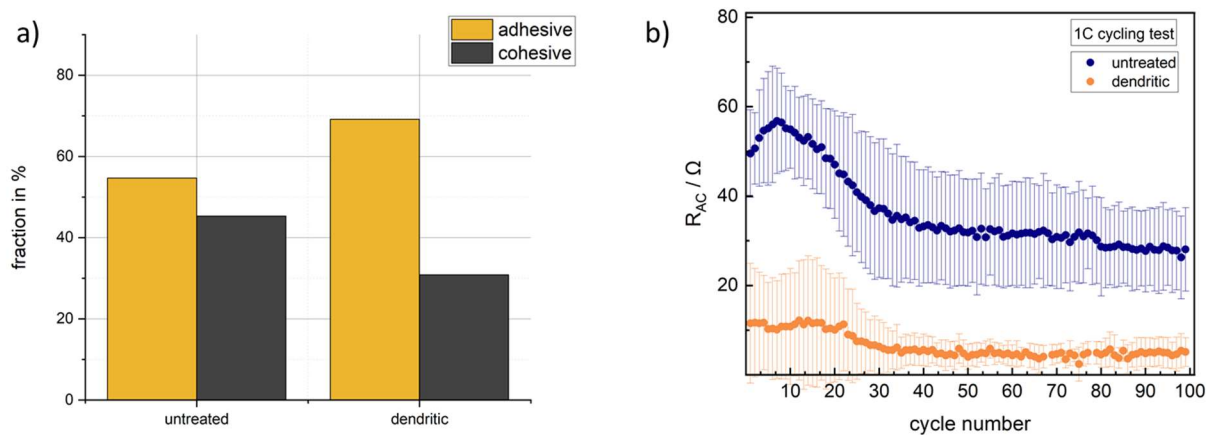


Figure 54: Comparison of failure mechanisms a) and internal resistance b) of LTO electrodes for untreated and dendritic copper foil as current collector. Reprinted from ref. [29] under the terms of the Creative Commons CC-BY license.

Figure 54b shows the internal resistance  $R_{AC}$  which is measured in-operando during cycling. This value is considerably reduced by a factor of 4.5 if comparing the LTO electrodes behavior with untreated (blue) and galvanically structured (orange) copper foil. Although not as precise as EIS measurements, these values already indicate an enhanced interface of the dendritic copper foil in contrast to the untreated one. Furthermore, C-rate capability is clearly improved, which can be seen in Figure 55, whereas an enlarged surface does not seem to show a significant difference for the ageing of electrodes during cycling test at 1C rate. A remarkable difference arises at application of highest C-rates above 5C. This corresponds to

the original target, namely to improve electrode transfer by increasing the interfacial area of LTO and copper foil.

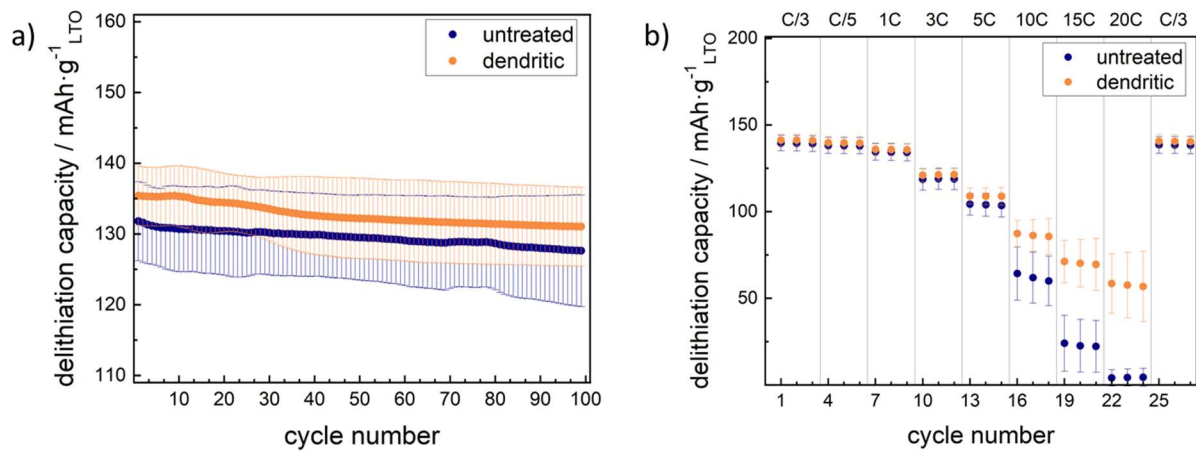


Figure 55: Galvanostatic charge/discharge test a) and C-rate test b) of LTO electrodes with untreated and dendritic current collectors. The error bars are also displayed. Reprinted from ref. [29] under the terms of the Creative Commons CC-BY license.

#### 4.3 Electrochemical impedance study

T-cells consisting of a LTO WE, Li CE and Li RE were investigated in three-electrode-mode via EIS comparing their behavior if untreated or dendritic copper current collectors were used along different states of charge. The EIS spectra were collected after three formation cycles (C/3 rate). Figure 56 shows the respective impedance spectra.

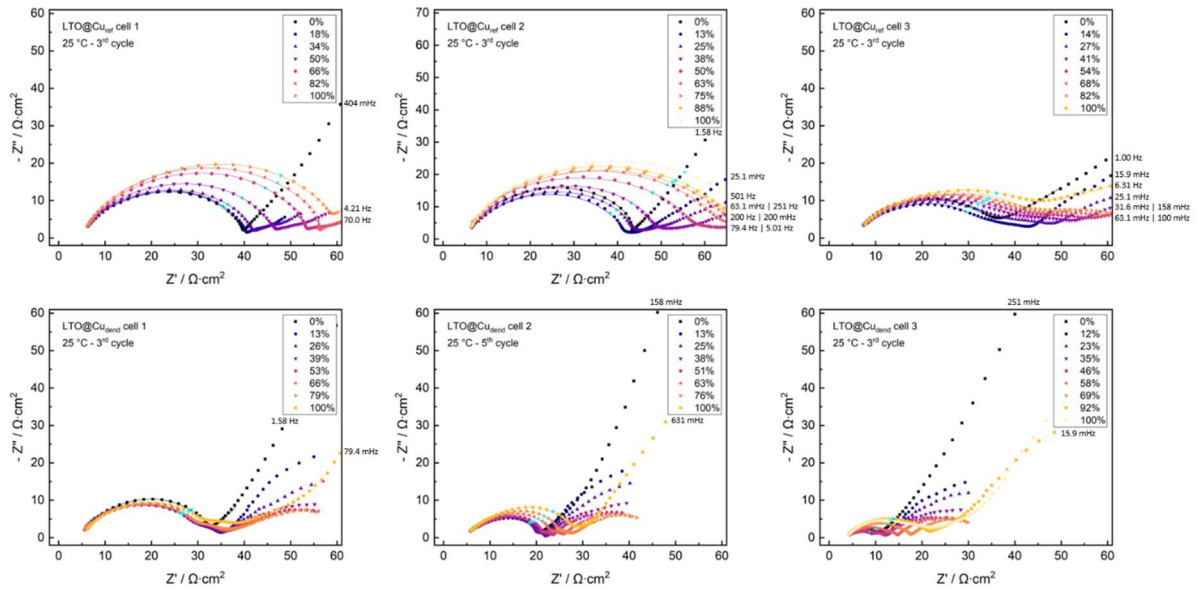


Figure 56: Impedance measurements (100 kHz – 10 mHz) of LTO electrodes on untreated or dendritic current collectors; three-electrode (T-cell) geometry; fitting curves indicated as solid lines; the data points at 1 kHz highlighted in pale blue; frequencies of final datapoints indicated for partially visible datasets. Reprinted from ref. [29] under the terms of the Creative Commons CC-BY license.

The Nyquist plots show a distorted flat semicircle and the Warburg behavior at the lowest frequencies. For data analysis, the equivalent circuit model shown in Figure 57 was used.

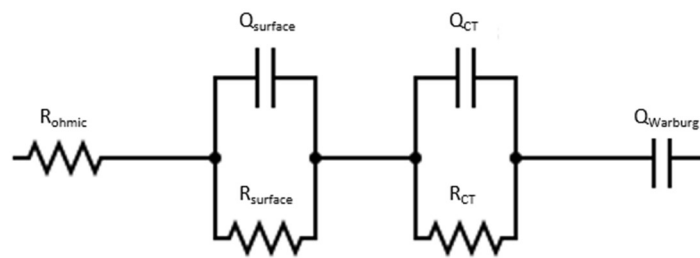


Figure 57: Equivalent circuit model used for EIS fit analysis.

The equivalent circuit model shown in Figure 57 was used for data analysis of the spectra in which two flat semicircles and a Warburg element is considered [195,196]. At the highest frequencies, ohmic resistance arises both from electrolyte and environment setup. Surface resistance phenomena are represented by the first semicircle, while the second semicircle arises from the LTO charge transfer reaction. LTO is usually considered to form negligible passivation layers [105,197,198] due to its relatively high potential, therefore main influence on the surface resistance should come from the electrode current collector interface [199].

Solid state diffusion phenomena are responsible for low frequency response [200]. While the resistance contribution due to SEI layer remains constant and independent from the SOC, the contribution related to the charge transfer increase with SOC. For some other active materials like NMC and graphite a similar SOC-dependency was already found; the charge-transfer signal of graphite [201] and NMC [202] decreases with increasing SOC. Due to the fact that the charge-transfer signal represents an intrinsic material parameter, a comparison between different materials might be questionable. Other groups have evaluated quite similar fitting parameters and a likewise impedance signal for LTO-based electrodes [41,203].

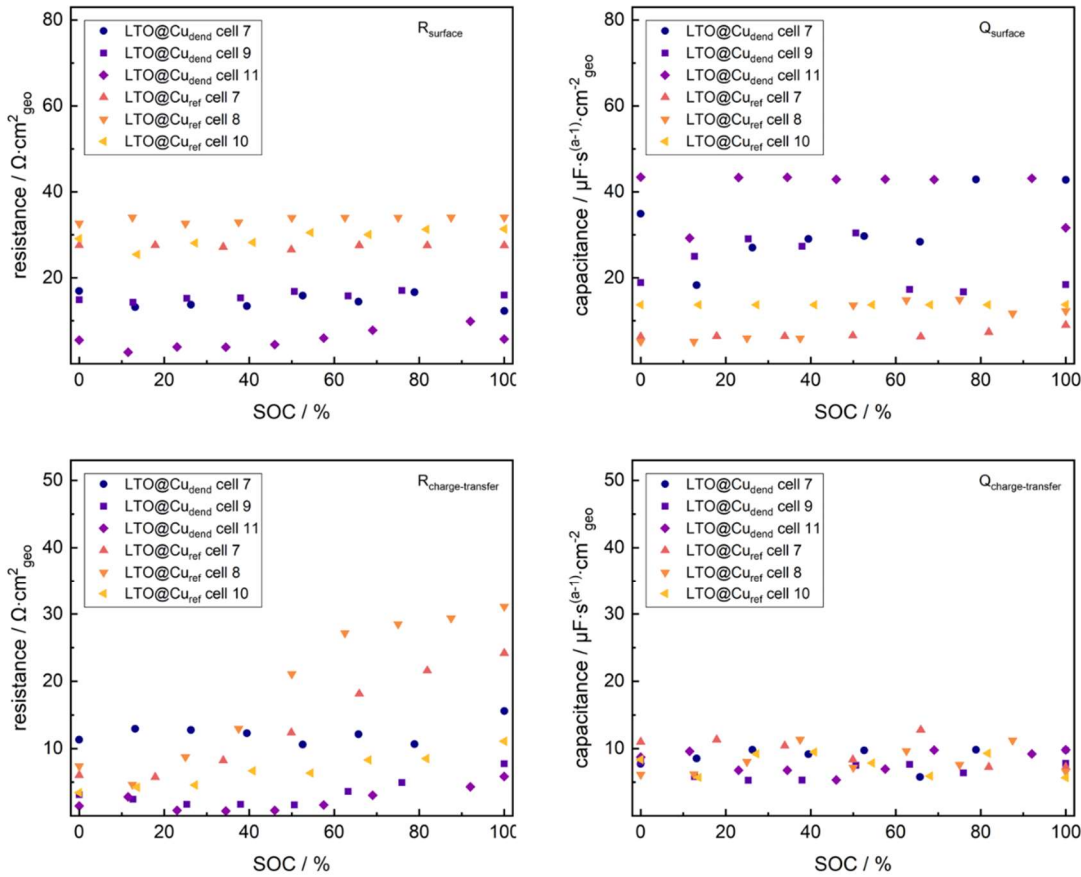


Figure 58: EIS fitting parameters of LTO electrodes with untreated or dendritic current collectors, along 3rd cycle lithiation step; data normalized to geometric electrode area. Reprinted from ref. [29] under the terms of the Creative Commons CC-BY license.

In Figure 56 the data point at 1 kHz (cyan highlighted) is close to the end of the semicircle in all the plots and its relative position seems not be affected by SOC for any of the cells. First, this behavior clearly excludes any changes in the system time constant throughout the measurements and secondly,  $R_{\text{surface}}$  originating the first semicircle can be regarded as

independent from SOC. Figure 58 shows the results from the data fitting in which the Warburg behavior was excluded.

The values of  $Q_{CT}$ , i.e. the double layer capacitance in parallel with the charge transfer resistance, lie around  $10 - 30 \mu\text{F}\cdot\text{s}^{(a-1)}\cdot\text{cm}^{-2}_{\text{geo}}$  for all cells with negligible dependence on SOC.  $Q_{\text{surface}}$  values show no significant correlation to the SOC and lie around  $6 - 13 \mu\text{F}\cdot\text{s}^{(a-1)}\cdot\text{cm}^{-2}_{\text{geo}}$  for cells coated on untreated copper current collector, while LTO electrodes coated on dendritic current collector reveal significantly increased capacitance fit parameters around  $17 - 43 \mu\text{F}\cdot\text{s}^{(a-1)}\cdot\text{cm}^{-2}_{\text{geo}}$ . Similarly, the surface resistance fit parameters have no significant correlation to SOC for any cell, though the introduction of a dendritic current collector in LTO electrodes significantly lowers the surface resistance fit parameters from  $27 - 34 \Omega\cdot\text{cm}^2_{\text{geo}}$  to  $4 - 15 \Omega\cdot\text{cm}^2_{\text{geo}}$ .

Differently than surface resistance, the LTO charge-transfer resistances increase linearly with SOC for all cells. Both phenomena do not indicate any dependence on the copper current collector geometry. It is more likely for the charge-transfer resistance to depend on the used electrolyte, as discussed by De Giorgio et al. [41]. Ma et al. showed comparable impedance parameters for a comparable electrolyte, but a different dependency on SOC [203], probably due to the different particle size. Kawade et al. though focusing on connection resistance of nanoparticles, reported in a similar order of magnitude for charge-transfer resistance [204]. Our fit parameters are also supported by several further publications with charge-transfer resistance values in likewise dimensions [199,201,205].

The decrease of the surface fit parameter of the electrode with dendritic current collector indicates a normalization discrepancy. While all fit parameters were normalized to the geometric electrode area, all surface resistance signals should truly depend on the electrochemically active interface area  $A_{\text{true}}$ . So obviously, the fitting parameters can be used as a measure for the electrochemically active interface area between LTO and copper foil. Further evaluation requires a statistical analysis of the respective fit parameters, which is shown in Figure 59.

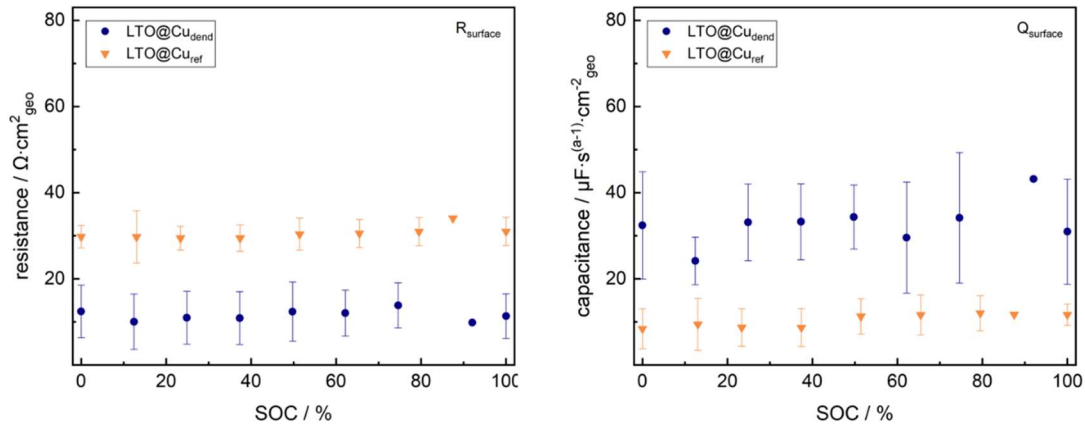


Figure 59: Averaged EIS fitting parameters of LTO electrodes with untreated or dendritic current collectors, along 3rd cycle lithiation step; data normalized to geometric electrode area. The point near 90% is the result of a single measurement. Reprinted from ref. [29] under the terms of the Creative Commons CC-BY license.

Table 14: Averaged EIS fit parameters of LTO electrodes.

Material	Surface capacitance [ $\mu\text{F}\cdot\text{s}^{(a-1)}\cdot\text{cm}^{-2}_{\text{geo}}$ ]	Surface resistance [ $\Omega\cdot\text{cm}^2_{\text{geo}}$ ]
LTO@Cu <sub>dendritic</sub>	25 ± 7	15 ± 6
LTO@Cu <sub>reference</sub>	8 ± 3	39 ± 4

The analysis of the generated EIS fit parameters provides two independent signal shifts, one for  $R_{\text{surface}}$  and one for  $Q_{\text{surface}}$ , bound to the difference in true electrochemically active interface. The normalization shift factor  $f_{\text{normalization}}$  results from the ratio between  $A_{\text{active-dendritic}}$  and  $A_{\text{active-reference}}$ , where  $A_{\text{active-dendritic}}$  and  $A_{\text{active-reference}}$  are the fit values at each SOC of  $R_{\text{surface}}$  and  $Q_{\text{surface}}$  reported in Figure 60.

$$f_{\text{normalization shift}} [A_{\text{active}}] = \frac{A_{\text{active-dendrit}}}{A_{\text{active-refere}}} \quad \text{Equation 4-1}$$

This normalization shift factor  $f_{\text{normalization shift}}$  for electrochemically active interface area is also capable to compare the physical surface areas of dendritic and untreated copper foil by indicating the RF.

$$f_{\text{normalization shift}} [A_{\text{true}}] = \frac{A_{\text{true-dendritic}}}{A_{\text{true-reference}}} = \frac{RF_{\text{dendritic}}}{RF_{\text{reference}}} \quad \text{Equation 4-2}$$

So finally,  $f_{\text{normalization shift}}$  allows for a direct comparison of electrochemically active interface area shift and physical surface increase, between dendritic and reference copper foil. This is visualized in Figure 60.

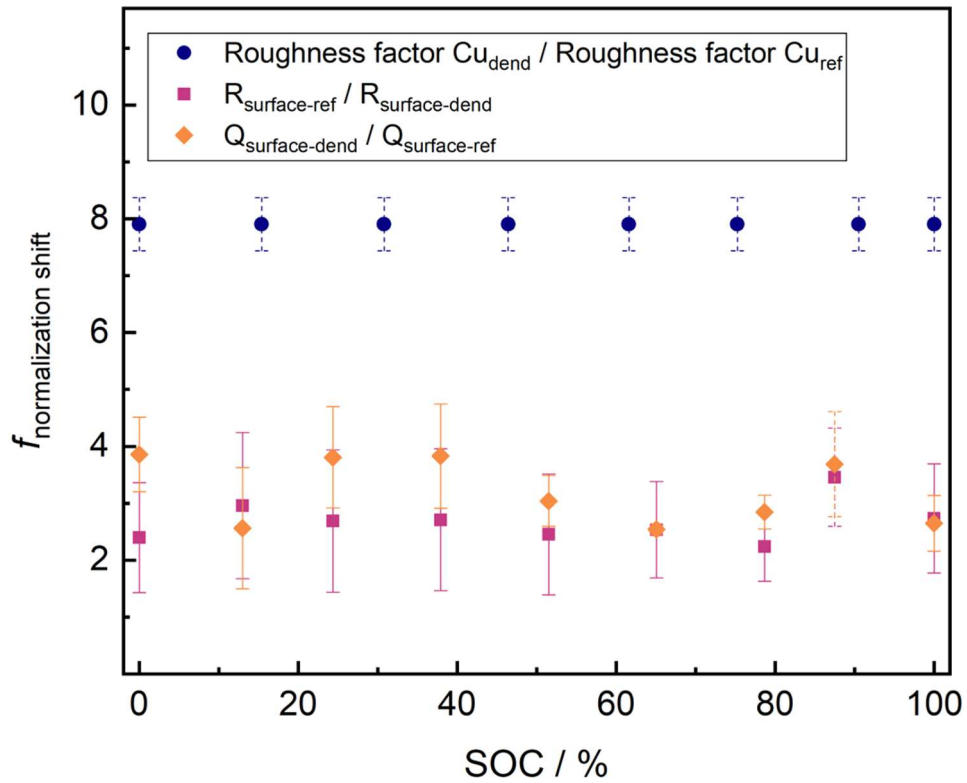


Figure 60: Comparison of surface increase factors at the electrode current collector interface, determined via roughness factor shift, surface capacitance shift and surface resistance shift; measured error bars indicated as solid lines, estimated error bars indicated as dashed lines. Reprinted from ref. [29] under the terms of the Creative Commons CC-BY license.

While the physical surface increase in interface area, given by the RF shift, lies at  $\approx 7.9$ , an electrochemically active shift of  $\approx 3.8$  or  $\approx 3.3$  is found for the surface capacitance shift and surface resistance shift, respectively. Consequently, 32 – 45 % of the increased surface area of the dendritic current collector are electrochemically active in the designed system.

#### 4.4 Conclusion

LTO anodes for the use in lithium-ion batteries on dendritic copper current collectors were successfully prepared. Evaluation of the surface modification was performed via mechanical analysis, FIB-SEM and electrochemical measurements. The investigations verified the existence of distinct copper dendrites leading to a physically increased surface area of the current collector. Differences in terms of inner resistance, rate capability at high current and surface resistance confirmed a clear difference in active area between untreated and dendritic current collectors due to the modified surface. Furthermore, a higher capacitance and a lowered surface resistance were found for the electrodes with the dendritic current collector in contrast to the ones with the copper reference. This indicates an improved connection between the current collector and the anode material, thus also proving an increase in electrochemically active surface area. Based on these findings, further research will be carried out to gain new insights into structural improvements for an enhanced performance of LTO anodes.

## 5 Preparation of Sodium Ion Battery

In recent times, LIBs are subjected to various discussions concerning safety, (environmental) sustainability and many others. On both active materials and the so-called “inactive” materials like separator, conductive agents, binders and many more intensive research is carried out in order to optimize them for different applications. Within the course of a massively growing market, especially in the field of electromobility, it is assumed that a higher price pressure occurs due to the problematic availability of lithium. Several other promising technologies reaching from redox flow systems to fuel cells as well as various chemical and electrical energy storage systems are currently being researched.

Sodium Ion Battery (SIB) technology is a suitable choice in terms of battery cost, safety and raw materials abundance [194]. The replacement of lithium by sodium in a battery seems straightforward at first sight, but unpredictable surprises are often found in practice [124]. Unfortunately, it is impossible to replace lithium by sodium without carrying out further adaptations like an adjustment of cell voltage, charging and discharging currents and the whole mechanical set-up. However, the basic set-up of a SIB is comparable to that of a LIB, containing Li or Na ions which are shuttling between the positive and negative electrode; these electrodes are separated by a porous membrane and filled up with electrolyte. Several differences in terms of size, polarity and accompanying properties like phase behavior and diffusion properties [124] make it essential to adapt both material choice and composition. Due to its bigger size, a customization of anode and cathode materials needs to be performed to ensure that the large sodium ion can easily accommodate within the host structure. Furthermore, the Na ions are subject to high diffusion barriers based on its large size [206]. Therefore, diffusion pathways need to be evaluated and adapted to Na ion technology.

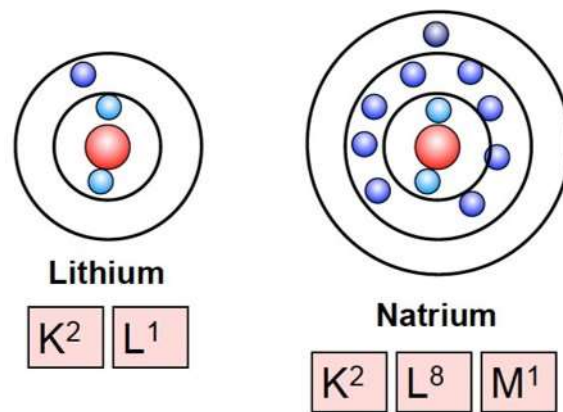


Figure 61: Size and electron configuration of lithium and sodium atom. Reprinted from ref. [207] under the terms of the Creative Commons CC-BY license.

Within the last years, many research groups on the one hand, and companies on the other hand, have concentrated on the evaluation and commercialization of sodium ion battery systems. With regard to increasing lithium prices and an increased environmental awareness and combined with the fact that many experience for LIB production technology can easily be adopted for SIB technology, this is a fast-growing sector.

## 5.1 Evaluation of suitable anode and cathode materials

To be able to perform synthesis with available lab equipment, a literature study on possible anode and cathode materials for SIB was conducted. Concerning factors like availability, sustainability and toxicity of educts, the choice fell on NASICON-type metal phosphate sodium titanium phosphate,  $\text{NaTi}_2(\text{PO}_4)_3$ , NTP, which was already in 1988 reported as to be able to insert lithium or sodium ions [208]. This material is also a possible cathode material for polymer lithium batteries with a voltage 2.5-2.6 V and metal lithium or graphite as anode [209]. Commonly, cathode materials used for SIBs can be divided into three groups: layered oxide cathode materials, polyanionic and prussian blue analogue cathode materials [210]. Layered oxide cathode materials mostly contain at least one of the following Fe and Mn materials due to the fact that the  $\text{Fe}^{2+}/\text{Fe}^{3+}$ ,  $\text{Mn}^{2+}/\text{Mn}^{3+}$  and  $\text{Mn}^{3+}/\text{Mn}^{4+}$  redox couples are regarded as ideal redox couples for electrode design because of their multiple properties in different chemical surroundings [210]. Typically,  $\text{NaFeO}_2$ ,  $\text{Na}_x\text{MnO}_2$  or mixed oxides containing cobalt and nickel belong to this group and have been intensively studied within the last years.

### 5.1.1 Selection of and synthesis process for anode material

Several possible preparation routes were evaluated and three promising ones compared with each other. Those were as follows:

Route #1: Described by Zhang et al. [211] followed a solid state method with  $\text{Na}_2\text{CO}_3$ ,  $\text{TiO}_2$  and  $(\text{NH}_4)_2\text{HPO}_4$  as educts. After ball-milling in acetone and drying and sintering at  $500\text{ }^\circ\text{C}$  for 5 h in air, a final heat treatment at  $900\text{ }^\circ\text{C}$  was performed. For the carbon coating, the NTP was ball-milled with glucose and sintered at  $800\text{ }^\circ\text{C}$ .

Route #2 was described by Vujkovic et al. [212] who followed a gel-combustion procedure.  $\text{Ti}(\text{C}_4\text{H}_9\text{O})_4$  was hydrolyzed to obtain  $\text{TiO}(\text{OH})_2$ .  $\text{NaNO}_3$  and  $\text{NH}_4\text{H}_2\text{PO}_4$  were added and upon dissolution, glycine was added. The homogenized solution was dried and the precursor transferred into the oven. An autocombustion took place at  $200\text{ }^\circ\text{C}$  and was followed by heating steps under argon.

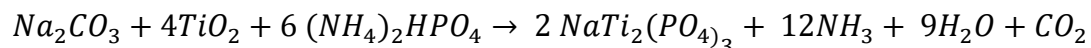
Route #3 was described by Delmas et al. [208], proposing a solid state method with  $\text{NaH}_2\text{PO}_4$ ,  $\text{TiO}_2$  and  $(\text{NH}_4)_2\text{HPO}_4$  as educts. This route was then adapted by Cao et al. [213].

Table 15 gives an overview on the eligible synthesis routes for NTP.

Table 15: Comparison of different synthesis routes for NTP.

	Route #1	Route #2	Route #3
Educts	$\text{Na}_2\text{CO}_3$ , $\text{TiO}_2$ , $(\text{NH}_4)_2\text{HPO}_4$	$\text{Ti}(\text{C}_4\text{H}_9\text{O})_4$ , $\text{NaNO}_3$ , $\text{NH}_4\text{H}_2\text{PO}_4$ , glycine	$\text{NaH}_2\text{PO}_4$ , $\text{TiO}_2$ , $(\text{NH}_4)_2\text{HPO}_4$
Mixing	Ball mill		Ball mill
Solvent	Acetone	Water, $\text{HNO}_3$	-
Sintering step	$500\text{ }^\circ\text{C}$ , 5 h in air, followed by $900\text{ }^\circ\text{C}$ , 24 h in air	$80\text{ }^\circ\text{C}$	-
Carbon coating	Glucose	Glycine	CB, graphite
Mixing	Ball mill		Ball mill
Sintering step	$800\text{ }^\circ\text{C}$ , 3 h in Argon	$200\text{ }^\circ\text{C}$ (0.5 h), $700\text{--}750\text{ }^\circ\text{C}$ (10 h)	$700\text{ }^\circ\text{C}$ , 2 h in Argon
Time	~ 36 h (4 h mixing, 32 h drying/sintering)	~ 16.5 h (6 h mixing, 10.5 h drying/sintering)	~ 5 h (3 h mixing, 2 h drying/sintering)

NTP was firstly synthesized according to route #1 where the following chemical reaction took place:



The educts  $\text{Na}_2\text{CO}_3$ ,  $\text{TiO}_2$  and  $(\text{NH}_4)_2\text{HPO}_4$  were weighted and mixing in a ball mill was performed with five wolfram carbide balls. As a solvent, 2.1 mL of acetone were added and the ball mill was started at a velocity of 350 rpm for two hours. After one hour, “sample 1” was extracted to perform XRD measurement and after the two hours of mixing process, one further “sample 2”.



Figure 62: Mixed educts in ball mill (left), sintered product “sample 4” (middle) and carbon-coated product (right).

In a next step, the sample is transferred into a sintering oven and sintered for 1.5 hours at 500 °C under ambient conditions. After this period, a “sample 3” is extracted to investigate the reaction progress via XRD. A further sintering step of 23 hours at 900 °C under ambient conditions is performed and “sample 4” is extracted. To complete the newly synthesized material with a carbon coating, 10.45 % of glucose are added and the mixing in 2 mL of deionized water in the ball mill is performed for one hour at 350 rpm. A last sintering step is then taking place for three hours at 800 °C under argon atmosphere, followed by slow cooling. The resulting product shows a different colour distribution depending on its location in the sintering oven, most probably dependent on an inhomogeneous temperature distribution within the oven. The product is divided in “sample 5a” (brown-white colour, maybe partly not coated with carbon) and “sample 5b” (black, most probably completely reacted to carbon-coated NTP). An overview of intermediate products is given in Figure 62.

Table 16: Used chemicals for synthesis route #1.

Educt	Molar ratio	Actual value [g]	Target value [g]zz
Na <sub>2</sub> CO <sub>3</sub>		0.796	0.795
TiO <sub>2</sub>		2.407	2.400
(NH <sub>4</sub> ) <sub>2</sub> HPO <sub>4</sub>		5.927	5.925

The corresponding XRD-measurements are depicted in Figure 63 and Figure 64 and clearly show the conversion of educts to carbon-composite NTP in the case of “sample 5b” in accordance with JCPDF card no. 33-1296. Furthermore, a thermal gravimetric analysis was performed.

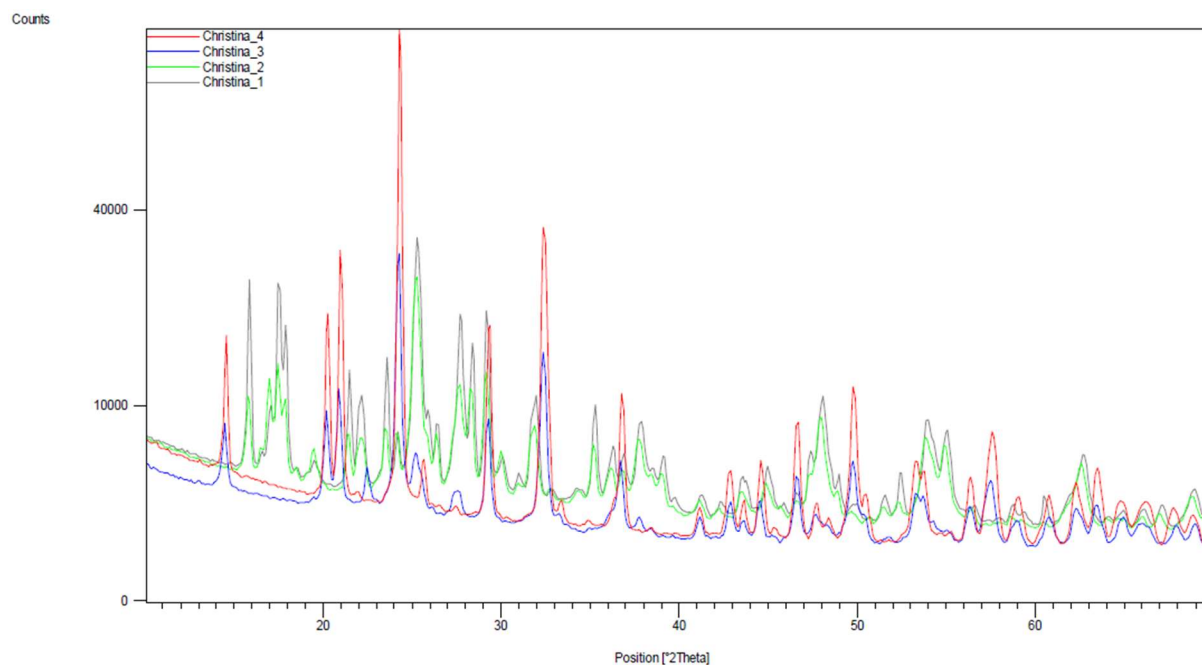


Figure 63: Result of XRD measurements for samples 1-4, synthesized by route #1.

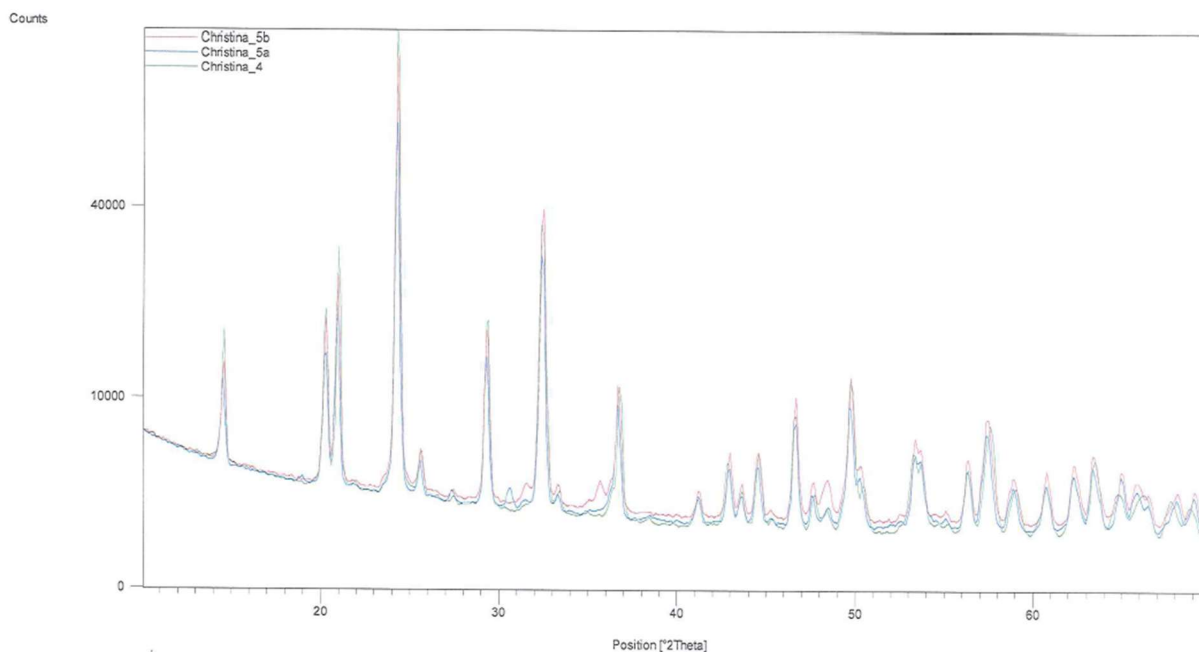


Figure 64: Result of XRD-measurement for samples 4-5, synthesized by route #1.

To estimate the amount of carbon-content on the synthesized NTP, a TGA measurement under ambient conditions was performed. An average weight loss of 1.55 % for the two samples 5b (up to 700 and 900 °C, respectively) was found leading to the result, that in fact, sample 5b owns a carbon coating, as confirmed in Figure 65. No carbon-content was detected for sample 5a, as the TGA weight percentage was decreasing with a constant slope not showing any specific weight decrease.

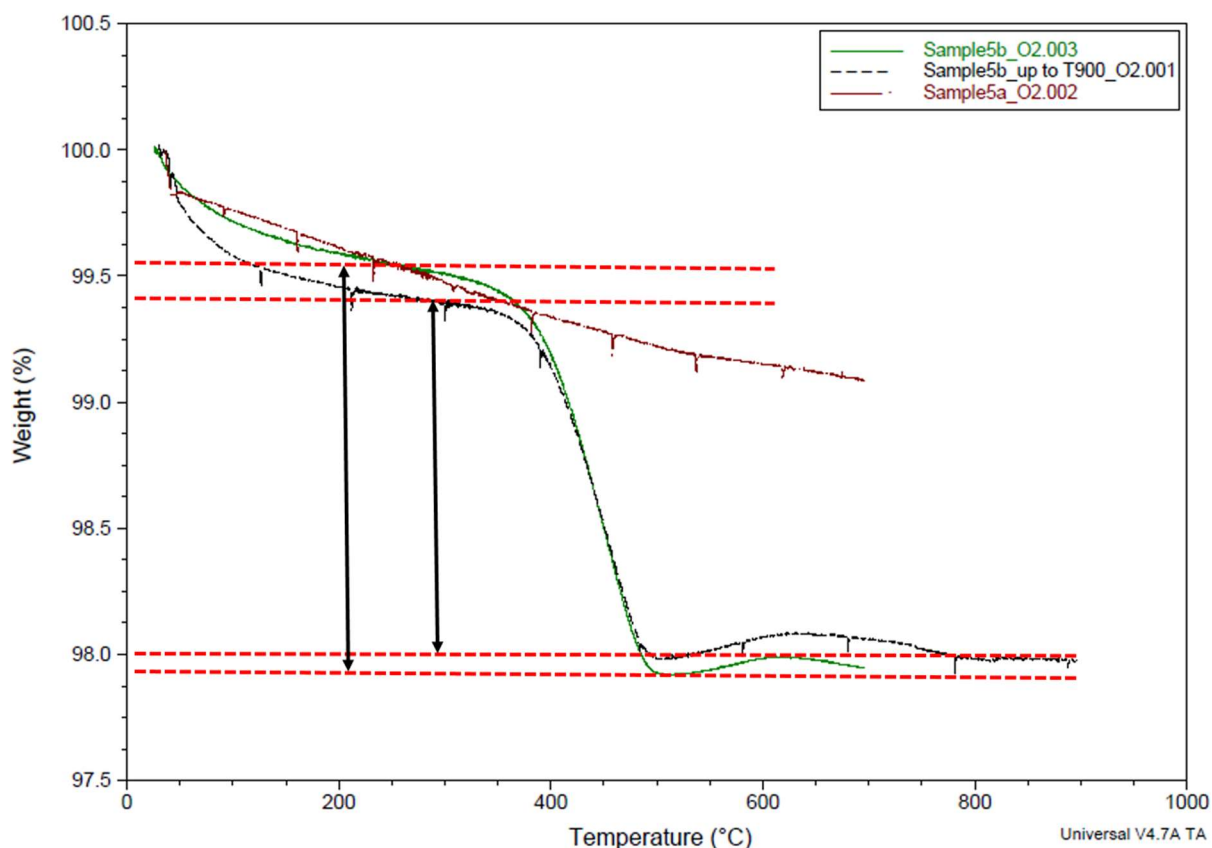
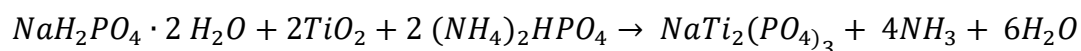


Figure 65: Result of TGA measurement of first NTP synthesis, synthesized by route #1.

By the abovementioned analysis techniques, it seems that synthesis route #1 is a practicable way to synthesize carbon-containing NTP in lab-scale.

As one further synthesis, route #3 was selected, mainly on the basis of its facile preparation with non-toxic and well available educts. The synthesis according to Cao et al. is based on the following reaction equation:



Initially, the educts with molar ratio and weight as described in Table 17 were placed in the ball mill and mixed for 10 minutes at 250 rpm using 10 tungsten carbide balls with a diameter of 10 mm. A small amount of the resulting white powder was extracted as "Sample 020919\_1" for XRD-measurements.

Table 17: Used chemicals for synthesis route #3.

Educt	Molar ratio	Actual value	Target value
NaH <sub>2</sub> PO <sub>4</sub>	1	3.128	3.120
TiO <sub>2</sub>	2	3.180	3.180
(NH <sub>4</sub> ) <sub>2</sub> HPO <sub>4</sub>	2	5.283	5.280

After the addition of 0.175 g (1.5%) CB and 0.29 g (2.5 %) of extruded graphite, the carbon coating was performed at 350 rpm for 60 minutes in the ball mill.



Figure 66: Product synthesis route #3 after ball-milling and carbon-coating.

The resulting intermediate product was exceptionally hard and virtually baked together with the milling medium, as can be seen in Figure 66. To retrieve the maximum possible amount of material, it was mechanically crushed and cleaned from the tungsten carbide balls. After a further grinding step to homogeneous powder, the sintering step at 700 °C for 2 hours under argon atmosphere was started. The fine powder product could easily be extracted from the sintering vessel and a sample “040919\_1” for XRD analysis was extracted and compared to the product of route #1, as can be seen in Figure 68. Though XRD for route #3 product shows a successful synthesis, the typical peaks for route #1 product are much more significant leading to the assumption that a lower amount of side reactions took place there. Some peaks of unreacted educts can also be found in the route #3 XRD analysis, most probably resulting in product impurities.

TGA analysis from Figure 67 resulted in a weight loss of more than 5 % starting at a temperature of around 550 °C. This corresponds to the degradation of the carbon content to

CO<sub>2</sub>, proving that the synthesis followed by the carbon coating step was successfully performed.

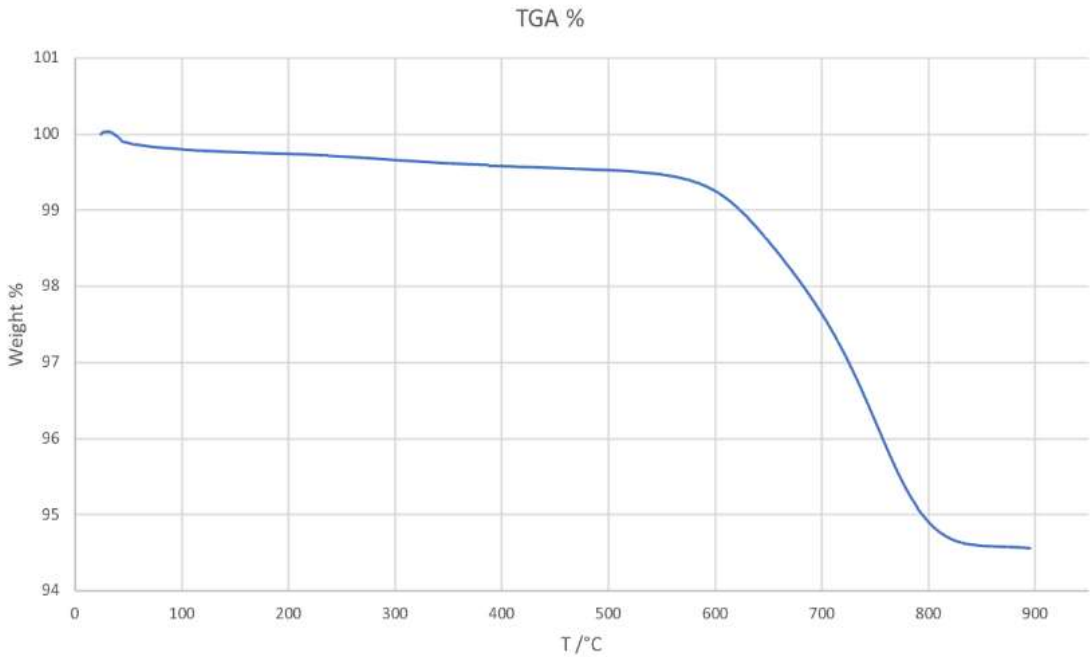


Figure 67: TGA analysis of prepared NTP according synthesis route #3.

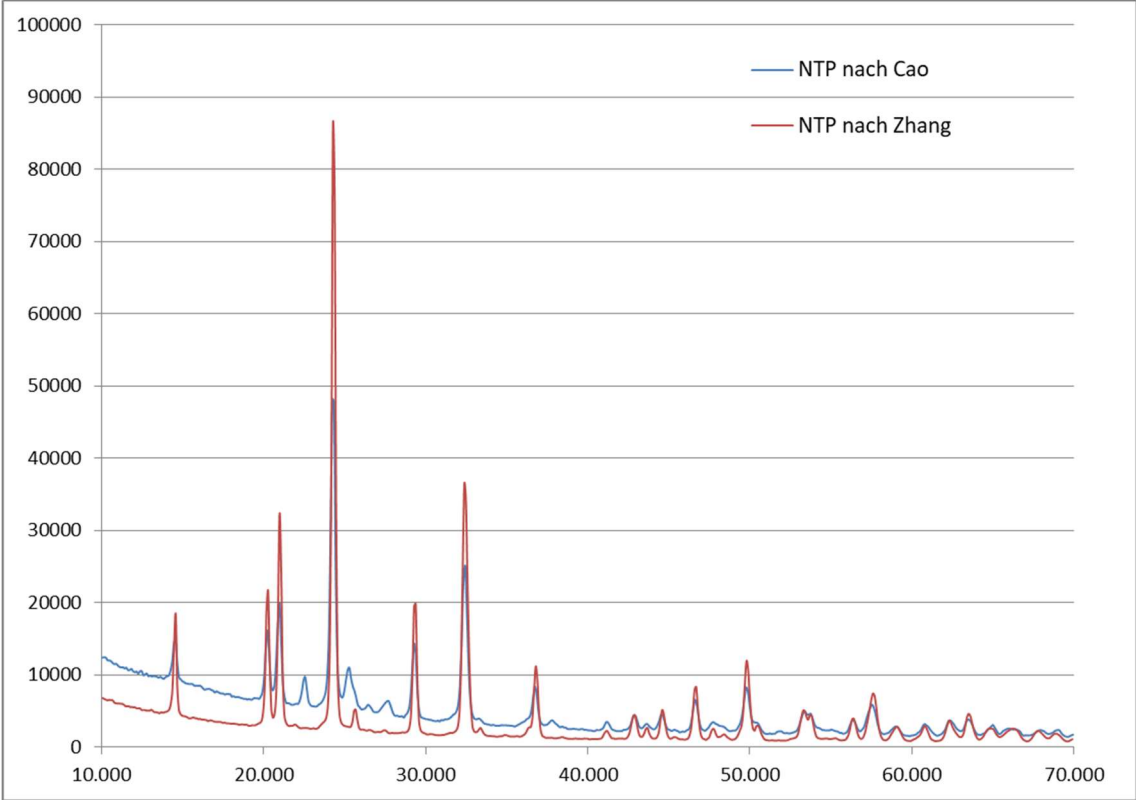


Figure 68: Comparison of products following synthesis route #1 and #3.

### 5.1.2 Synthesis process of cathode material

The preparation of lambda-MnO<sub>2</sub> was already described in 1981 by Hunter et al. by the treatment of LiMn<sub>2</sub>O<sub>4</sub> with aqueous acid [68]. 3.004 g of LiMn<sub>2</sub>O<sub>4</sub> were dissolved in 80 mL of deionized water under magnetic stirring. The pH monitoring was initiated before the first addition of diluted HCl acid and only after pH stabilization, the solution was stirred for 45 more minutes, as can be seen in Table 18.

Table 18: Step-wise addition of diluted HCl for preparation of lambda-MnO<sub>2</sub>

Addition diluted HCl	Time [min]	pH
-	0:00	9.25
2 mL	1:00	4.52
-	7:00	4.72
-	17:00	4.69
-	27:00	4.73
+ 4 more drops	32:00	Stable
+ 4 more drops	42:00	Stable
-	+ 45:00	stirring

As a next step, decanting and filtering through a sintered glass filter followed by washing with deionized water was performed. The sintered glass filter was then placed in a vacuum drying oven at 80 °C for 24 hours. The corresponding XRD spectrum is depicted in Figure 69 and reveals a spectrum that is slightly shifted to the left side when compared to reference spectrum according JCPDF-card # 33-1296. This is a strong indication for an incomplete conversion of the educt material LiMn<sub>2</sub>O<sub>4</sub>.

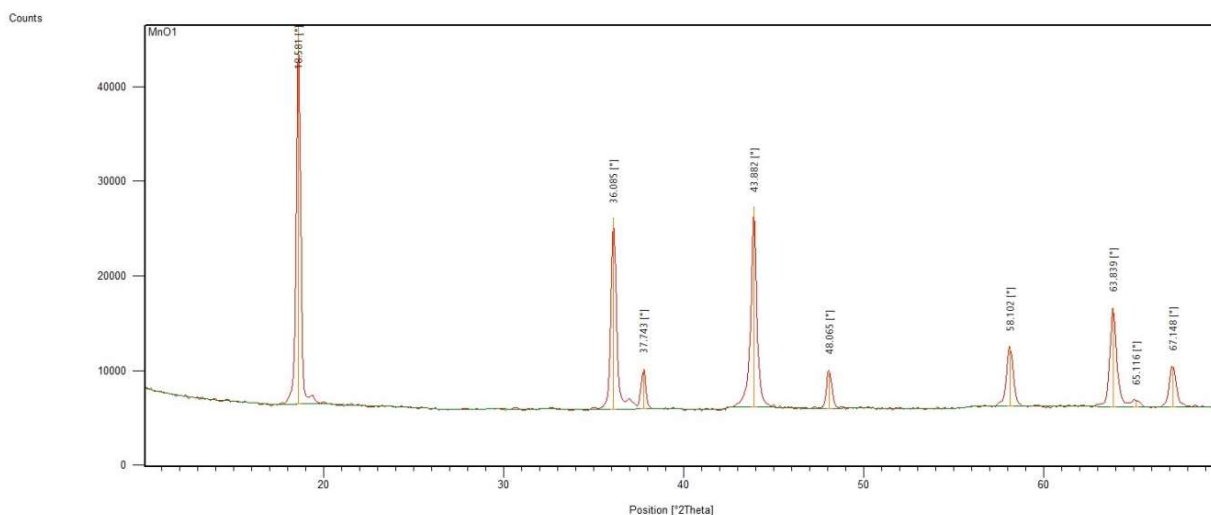


Figure 69: Result of XRD measurement for lambda-MnO<sub>2</sub> synthesis product.

SEM measurements in Figure 70 demonstrate fine, powdery and unregular shaped, flattened particles with a particle size in a range between 1 and 5  $\mu\text{m}$ .

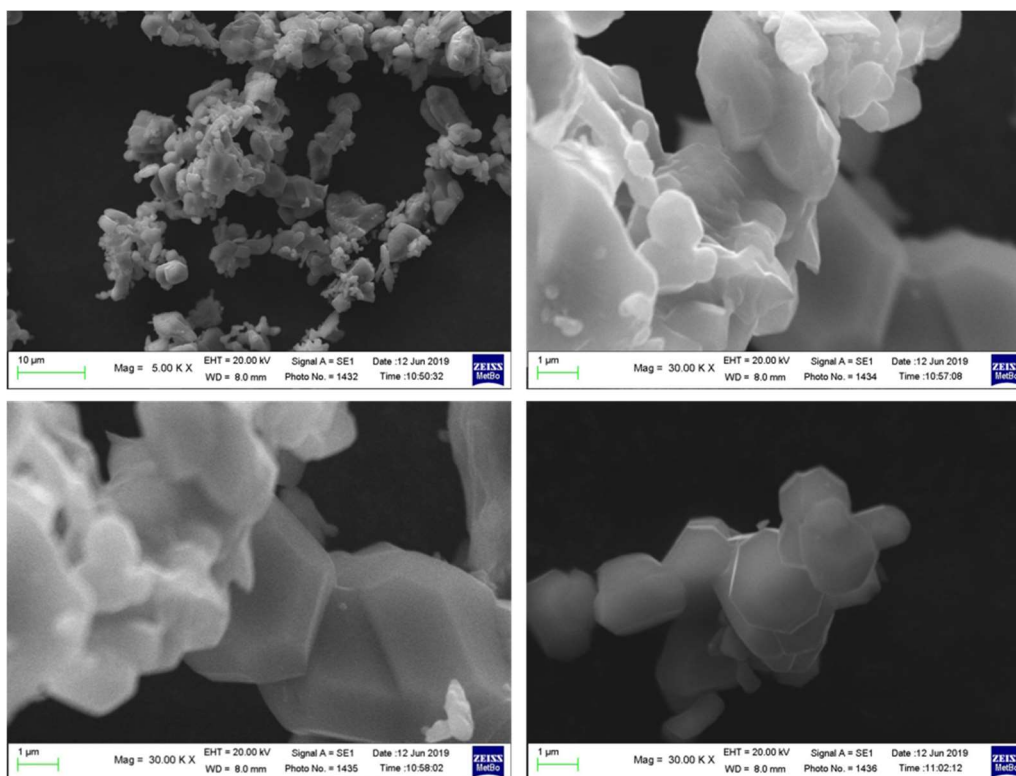


Figure 70: SEM images of synthesized lambda-MnO<sub>2</sub>.

To make sure that the questionable incomplete conversion of LiMn<sub>2</sub>O<sub>4</sub> did not originate from acidic treatment, another synthesis with sulfuric acid was conducted, following a route

proposed by Yuan et al. [214]. Therefore, 5.00 g of  $\text{LiMn}_2\text{O}_4$  were dissolved in 500 mL of 5.6 M  $\text{H}_2\text{SO}_4$  under magnetic stirring at a temperature of 50 °C. Stirring was conducted for 23 hours at this temperature and was followed by an ultrasonic cleaning step at room temperature for 3 hours. The solution was then separated, filtered through a glass sinter filter and washed several times with deionized water. Drying was performed at 100 °C in a vacuum drying chamber for 12 hours.

Analysis of powder diffraction ended up with the result, that several Li-enriched phases of  $\text{LiMn}_2\text{O}_4$  and  $\text{Li}_2\text{Mn}_2\text{O}_4$  (probably due to a reduction of  $\text{Mn}^{4+}$  by sulfuric acid at high temperatures) are still present in the product.

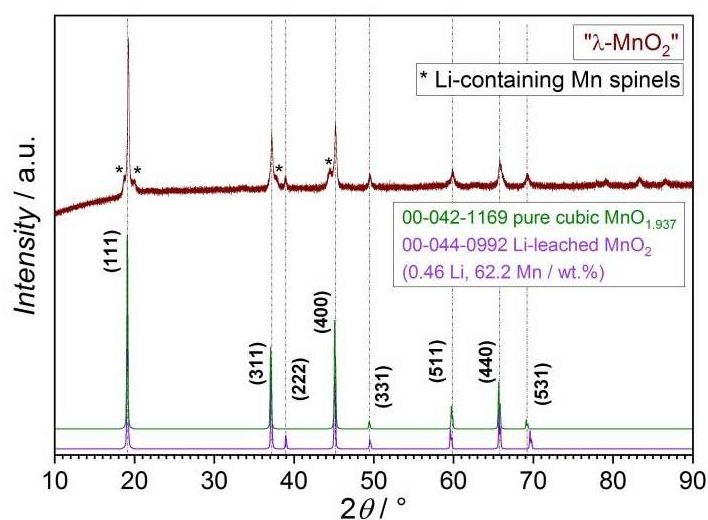


Figure 71: XRD analysis of  $\lambda\text{-MnO}_2$  prepared with sulfuric acid.

## 5.2 Preparation of electrodes

Preparation of NTP electrodes was performed using NMP as a solvent. The recipes frame parameters were adopted to the question whether a suitable electrode slurry in general can be prepared. Therefore, high amounts of conductive additive and binder were added in the ratio 70:20:10 (NTP:CB:PVDF). Due to the fact that only a small amount of NTP could be synthesized, the electrode paste was manually prepared in a mortar and coated upon a carbon-coated aluminium current collector foil at a wet thickness of 250  $\mu\text{m}$ .

As CE, a carbon electrode consisting of 83.9% of activated carbon, 4.6% conducting additive Super P, 4.8% of CMC-binder and 6.7% PTFE binder was used to assembly a Teflon® BOLA (Bolhander GmbH) three electrode cell.

Table 19: Active material weight and electrolyte volume for electrodes.

Cell-#	NTP Anode [mg]	Treatment	Graphite cathode [mg]	NaPF <sub>6</sub> in PC:FEC [μL]	LP30 [μL]
29	2,43	Pressure (5 tons)	12,09	600	100
34	2,74	Pressure (5 tons)	11,08	500	200
28	2,23		9,85	400	100
33	2,24	Carbon paper	9,71	600	100
10	2,32	Carbon paper	11,01	600	100
7	1,92	Pressure (5 tons)	11,05	500	200

For the evaluation of further influence factors, some electrodes were prepared and subjected to pressure and others were directly coated upon a carbon paper, as can be seen in Table 19. The use of the carbon paper was based on the assumption, that a highly structured, three-dimensional current collector surface – as already discussed in chapter 4 *Improved current collector surfaces for LTO electrodes* – is advantageous for electrochemical properties.

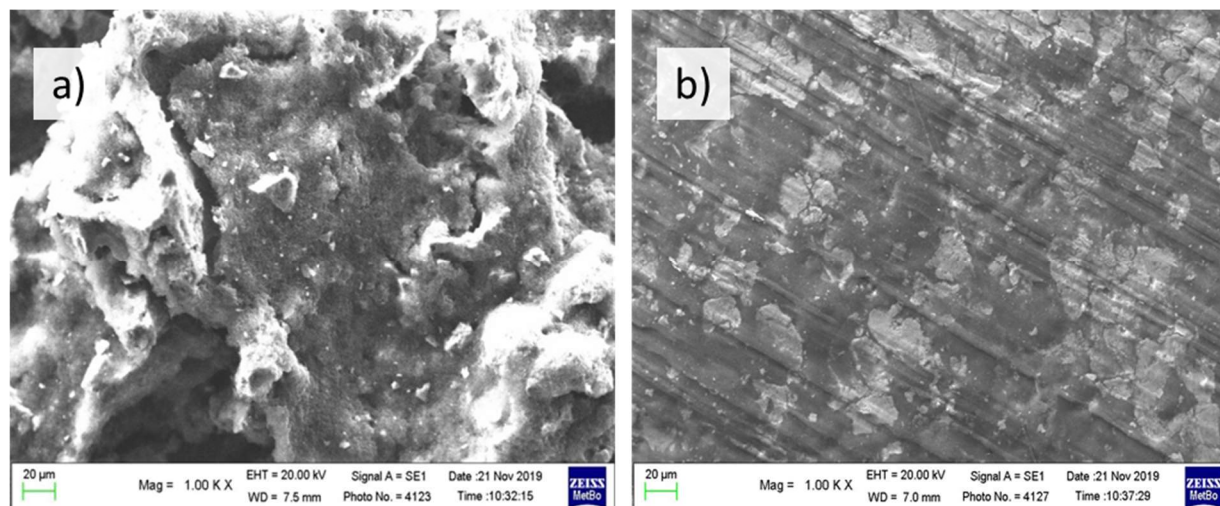


Figure 72: SEM images of unpressed (a) and pressed (b) NTP anode (reprinted with permission from ref [215]).

To morphologically evaluate the electrodes, SEM images have been taken from a pressed and an unpressed sample, as can be seen in Figure 72. The structure of the unpressed electrode is

containing several inhomogeneities and fine cracks, whereas the pressed one has a smooth and planar surface [215].

### 5.3 Cyclovoltammetric measurements

The unpressed electrode #28 has been subjected to cyclovoltammetry measurements at 0.1 and 0.2  $\text{mV s}^{-1}$ , leading to the graph depicted in Figure 73. An oxidation peak at about 2.35 V is clearly visible for both measurement speeds, indicating a kind of side reaction and rarely visible titanium reduction/oxidation. Obviously, the unpressed electrode is not capable of performing efficient titanium reactions. The potential is reported vs.  $\text{Li}^+/\text{Li}$  to underline the fact that Li metal was used as reference.

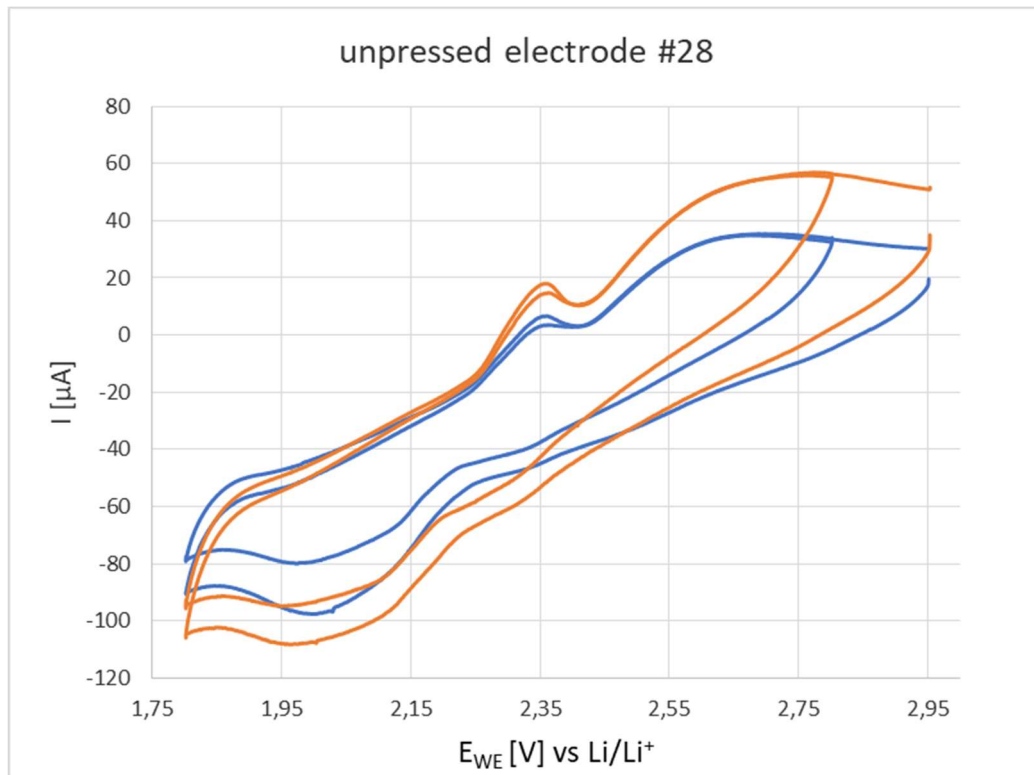


Figure 73: Cyclovoltammetry of unpressed electrode #28 at different scan speeds (0.1 mV/s in blue and 0.2 mV/s in orange), reprinted with permission from ref. [215].

Further CyV measurements of electrode #10 equipped with carbon paper showed a slightly shifted CyV diagram, as can be seen in Figure 74. Also in this case, a significant pair of peaks besides Ti-redox reaction was also visible in Figure 73. These additional peaks can be assigned

to any kind of parasitic process based on the interaction of the carbon paper with the chosen electrolyte system.

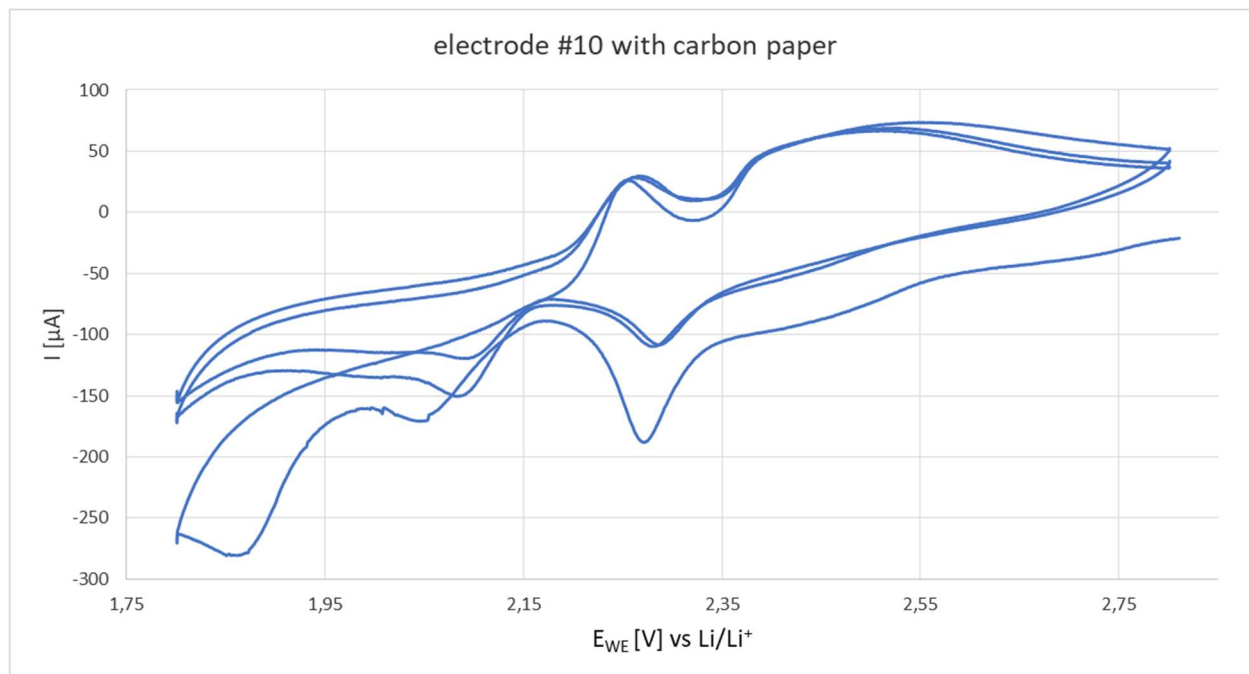


Figure 74: CyV diagram of electrode #10 equipped with carbon paper at 0.05 mV/s. Reprinted with permission from ref. [215].

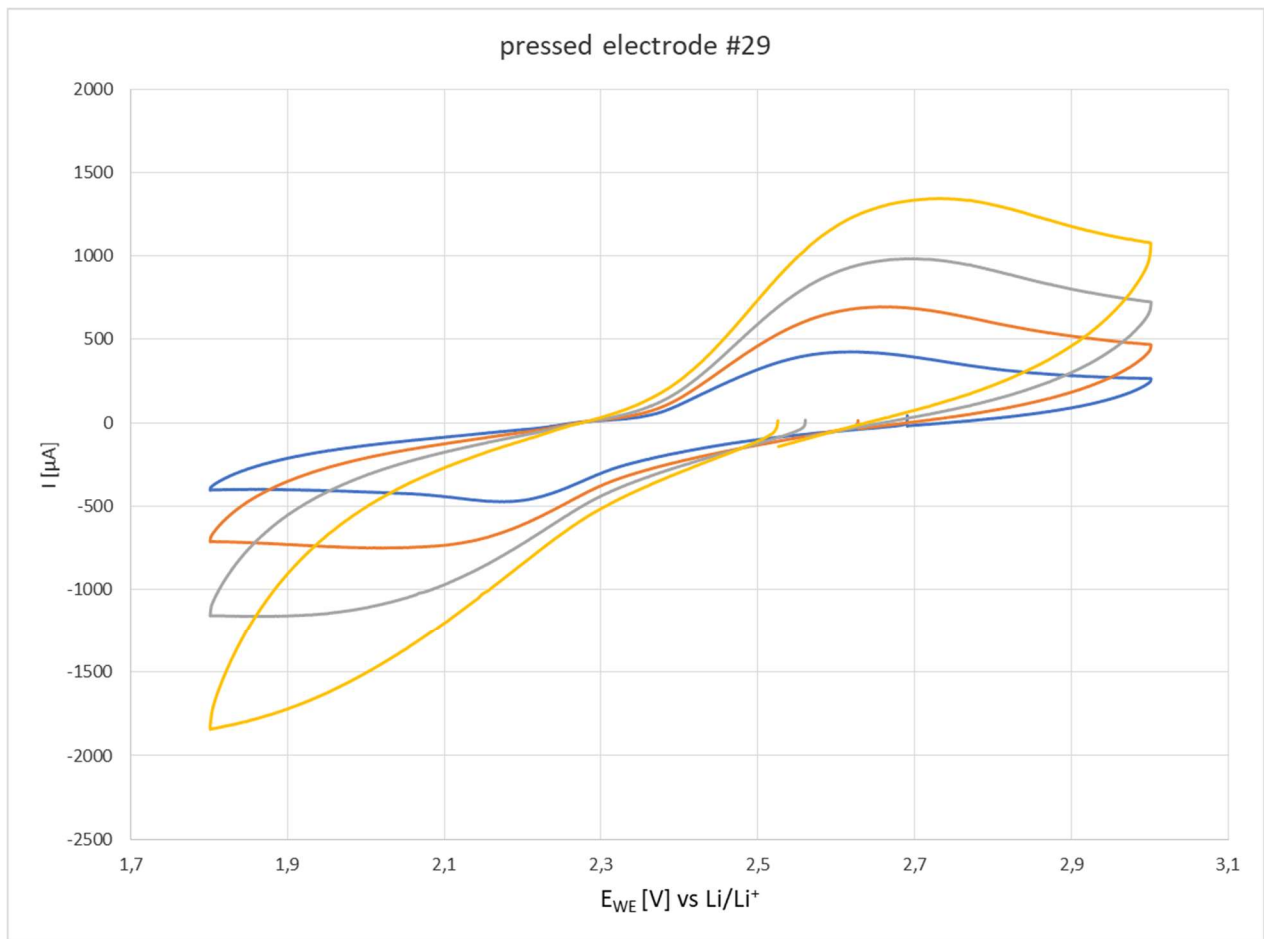


Figure 75: CyV diagram of pressed electrode #29 at different measurement speeds of 2 (blue), 5 (orange), 10 (grey) and 20 (yellow) mV/s. Reprinted with permission from ref. [215].

The measurement of pressed electrode revealed a very different picture, as can be seen in Figure 75. Obviously, pressing of the electrodes leads to a morphological improvement which can directly be seen in CyV measurements, and is therefore assumed as optimum choice for this kind of electrodes.

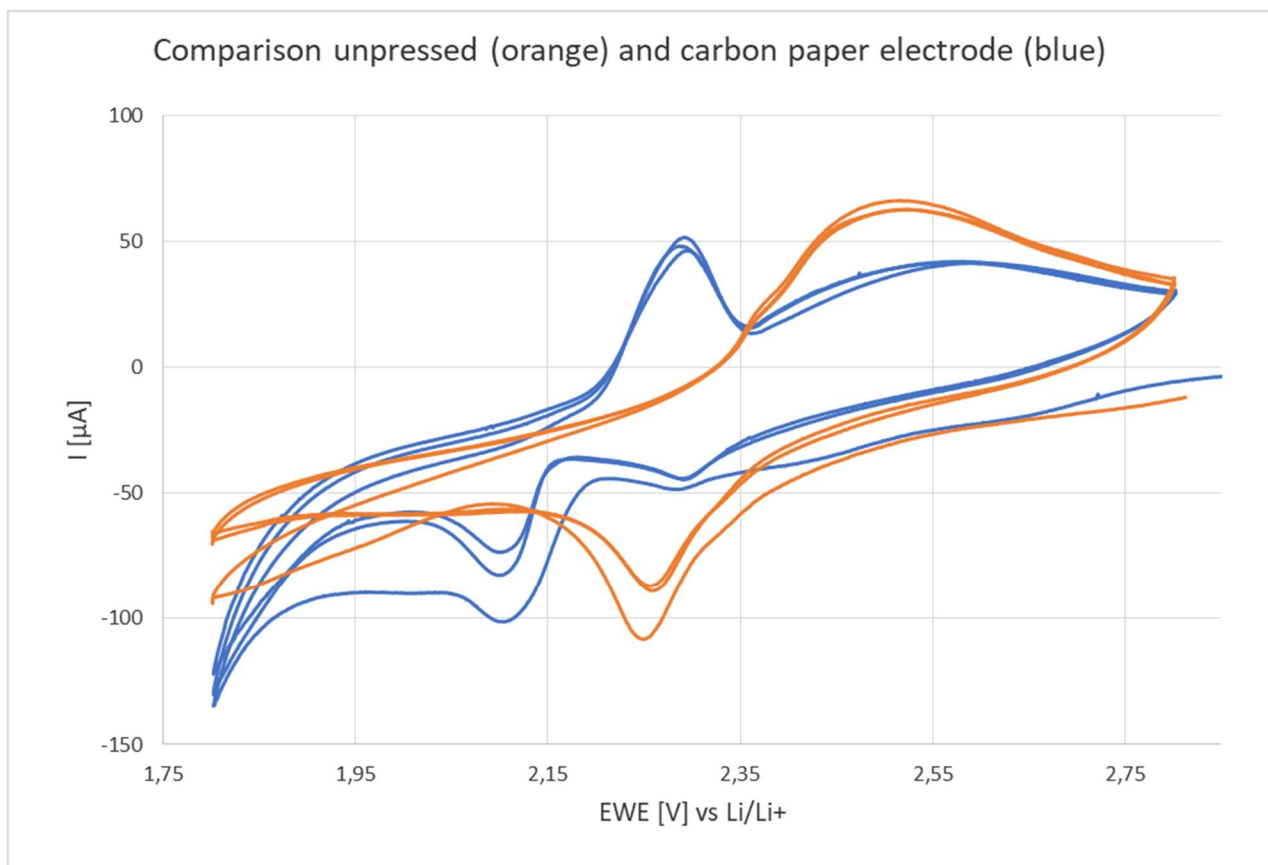


figure 76: Comparison between unpressed electrode (#7, orange) and carbon paper electrode (#33, blue) at 0.1 mV/S. Reprinted with permission from ref. [215].

Furthermore, a free standing NTP electrode (80 % NTP, 10 % CB, 10 % binder) has been prepared to be used in aqueous SIB. The binder was water-soluble chitosan. Given the idea to use this electrode in an aqueous cell, the chitosan was crosslinked in order to maintain the mechanical stability of the electrodes as described in reference [216]. The cyclic voltammetry in figure 77 has been carried out in a BOLA cell with Ag as reference electrode (potential reported vs SCE) and a counter electrode made of activated carbon that works in capacitive mode. The electrolyte was 1.5 M  $\text{Na}_2\text{SO}_4$  in water.

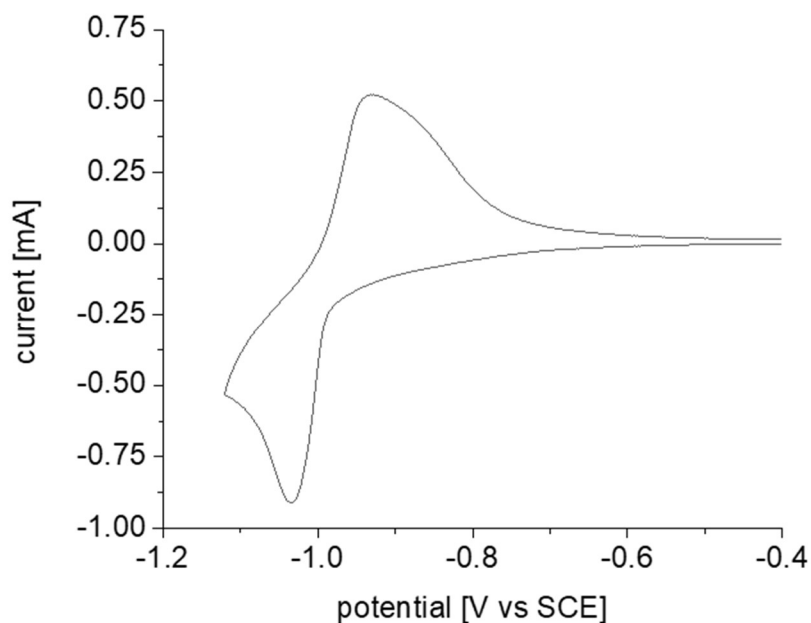


figure 77: CyV of NTP electrode ( $6 \text{ mg cm}^{-2}$ ) with chitosan binder in aqueous  $1.5 \text{ M Na}_2\text{SO}_4$ -solution at  $0.5 \text{ mV s}^{-1}$ .

This NTP anode displays a quasi-reversible process and can therefore be called a successful application of this type of anode material for aqueous SIB. Its potential is limited by water reaction, but is stable in aqueous medium. Further study are ongoing.

#### 5.4 Conclusion

The preparation of low-cost sodium ion battery anode and cathode materials was successfully performed. The  $\lambda$ - $\text{MnO}_2$  was synthesized from LMO and characterized in several morphological measurements. As the conversion did not seem to have been successfully performed, further evaluation of this material was not conducted.

The NTP was evaluated in terms of morphological and further electrochemical measurements via cyclic voltammetry. A clear improvement could be found for pressed electrodes in contrast to unpressed electrodes and those equipped with an additional carbon paper. This material seems to be a promising candidate for application in a low-cost SIB.



## 6 Conclusions

In this PhD work, several aspects concerning the sustainability and eco-friendliness of lithium and sodium ion batteries have been highlighted, starting from the raw materials up to improvements based on complex structuring of the current collector foil.

One main topic has been the preparation and evaluation of different water-based binder systems as an alternative to commonly used solvent-based ones, which are lacking from safety and sustainability. It was shown that a great variety of different bio-based binders with low environmental impact does not only exist, but also reveals nearly similar properties in an operating electrochemical cell when compared to standardly used and mostly fluoride-based binders. This can pave the way to a completely water-based battery processing on the one hand, which is beneficial in manifold ways: A decreased consumption of toxic solvent with all its disadvantages is definitely a big step towards sustainable battery production, and the same applies for a lower demand of fluorinated polymers. A replacement of those binders by bio-based polymers is a feasible way to reduce the ecological footprint of future batteries.

As a very promising binder candidate for the use in LTO anodes, SA was identified and further investigated. Its specific rheological properties guided to a study on its complex interactions in aqueous medium, once again emphasizing its good applicability as a binder polymer for battery electrodes.

A closer look on the optimization possibilities of composite electrode and copper current collector was performed, as the active material LTO suffers from a low electric conductivity and lithium ion diffusion coefficient. By the help of copper deposition upon current collector foil, distinct copper dendrites were formed on the surface and lead to an increased surface area, thus enhancing its mechanical stability. Furthermore, an increased electrochemically active surface was found out for this highly structured foil, proving its beneficial properties. Compared to untreated copper foil, it revealed a reduced internal resistance and an improved C-rate capability. Calculation of roughness factor lead to the conclusion, that it provides an 8-fold larger surface area compared to untreated foil.

SIBs basically obtain a higher degree of sustainability, as their raw material availability is not critical and a great variety of naturally based materials can be used. A SIB anode on the basis of NTP was prepared by different synthesis routes and combined with a cathode to evaluate

its electrochemical properties. It was found out that pressing of the composite electrode is not only favorable for its later electrochemical behavior, but also leads to an increased mechanical stability. NTP can also be a free-standing, suitable cathode for aqueous SIB and its processing by using a crosslinked, water-soluble binder is the demonstration that sustainability can be achieved through different ways.

To conclude, many possible ways lead to an improvement of sustainability for lithium and sodium ion batteries and the most promising ones are a critical evaluation of raw material consumption and the replacement of critical and/or toxic ingredients by bio-based and eco-friendly alternatives.

## 7 References

1. Mancini, L.; Eslava, N.A.; Traverso, M.; Mathieux, F. *Responsible and sustainable sourcing of batteries raw materials: Insights from hotspot analysis, corporate disclosures and field research*; Publications Office of the European Union: Luxembourg, 2020, ISBN 978-92-76-17950-4.
2. Zhang, W.; Zhang, F.; Ming, F.; Alshareef, H.N. Sodium-ion battery anodes: Status and future trends. *EnergyChem* **2019**, *1*, 100012, doi:10.1016/j.enchem.2019.100012.
3. L. Kulova, T. A Brief Review of Post-Lithium-Ion Batteries. *Int. J. Electrochem. Sci.* **2020**, 7242–7259, doi:10.20964/2020.08.22.
4. Birke, P.; Schiemann, M. *Akkumulatoren: Vergangeheit, Gegenwart und Zukunft elektrochemischer Energiespeicher*; Herbert Utz Verlag: München, 2013, ISBN 978-3-8316-0958-1.
5. Goriparti, S.; Miele, E.; Angelis, F. de; Di Fabrizio, E.; Proietti Zaccaria, R.; Capiglia, C. Review on recent progress of nanostructured anode materials for Li-ion batteries. *J. Power Sources* **2014**, *257*, 421–443, doi:10.1016/j.jpowsour.2013.11.103.
6. Goodenough, J.B.; Park, K.-S. The Li-ion rechargeable battery: a perspective. *J. Am. Chem. Soc.* **2013**, *135*, 1167–1176, doi:10.1021/ja3091438.
7. Hiremath, M.; Derendorf, K.; Vogt, T. Comparative life cycle assessment of battery storage systems for stationary applications. *Environ. Sci. Technol.* **2015**, *49*, 4825–4833, doi:10.1021/es504572q.
8. Cusenza, M.A.; Bobba, S.; Ardente, F.; Cellura, M.; Di Persio, F. Energy and environmental assessment of a traction lithium-ion battery pack for plug-in hybrid electric vehicles. *J. Clean. Prod.* **2019**, *215*, 634–649, doi:10.1016/j.jclepro.2019.01.056.
9. Wang, L.; Wu, H.; Hu, Y.; Yu, Y.; Huang, K. Environmental Sustainability Assessment of Typical Cathode Materials of Lithium-Ion Battery Based on Three LCA Approaches. *Processes* **2019**, *7*, 83, doi:10.3390/pr7020083.
10. Ellingsen, L.A.-W.; Hung, C.R.; Majeau-Bettez, G.; Singh, B.; Chen, Z.; Whittingham, M.S.; Strømman, A.H. Nanotechnology for environmentally sustainable electromobility. *Nat. Nanotechnol.* **2016**, *11*, 1039–1051, doi:10.1038/NNANO.2016.237.
11. Daniel, C.; Mohanty, D.; Li, J.; Wood, D.L. Cathode materials review. In . REVIEW ON ELECTROCHEMICAL STORAGE MATERIALS AND TECHNOLOGY: Proceedings of the 1st International Freiberg Conference on Electrochemical Storage Materials, Freiberg, Germany, 3–4 June 2013; AIP Publishing LLC, 2014; pp 26–43.
12. Manthiram, A. A reflection on lithium-ion battery cathode chemistry. *Nat. Commun.* **2020**, *11*, 1550, doi:10.1038/s41467-020-15355-0.
13. Morgan, D.; van der Ven, A.; Ceder, G. Li Conductivity in  $\text{Li}_{x}\text{MPO}_{4}$  (M = Mn, Fe, Co, Ni) Olivine Materials. *Electrochem. Solid-State Lett.* **2004**, *7*, A30, doi:10.1149/1.1633511.
14. Toigo, C. *Development of Lithium-Iron-Manganese-Phosphat-Cathodes: Bachelor Thesis*, 2016.
15. Hischer, R.; Kwon, N.H.; Brog, J.-P.; Fromm, K.M. Early-Stage Sustainability Evaluation of Nanoscale Cathode Materials for Lithium Ion Batteries. *ChemSusChem* **2018**, *11*, 2068–2076, doi:10.1002/cssc.201800109.
16. Chakraborty, A.; Kunnikuruvaan, S.; Kumar, S.; Markovsky, B.; Aurbach, D.; Dixit, M.; Major, D.T. Layered Cathode Materials for Lithium-Ion Batteries: Review of Computational Studies on  $\text{LiNi}_{1-x-y}\text{Co}_x\text{Mn}_y\text{O}_2$  and  $\text{LiNi}_{1-x-y}\text{Co}_x\text{Al}_y\text{O}_2$ . *Chem. Mater.* **2020**, *32*, 915–952, doi:10.1021/acs.chemmater.9b04066.
17. Venkatraman, S.; Subramanian, V.; Gopu Kumar, S.; Renganathan, N.; Muniyandi, N. Capacity of layered cathode materials for lithium-ion batteries — a theoretical study and experimental evaluation. *Electrochemistry Communications* **2000**, *2*, 18–22, doi:10.1016/S1388-2481(99)00127-7.

18. Solchenbach, S.; Wetjen, M.; Pritzl, D.; Schwenke, K.U.; Gasteiger, H.A. Lithium Oxalate as Capacity and Cycle-Life Enhancer in LNMO/Graphite and LNMO/SiG Full Cells. *J. Electrochem. Soc.* **2018**, *165*, A512-A524, doi:10.1149/2.0611803jes.
19. Purwanto, A.; Yudha, C.S.; Ubaidillah, U.; Widiyandari, H.; Ogi, T.; Haerudin, H. NCA cathode material: synthesis methods and performance enhancement efforts. *Mater. Res. Express* **2018**, *5*, 122001, doi:10.1088/2053-1591/aae167.
20. Wang, Z.-H.; Yuan, L.-X.; Zhang, W.-X.; Huang, Y.-H. LiFe<sub>0.8</sub>Mn<sub>0.2</sub>PO<sub>4</sub>/C cathode material with high energy density for lithium-ion batteries. *Journal of Alloys and Compounds* **2012**, *532*, 25–30, doi:10.1016/j.jallcom.2012.04.008.
21. Gourley, S.W.D.; Or, T.; Chen, Z. Breaking Free from Cobalt Reliance in Lithium-Ion Batteries. *iScience* **2020**, *23*, 101505, doi:10.1016/j.isci.2020.101505.
22. Becher, K.; Lagodzinski, J.A.G.; Strufe, T. Privacy-Preserving Public Verification of Ethical Cobalt Sourcing. In *2020 IEEE 19th International Conference on Trust, Security and Privacy in Computing and Communications (TrustCom)*. 2020 IEEE 19th International Conference on Trust, Security and Privacy in Computing and Communications (TrustCom), Guangzhou, China, 29 Dec. 2020 – 01 Jan. 2021; IEEE, 2020 - 2021; pp 998–1005, ISBN 978-1-6654-0392-4.
23. Henckens, M.; Worrell, E. Reviewing the availability of copper and nickel for future generations. The balance between production growth, sustainability and recycling rates. *J. Clean. Prod.* **2020**, *264*, 121460, doi:10.1016/j.jclepro.2020.121460.
24. Genchi, G.; Carocci, A.; Lauria, G.; Sinicropi, M.S.; Catalano, A. Nickel: Human Health and Environmental Toxicology. *Int. J. Environ. Res. Public Health* **2020**, *17*, doi:10.3390/ijerph17030679.
25. Dohmann, J. *Experimentelle Einführung in die Elektrochemie*; Springer Berlin Heidelberg: Berlin, Heidelberg, 2020, ISBN 978-3-662-59762-0.
26. Buqa, H.; Blyth, R.; Golob, P.; Evers, B.; Schneider, I.; Santis Alvarez, M.V.; Hofer, F.; Netzer, F.P.; Ramsey, M.G.; Winter, M.; et al. Negative Electrodes in Rechargeable Lithium Ion Batteries - Influence of Graphite Surface Modification on the Formation of the Solid Electrolyte Interphase. *Ionics* **2000**, *6*, 172–179.
27. Heidari, E.K.; Kamyabi-Gol, A.; Sohi, M.H.; Ataie, A. Electrode Materials for Lithium Ion Batteries: A Review. *Journal of Ultrafine Grained and Nanostructured Materials* **2018**, *51*, 1–12, doi:10.22059/JUFGNSM.2018.01.01.
28. An, S.J.; Li, J.; Daniel, C.; Mohanty, D.; Nagpure, S.; Wood, D.L. The state of understanding of the lithium-ion-battery graphite solid electrolyte interphase (SEI) and its relationship to formation cycling. *Carbon* **2016**, *105*, 52–76, doi:10.1016/j.carbon.2016.04.008.
29. Li, D.; Danilov, D.; Zhang, Z.; Chen, H.; Yang, Y.; Notten, P.H.L. Modeling the SEI-Formation on Graphite Electrodes in LiFePO<sub>4</sub> Batteries. *J. Electrochem. Soc.* **2015**, *162*, A858-A869, doi:10.1149/2.0161506jes.
30. Toigo, C.; Frankenberger, M.; Billot, N.; Pscherer, C.; Stumper, B.; Distelrath, F.; Schubert, J.; Pettinger, K.-H.; Arbizzani, C. Improved Li<sub>4</sub>Ti<sub>5</sub>O<sub>12</sub> electrodes by modified current collector surface. *Electrochim. Acta* **2021**, *392*, 138978, doi:10.1016/j.electacta.2021.138978.
31. Zuo, X.; Zhu, J.; Müller-Buschbaum, P.; Cheng, Y.-J. Silicon based lithium-ion battery anodes: A chronicle perspective review. *Nano Energy* **2017**, *31*, 113–143, doi:10.1016/j.nanoen.2016.11.013.
32. Wang, A.; Kadam, S.; Li, H.; Shi, S.; Qi, Y. Review on modeling of the anode solid electrolyte interphase (SEI) for lithium-ion batteries. *npj Comput Mater* **2018**, *4*, doi:10.1038/s41524-018-0064-0.

33. Jara, A.D.; Betemariam, A.; Woldetinsae, G.; Kim, J.Y. Purification, application and current market trend of natural graphite: A review. *International Journal of Mining Science and Technology* **2019**, *29*, 671–689, doi:10.1016/j.ijmst.2019.04.003.
34. Köllner, C. Öko-Probleme bei den Batterie-Rohstoffen Lithium und Graphit. Available online: <https://www.springerprofessional.de/batterie/ressourceneinsatz/oeko-probleme-bei-den-batterierohstoffen-lithium-und-graphit/18790148>.
35. Xing, B.; Zhang, C.; Cao, Y.; Huang, G.; Liu, Q.; Zhang, C.; Chen, Z.; Yi, G.; Chen, L.; Yu, J. Preparation of synthetic graphite from bituminous coal as anode materials for high performance lithium-ion batteries. *Fuel Processing Technology* **2018**, *172*, 162–171, doi:10.1016/j.fuproc.2017.12.018.
36. Wissler, M. Graphite and carbon powders for electrochemical applications. *J. Power Sources* **2006**, *156*, 142–150, doi:10.1016/j.jpowsour.2006.02.064.
37. Banek, N.A.; Abele, D.T.; McKenzie, K.R.; Wagner, M.J. Sustainable Conversion of Lignocellulose to High-Purity, Highly Crystalline Flake Potato Graphite. *ACS Sustainable Chem. Eng.* **2018**, *6*, 13199–13207, doi:10.1021/acssuschemeng.8b02799.
38. Chou, S.-H.; Wang, J.-Z.; Liu, H.-K.; Dou, S.-X. Rapid synthesis of LTO microspheres as Anode Materials and Its Binder Effect for Lithium-Ion Battery. *J. Phys. Chem.* **2011**, *115*, 16220–16227.
39. Jiang, J.; Nie, P.; Ding, B.; Wu, W.; Chang, Z.; Wu, Y.; Dou, H.; Zhang, X. Effect of Graphene Modified Cu Current Collector on the Performance of Li<sub>4</sub>Ti<sub>5</sub>O<sub>12</sub> Anode for Lithium-Ion Batteries. *ACS Appl. Mater. Interfaces* **2016**, *8*, 30926–30932, doi:10.1021/acsaami.6b10038.
40. Sandhya, C.P.; John, B.; Gouri, C. Lithium titanate as anode material for lithium-ion cells: a review. *Ionics* **2014**, *20*, 601–620, doi:10.1007/s11581-014-1113-4.
41. Giorgio, F. de; La Monaca, A.; Dinter, A.; Frankenberger, M.; Pettinger, K.-H.; Arbizzani, C. Water-processable Li<sub>4</sub>Ti<sub>5</sub>O<sub>12</sub> electrodes featuring eco-friendly sodium alginate binder. *Electrochim. Acta* **2018**, *289*, 112–119.
42. Sun, X.; Radovanovic, P.V.; Cui, B. Advances in spinel Li<sub>4</sub>Ti<sub>5</sub>O<sub>12</sub> anode materials for lithium-ion batteries. *New J. Chem.* **2015**, *39*, 38–63, doi:10.1039/C4NJ01390E.
43. He, S.; Huang, S.; Wang, S.; Mizota, I.; Liu, X.; Hou, X. Considering Critical Factors of Silicon/Graphite Anode Materials for Practical High-Energy Lithium-Ion Battery Applications. *Energy Fuels* **2021**, *35*, 944–964, doi:10.1021/acs.energyfuels.0c02948.
44. Phanikumar, V.; Rikka, V.R.; Das, B.; Gopalan, R.; Rao, B.V.; Prakash, R. Investigation on polyvinyl alcohol and sodium alginate as aqueous binders for lithium-titanium oxide anode in lithium-ion batteries. *Ionics* **2019**, *25*, 2549–2561.
45. Toigo, C.; Kracalik, M.; Bradt, E.; Pettinger, K.-H.; Arbizzani, C. Rheological Properties of Aqueous Sodium Alginate Slurries for LTO Battery Electrodes. *Polymers (Basel)* **2021**, *13*, 3582, doi:10.3390/polym13203582.
46. Mo, L.; Zheng, H. Solid coated Li<sub>4</sub>Ti<sub>5</sub>O<sub>12</sub> (LTO) using polyaniline (PANI) as anode materials for improving thermal safety for lithium ion battery. *Energy Reports* **2020**, *6*, 2913–2918, doi:10.1016/j.egyr.2020.10.018.
47. Wang, J.; Liu, X.-M.; Yang, H.; Shen, X. Characterization and electrochemical properties of carbon-coated Li<sub>4</sub>Ti<sub>5</sub>O<sub>12</sub> prepared by a citric acid sol-gel method. *Journal of Alloys and Compounds* **2011**, *509*, 712–718, doi:10.1016/j.jallcom.2010.07.215.
48. Carvalho, D.V.; Loeffler, N.; Kim, G.-T.; Marinaro, M.; Wohlfahrt-Mehrens, M.; Passerini, S. Study of Water-Based Lithium Titanate Electrode Processing: The Role of pH and Binder Molecular Structure. *Polymers (Basel)* **2016**, *8*, doi:10.3390/polym8080276.
49. Toigo, C.; Singh, M.; Gmeiner, B.; Bisio, M.; Pettinger, K.-H. A Method to Measure the Swelling of Water-Soluble PVDF Binder System and Its Electrochemical Performance for Lithium Ion Batteries. *J. Electrochem. Soc.* **2020**, *167*, 20514.

50. Toigo, C.; Arbizzani, C.; Pettinger, K.-H.; Bisio, M. Study on Different Water-Based Binders for Li<sub>4</sub>Ti<sub>5</sub>O<sub>12</sub> Electrodes. *Molecules* **2020**, *25*, doi:10.3390/molecules25102443.
51. Birrozzi, A.; Copley, M.; Zamory, J. von; Pasqualini, M.; Calcaterra, S.; Nobili, F.; Di Cicco, A.; Rajantie, H.; Briceno, M.; Bilb , E.; et al. Scaling up “Nano” Li<sub>4</sub>Ti<sub>5</sub>O<sub>12</sub> for High-Power Lithium-Ion Anodes Using Large Scale Flame Spray Pyrolysis. *J. Electrochem. Soc.* **2015**, *162*, A2331-A2338, doi:10.1149/2.0711512jes.
52. Karuppiah, S.; Franger, S.; Nallathamby, K. Water-soluble green binder for Li<sub>4</sub>Ti<sub>5</sub>O<sub>12</sub> anodes: Effect of binder choice on Lithium Storage. *ChemElectroChem* **2018**, *5*, 343–349.
53. Tran, B.; Oladeji, I.O.; Wang, Z.; Calderon, J.; Chai, G.; Atherton, D.; Zhai, L. Adhesive PEG-based binder for aqueous fabrication of thick LTO electrode. *Electrochim. Acta* **2013**, *88*.
54. Kim, S.-J.; Lee, B.-R.; Oh, E.-S. Application of a bio-derivative, rosin, as a binder additive for lithium titanium oxide electrodes in lithium-ion batteries. *J. Power Sources* **2015**, *273*, 608–612, doi:10.1016/j.jpowsour.2014.09.160.
55. Salvatore, K.L.; Lutz, D.M.; Guo, H.; Yue, S.; Gan, J.; Tong, X.; Liu, P.; Takeuchi, E.S.; Takeuchi, K.J.; Marschilok, A.C.; et al. Solution-Based, Anion-Doping of Li<sub>4</sub>Ti<sub>5</sub>O<sub>12</sub> Nanoflowers for Lithium-Ion Battery Applications. *Chemistry* **2020**, *26*, 9389–9402, doi:10.1002/chem.202002489.
56. Wu, H.-C.; Lin, Y.-P.; Lee, E.; Lin, W.-T.; Hu, J.-K.; Chen, H.-C.; Wu, N.-L. High-performance carbon-based supercapacitors using Al current-collector with conformal carbon coating. *Materials Chemistry and Physics* **2009**, *117*, 294–300, doi:10.1016/j.matchemphys.2009.06.001.
57. Zhang, N.; Zheng, Y.; Trifonova, A.; Pfl ging, W. Laser structured Cu foil for high-performance lithium-ion battery anodes. *J Appl Electrochem* **2017**, *47*, 829–837, doi:10.1007/s10800-017-1086-x.
58. Pfl ging, W.; Mangang, M.; Zheng, Y.; Smyrek, P. Laser structuring for improved battery performance. *SPIE Newsroom* **2016**, doi:10.1117/2.1201602.006342.
59. Kang, S.; Xie, H.; Zhai, W.; Ma, Z.; Wang, R.; Zhang, W. Enhancing performance of a Lithium Ion Battery by Optimizing the Surface Properties of the Current Collector. *International Journal of Electrochemical Science* **2015**, *10*, 2324–2335.
60. Nakamura, T.; Okano, S.; Yaguma, N.; Morinaga, Y.; Takahara, H.; Yamada, Y. Electrochemical performance of cathodes prepared on current collector with different surface morphologies. *J. Power Sources* **2013**, *244*, 532–537, doi:10.1016/j.jpowsour.2013.02.021.
61. Zheng, Y.; An, Z.; Smyrek, P.; Seifert, H.J.; Pfl ging, W.; Kunze, T.; Lang, V.; Lasagni, A.F. Laser interference patterning and laser-induced periodic surface structure formation on metallic substrates. In *2016 IEEE International Conference on Manipulation, Manufacturing and Measurement on the Nanoscale (3M-NANO)*. 2016 IEEE International Conference on Manipulation, Manufacturing and Measurement on the Nanoscale (3M-NANO), Chongqing, China, 18–22 Jul. 2016; IEEE, 2016 - 2016; pp 159–163, ISBN 978-1-5090-2945-7.
62. Tang, J.; Dysart, A.D.; Kim, D.H.; Saraswat, R.; Shaver, G.M.; Pol, V.G. Fabrication of Carbon/Silicon Composite as Lithium-ion Anode with Enhanced Cycling Stability. *Electrochim. Acta* **2017**, *247*, 626–633, doi:10.1016/j.electacta.2017.06.178.
63. Zhao, T.; Meng, Y.; Yin, H.; Guo, K.; Ji, R.; Zhang, G.; Zhang, Y. Beneficial effect of green water-soluble binders on SiO<sub>x</sub>/graphite anode for lithium-ion batteries. *Chemical Physics Letters* **2020**, *742*, 137145, doi:10.1016/j.cplett.2020.137145.
64. Schiele, A.; Breitung, B.; Mazilkin, A.; Schweidler, S.; Janek, J.; Gumbel, S.; Fleischmann, S.; Burakowska-Meise, E.; Sommer, H.; Brezesinski, T. Silicon Nanoparticles with a Polymer-Derived Carbon Shell for Improved Lithium-Ion Batteries: Investigation into Volume Expansion, Gas Evolution, and Particle Fracture. *ACS Omega* **2018**, *3*, 16706–16713, doi:10.1021/acsomega.8b02541.

65. Schweidler, S.; Biasi, L. de; Schiele, A.; Hartmann, P.; Brezesinski, T.; Janek, J. Volume Changes of Graphite Anodes Revisited: A Combined Operando X-ray Diffraction and In Situ Pressure Analysis Study. *J. Phys. Chem. C* **2018**, *122*, 8829–8835, doi:10.1021/acs.jpcc.8b01873.
66. Wagner, M.R.; Raimann, P.R.; Trifonova, A.; Möller, K.-C.; Besenhard, J.O.; Winter, M. Dilatometric and mass spectrometric investigations on lithium ion battery anode materials. *Anal. Bioanal. Chem.* **2004**, *379*, 272–276, doi:10.1007/s00216-004-2570-9.
67. Casimir, A.; Zhang, H.; Ogoke, O.; Amine, J.C.; Lu, J.; Wu, G. Silicon-based anodes for lithium-ion batteries: Effectiveness of materials synthesis and electrode preparation. *Nano Energy* **2016**, *27*, 359–376, doi:10.1016/j.nanoen.2016.07.023.
68. Hunter, J. Preparation of a new crystal form of Manganese Dioxide:  $\lambda$ -MnO<sub>2</sub>. *Journal of Solid State Chemistry* **1981**, *39*, 142–147.
69. Liao, L.; Cheng, X.; Ma, Y.; Zuo, P.; Fang, W.; Yin, G.; Gao, Y. Fluoroethylene carbonate as electrolyte additive to improve low temperature performance of LiFePO<sub>4</sub> electrode. *Electrochim. Acta* **2013**, *87*, 466–472, doi:10.1016/j.electacta.2012.09.083.
70. Hall, D.S.; Self, J.; Dahn, J.R. Dielectric Constants for Quantum Chemistry and Li-Ion Batteries: Solvent Blends of Ethylene Carbonate and Ethyl Methyl Carbonate. *J. Phys. Chem. C* **2015**, *119*, 22322–22330, doi:10.1021/acs.jpcc.5b06022.
71. Zhu, J.; Yanilmaz, M.; Fu, K.; Chen, C.; Lu, Y.; Ge, Y.; Kim, D.; Zhang, X. Understanding glass fiber membrane used as a novel separator for lithium–sulfur batteries. *Journal of Membrane Science* **2016**, *504*, 89–96, doi:10.1016/j.memsci.2016.01.020.
72. Xiang, Y.; Li, J.; Lei, J.; Liu, D.; Xie, Z.; Qu, D.; Li, K.; Deng, T.; Tang, H. Advanced Separators for Lithium-Ion and Lithium-Sulfur Batteries: A Review of Recent Progress. *ChemSusChem* **2016**, *9*, 3023–3039, doi:10.1002/cssc.201600943.
73. Pereira, R.F.P.; Brito-Pereira, R.; Gonçalves, R.; Silva, M.P.; Costa, C.M.; Silva, M.M.; Zea Bermudez, V. de; Lanceros-Méndez, S. Silk Fibroin Separators: A Step Toward Lithium-Ion Batteries with Enhanced Sustainability. *ACS Appl. Mater. Interfaces* **2018**, *10*, 5385–5394, doi:10.1021/acsami.7b13802.
74. Reizabal, A.; Gonçalves, R.; Fidalgo-Marijuan, A.; Costa, C.M.; Pérez, L.; Vilas, J.-L.; Lanceros-Mendez, S. Tailoring silk fibroin separator membranes pore size for improving performance of lithium ion batteries. *Journal of Membrane Science* **2020**, *598*, 117678, doi:10.1016/j.memsci.2019.117678.
75. Barbosa, J.C.; Reizabal, A.; Correia, D.M.; Fidalgo-Marijuan, A.; Gonçalves, R.; Silva, M.M.; Lanceros-Mendez, S.; Costa, C.M. Lithium-ion battery separator membranes based on poly(L-lactic acid) biopolymer. *Materials Today Energy* **2020**, *18*, 100494, doi:10.1016/j.mtener.2020.100494.
76. Tan, L.; Li, Z.; Shi, R.; Quan, F.; Wang, B.; Ma, X.; Ji, Q.; Tian, X.; Xia, Y. Preparation and Properties of an Alginate-Based Fiber Separator for Lithium-Ion Batteries. *ACS Appl. Mater. Interfaces* **2020**, *12*, 38175–38182, doi:10.1021/acsami.0c10630.
77. Song, Q.; Li, A.; Shi, L.; Qian, C.; Feric, T.G.; Fu, Y.; Zhang, H.; Li, Z.; Wang, P.; Li, Z.; et al. Thermally stable, nano-porous and eco-friendly sodium alginate/attapulgitite separator for lithium-ion batteries. *Energy Storage Mater.* **2019**, *22*, 48–56, doi:10.1016/j.ensm.2019.06.033.
78. Gwon, H.; Park, K.; Chung, S.-C.; Kim, R.-H.; Kang, J.K.; Ji, S.M.; Kim, N.-J.; Lee, S.; Ku, J.-H.; Do, E.C.; et al. A safe and sustainable bacterial cellulose nanofiber separator for lithium rechargeable batteries. *Proc. Natl. Acad. Sci. U. S. A.* **2019**, *116*, 19288–19293, doi:10.1073/pnas.1905527116.
79. Zhang, T.-W.; Shen, B.; Yao, H.-B.; Ma, T.; Lu, L.-L.; Zhou, F.; Yu, S.-H. Prawn Shell Derived Chitin Nanofiber Membranes as Advanced Sustainable Separators for Li/Na-Ion Batteries. *Nano Lett.* **2017**, *17*, 4894–4901, doi:10.1021/acs.nanolett.7b01875.

80. Satyavani, T.; Ramya Kiran, B.; Rajesh Kumar, V.; Srinivas Kumar, A.; Naidu, S.V. Effect of particle size on dc conductivity, activation energy and diffusion coefficient of lithium iron phosphate in Li-ion cells. *Engineering Science and Technology, an International Journal* **2016**, *19*, 40–44, doi:10.1016/j.jestch.2015.05.011.
81. Qiang, G.; Hong, W.; Xiao-Zhen, L.; Wei, M.A.; Yu-Shi, H.E.; Zi-Feng, M.A. Electrochemical Performance of Vanadium Modified  $\text{LiFe}_{0.5}\text{Mn}_{0.5}\text{PO}_4/\text{C}$  Cathode Materials for Lithium-Ion Batteries. *Acta Physico-Chimica Sinica* **2012**, *28*, 100–104, doi:10.3866/PKU.WHXB201228100.
82. Huang, S.; Wen, Z.; Yang, X.; Gu, Z.; Xu, X. Improvement of the high-rate discharge properties of  $\text{LiCoO}_2$  with the Ag additives. *J. Power Sources* **2005**, *148*, 72–77, doi:10.1016/j.jpowsour.2005.02.002.
83. Hari Prasad, K.; Vinoth, S.; Ratnakar, A.; Venkateswarlu, M.; Satyanarayana, N. Structural and Electrical Conductivity studies of Spinel  $\text{LiMn}_2\text{O}_4$  Cathode films grown by RF Sputtering. *Materials Today: Proceedings* **2016**, *3*, 4046–4051, doi:10.1016/j.matpr.2016.11.071.
84. Hermawan, A.; Wibowo, A.; Asri, L.A.T.W.; Yin, S.; Purwasasmita, B.S. Improved ionic conductivity of porous  $\text{Li}_4\text{Ti}_5\text{O}_{12}$  synthesized by sol-gel method using eggshell membrane as soft template. *Mater. Res. Express* **2019**, *6*, 75030, doi:10.1088/2053-1591/ab1298.
85. Cai, Y.; Fan, C. Influences of conductive additives on electrochemical performances of artificial graphite anode with different shapes for lithium ion batteries. *Electrochim. Acta* **2011**, *58*, 481–487, doi:10.1016/j.electacta.2011.09.080.
86. Su, F.-Y.; You, C.; He, Y.-B.; Lv, W.; Cui, W.; Jin, F.; Li, B.; Yang, Q.-H.; Kang, F. Flexible and planar graphene conductive additives for lithium-ion batteries. *J. Mater. Chem.* **2010**, *20*, 9644, doi:10.1039/c0jm01633k.
87. Medvedev, O.S.; Wang, Q.; Popovich, A.A.; Novikov, P.A. Comparison of conductive additives for high-power applications of Li-ion batteries. *Ionics* **2020**, *26*, 4277–4286, doi:10.1007/s11581-020-03631-4.
88. Higgins, T.M.; Park, S.-H.; King, P.J.; Zhang, C.J.; McEvoy, N.; Berner, N.C.; Daly, D.; Shmeliov, A.; Khan, U.; Duesberg, G.; et al. A Commercial Conducting Polymer as Both Binder and Conductive Additive for Silicon Nanoparticle-Based Lithium-Ion Battery Negative Electrodes. *ACS Nano* **2016**, *10*, 3702–3713, doi:10.1021/acs.nano.6b00218.
89. Myung, S.-T.; Sasaki, Y.; Sakurada, S.; Sun, Y.-K.; Yashiro, H. Electrochemical behavior of current collectors for lithium batteries in non-aqueous alkyl carbonate solution and surface analysis by ToF-SIMS. *Electrochim. Acta* **2009**, *55*, 288–297, doi:10.1016/j.electacta.2009.08.051.
90. Fritsch, M.; Coeler, M.; Kunz, K.; Krause, B.; Marcinkowski, P.; Pötschke, P.; Wolter, M.; Michaelis, A. Lightweight Polymer-Carbon Composite Current Collector for Lithium-Ion Batteries. *Batteries* **2020**, *6*, 60, doi:10.3390/batteries6040060.
91. Zhu, P.; Gastol, D.; Marshall, J.; Sommerville, R.; Goodship, V.; Kendrick, E. A review of current collectors for lithium-ion batteries. *J. Power Sources* **2021**, *485*, 229321, doi:10.1016/j.jpowsour.2020.229321.
92. Zhang, Z.; Zeng, T.; Lai, Y.; Jia, M.; Li, J. A comparative study of different binders and their effects on electrochemical properties of  $\text{LiMn}_2\text{O}_4$  cathode in lithium ion batteries. *J. Power Sources* **2014**, *247*, 1–8.
93. Nirmale, T.C.; Kale, B.B.; Varma, A.J. A review on cellulose and lignin based binders and electrodes: Small steps towards a sustainable lithium ion battery. *Int. J. Biol. Macromol.* **2017**, *103*, 1032–1043, doi:10.1016/j.ijbiomac.2017.05.155.
94. Kovalenko, I.; Zdyrko, B.; Magasinski, A.; Hertzberg, B.; Milicev, Z.; Burtovyy, R.; Luzinov, I.; Yushin, G. A major constituent of brown algae for use in high-capacity Li-ion batteries. *Science* **2011**, *334*, 75–79, doi:10.1126/science.1209150.

95. Lee, B.-R.; Oh, E.-S. Effect of Molecular Weight and Degree of Substitution of a Sodium-Carboxymethyl Cellulose Binder on LTO Anodic Performance. *J. Phys. Chem.* **2013**, *117*, 4404–4409.
96. Bigoni, F.; Giorgio, F. de; Soavi, F.; Arbizzani, C. Sodium Alginate: A Water-Processable Binder in High-Voltage Cathode Formulations. *J. Electrochem. Soc.* **2017**, *164*, A6171-A6177, doi:10.1149/2.0281701jes.
97. Cuesta, N.; Ramos, A.; Cameán, I.; Antuña, C.; García, A.B. Hydrocolloids as binders for graphite anodes of lithium-ion batteries. *Electrochim. Acta* **2015**, *155*, 140–147, doi:10.1016/j.electacta.2014.12.122.
98. Lan, W.; He, L.; Liu, Y. Preparation and Properties of Sodium Carboxymethyl Cellulose/Sodium Alginate/Chitosan Composite Film. *Coatings* **2018**, *8*, 291, doi:10.3390/coatings8080291.
99. Samanta, H.S.; Ray, S.K. Synthesis, characterization, swelling and drug release behavior of semi-interpenetrating network hydrogels of sodium alginate and polyacrylamide. *Carbohydr. Polym.* **2014**, *99*, 666–678, doi:10.1016/j.carbpol.2013.09.004.
100. Ma, Y.; Ma, J.; Cui, G. Small things make big deal: Powerful binders of lithium batteries and post-lithium batteries. *Energy Storage Mater.* **2019**, *20*, 146–175, doi:10.1016/j.ensm.2018.11.013.
101. Magasinski, A.; Zdyrko, B.; Kovalenko, I.; Hertzberg, B.; Burtovyy, R.; Huebner, C.F.; Fuller, T.F.; Luzinov, I.; Yushin, G. Toward efficient binders for Li-ion battery Si-based anodes: Polyacrylic acid. *ACS Appl. Mater. Interfaces* **2010**, *2*, 3004–3010, doi:10.1021/am100871y.
102. Yoo, M.; Frank, C.W.; Mori, S. Interaction of Poly(vinylidene fluoride) with Graphite Particles. 1. Surface Morphology of a Composite Film and Its Relation to Processing Parameters. *Chem. Mater.* **2003**, *15*, 850–861, doi:10.1021/cm0209970.
103. Salini, P.S.; Gopinadh, S.V.; Kalpakasseri, A.; John, B.; Thelakkattu Devassy, M. Toward Greener and Sustainable Li-Ion Cells: An Overview of Aqueous-Based Binder Systems. *ACS Sustainable Chem. Eng.* **2020**, *8*, 4003–4025, doi:10.1021/acssuschemeng.9b07478.
104. Bresser, D.; Buchholz, D.; Moretti, A.; Varzi, A.; Passerini, S. Alternative binders for sustainable electrochemical energy storage – the transition to aqueous electrode processing and bio-derived polymers. *Energy Environ. Sci.* **2018**, *11*, 3096–3127, doi:10.1039/C8EE00640G.
105. Pohjalainen, E.; Räsänen, S.; Jokinen, M.; Yliniemi, K.; Worsley, D.A.; Kuusivaara, J.; Juurikivi, J.; Ekqvist, R.; Kallio, T.; Karppinen, M. Water soluble binder for fabrication of Li<sub>4</sub>Ti<sub>5</sub>O<sub>12</sub> electrodes. *J. Power Sources* **2013**, *226*, 134–139, doi:10.1016/j.jpowsour.2012.10.083.
106. Wennig, S.; Langklotz, U.; Prinz, G.M.; Schmidt, A.; Oberschachtsiek, B.; Lorke, A.; Heinzl, A. The influence of different pre-treatments of current collectors and variation of the binders on the performance of LTO anodes for lithium ion batteries. *J. Appl. Electrochem.* **2015**, *45*, 1043–1055.
107. Xu, J.; Chou, S.-L.; Gu, Q.; Liu, H.-K.; Dou, S.-X. The effect of different binders on electrochemical properties of LiNi<sub>1/3</sub>Mn<sub>1/3</sub>Co<sub>1/3</sub>O<sub>2</sub> cathode material in lithium ion batteries. *J. Power Sources* **2013**, *225*, 172–178, doi:10.1016/j.jpowsour.2012.10.033.
108. 2016 IEEE International Conference on Manipulation, Manufacturing and Measurement on the Nanoscale (3M-NANO). 2016 IEEE International Conference on Manipulation, Manufacturing and Measurement on the Nanoscale (3M-NANO), Chongqing, China, 18–22 Jul. 2016; IEEE, 2016 - 2016.
109. Vasileiadis, A.; Klerk, N. de; Smith, R.; Ganapathy, S.; Harks, P.; Bazant, M.; Wagemaker, M. Toward optimal performance and in-depth understanding of spinel Li<sub>4</sub>Ti<sub>5</sub>O<sub>12</sub> electrodes through Phase Field Modeling. *Adv. Funct. Mater.* **2018**, *28*, 1705992.
110. Zhu, G.-N.; Liu, H.-J.; Zhuang, J.-H.; Wang, C.-X.; Wang, Y.-G.; Xia, Y.-Y. Carbon-coated nano-sized Li<sub>4</sub>Ti<sub>5</sub>O<sub>12</sub> nanoporous micro-sphere as anode material for high-rate lithium-ion batteries. *Energy Environ. Sci.* **2011**, *4*, 4016, doi:10.1039/c1ee01680f.

111. Braun, D.; Cherdrón, H.; Rehahn, M.; Ritter, H.; Voit, B. *Polymer Synthesis: Theory and Practice*; Springer Berlin Heidelberg: Berlin, Heidelberg, 2013, ISBN 978-3-642-28979-8.
112. Osswald, T.A. *Understanding Polymer Processing*; Carl Hanser Verlag GmbH & Co. KG: München, 2017, ISBN 978-1-56990-647-7.
113. Kaiser, J.; Wenzel, V.; Nirschl, H.; Bitsch, B.; Willenbacher, N.; Baunach, M.; Schmitt, M.; Jaiser, S.; Scharfer, P.; Schabel, W. Prozess- und Produktentwicklung von Elektroden für Li-Ionen-Zellen. *Chemie Ingenieur Technik* **2014**, *86*, 695–706, doi:10.1002/cite.201300085.
114. Li, C.-C.; Wang, Y.-W. Importance of binder compositions to the dispersion and electrochemical properties of water-based LiCoO<sub>2</sub> cathodes. *J. Power Sources* **2013**, *227*, 204–210, doi:10.1016/j.jpowsour.2012.11.025.
115. Schällicke, G.; Landwehr, I.; Dinter, A.; Pettinger, K.-H.; Haselrieder, W.; Kwade, A. Solvent-Free Manufacturing of Electrodes for Lithium-Ion Batteries via Electrostatic Coating. *Energy Technol.* **2020**, *8*, 1900309, doi:10.1002/ente.201900309.
116. Bauer, W. Besonderheiten der Pulvertechnologie bei der Herstellung von Lithium-Ionen-Batterien. *Keram. Z.* **2019**, *71*, 42–47, doi:10.1007/s42410-018-0055-2.
117. Korthauer, R. *Handbuch Lithium-Ionen-Batterien*; Springer Berlin Heidelberg: Berlin, Heidelberg, 2013, ISBN 978-3-642-30652-5.
118. Huang, B.; Pan, Z.; Su, X.; An, L. Recycling of lithium-ion batteries: Recent advances and perspectives. *J. Power Sources* **2018**, *399*, 274–286, doi:10.1016/j.jpowsour.2018.07.116.
119. Yao, Y.; Zhu, M.; Zhao, Z.; Tong, B.; Fan, Y.; Hua, Z. Hydrometallurgical Processes for Recycling Spent Lithium-Ion Batteries: A Critical Review. *ACS Sustainable Chem. Eng.* **2018**, *6*, 13611–13627, doi:10.1021/acssuschemeng.8b03545.
120. Kamath, D.; Arsenault, R.; Kim, H.C.; Anctil, A. Economic and Environmental Feasibility of Second-Life Lithium-Ion Batteries as Fast-Charging Energy Storage. *Environ. Sci. Technol.* **2020**, *54*, 6878–6887, doi:10.1021/acs.est.9b05883.
121. Neubauer, J.S.; Wood, E.; Pesaran, A. A Second Life for Electric Vehicle Batteries: Answering Questions on Battery Degradation and Value. *SAE Int. J. Mater. Manf.* **2015**, *8*, 544–553, doi:10.4271/2015-01-1306.
122. Jiang, Y.; Jiang, J.; Zhang, C.; Zhang, W.; Gao, Y.; Li, N. State of health estimation of second-life LiFePO<sub>4</sub> batteries for energy storage applications. *J. Clean. Prod.* **2018**, *205*, 754–762, doi:10.1016/j.jclepro.2018.09.149.
123. Hasa, I.; Mariyappan, S.; Saurel, D.; Adelhelm, P.; Kuposov, A.Y.; Masquelier, C.; Croguennec, L.; Casas-Cabanas, M. Challenges of today for Na-based batteries of the future: From materials to cell metrics. *J. Power Sources* **2021**, *482*, 228872, doi:10.1016/j.jpowsour.2020.228872.
124. Nayak, P.K.; Yang, L.; Brehm, W.; Adelhelm, P. From Lithium-Ion to Sodium-Ion Batteries: Advantages, Challenges, and Surprises. *Angew. Chem. Int. Ed Engl.* **2018**, *57*, 102–120, doi:10.1002/anie.201703772.
125. Hirsh, H.S.; Li, Y.; Tan, D.H.S.; Zhang, M.; Zhao, E.; Meng, Y.S. Sodium-Ion Batteries Paving the Way for Grid Energy Storage. *Adv. Energy Mater.* **2020**, *10*, 2001274, doi:10.1002/aenm.202001274.
126. Mining.com. Lithium price rally accelerates in September: 2021. Available online: <https://www.mining.com/lithium-price-rally-accelerates-in-september/>.
127. Chen, S.; Wu, C.; Shen, L.; Zhu, C.; Huang, Y.; Xi, K.; Maier, J.; Yu, Y. Challenges and Perspectives for NASICON-Type Electrode Materials for Advanced Sodium-Ion Batteries. *Adv. Mater.* **2017**, *29*, doi:10.1002/adma.201700431.
128. Jin, T.; Li, H.; Zhu, K.; Wang, P.-F.; Liu, P.; Jiao, L. Polyanion-type cathode materials for sodium-ion batteries. *Chem. Soc. Rev.* **2020**, *49*, 2342–2377, doi:10.1039/c9cs00846b.

129. Qian, J.; Wu, C.; Cao, Y.; Ma, Z.; Huang, Y.; Ai, X.; Yang, H. Prussian Blue Cathode Materials for Sodium-Ion Batteries and Other Ion Batteries. *Adv. Energy Mater.* **2018**, *8*, 1702619, doi:10.1002/aenm.201702619.
130. Xiang, X.; Zhang, K.; Chen, J. Recent Advances and Prospects of Cathode Materials for Sodium-Ion Batteries. *Adv. Mater.* **2015**, *27*, 5343–5364, doi:10.1002/adma.201501527.
131. Kitta, M.; KATAOKA, R.; Tanaka, S.; Takeichi, N.; Kohyama, M. Spinel-Type Sodium Titanium Oxide: A Promising Sodium-Insertion Material of Sodium-Ion Batteries. *ACS Appl. Energy Mater.* **2019**, *2*, 4345–4353, doi:10.1021/acsaem.9b00541.
132. Mogensen, R.; Colbin, S.; Younesi, R. An Attempt to Formulate Non-Carbonate Electrolytes for Sodium-Ion Batteries. *Batteries & Supercaps* **2021**, *4*, 791–814, doi:10.1002/batt.202000252.
133. Morales, D.; Chagas, L.G.; Paterno, D.; Greenbaum, S.; Passerini, S.; Suarez, S. Transport studies of NaPF<sub>6</sub> carbonate solvents-based sodium ion electrolytes. *Electrochim. Acta* **2021**, *377*, 138062, doi:10.1016/j.electacta.2021.138062.
134. Suo, L.; Borodin, O.; Wang, Y.; Rong, X.; Sun, W.; Fan, X.; Xu, S.; Schroeder, M.A.; Cresce, A.V.; Wang, F.; et al. “Water-in-Salt” Electrolyte Makes Aqueous Sodium-Ion Battery Safe, Green, and Long-Lasting. *Adv. Energy Mater.* **2017**, *7*, 1701189, doi:10.1002/aenm.201701189.
135. Han, J.; Zhang, H.; Varzi, A.; Passerini, S. Fluorine-Free Water-in-Salt Electrolyte for Green and Low-Cost Aqueous Sodium-Ion Batteries. *ChemSusChem* **2018**, *11*, 3704–3707, doi:10.1002/cssc.201801930.
136. Coustan, L.; Tarascon, J.-M.; Laberty-Robert, C. Thin Fiber-Based Separators for High-Rate Sodium Ion Batteries. *ACS Appl. Energy Mater.* **2019**, *2*, 8369–8375, doi:10.1021/acsaem.9b01821.
137. Zhang, L.; Li, X.; Yang, M.; Chen, W. High-safety separators for lithium-ion batteries and sodium-ion batteries: advances and perspective. *Energy Storage Mater.* **2021**, *41*, 522–545, doi:10.1016/j.ensm.2021.06.033.
138. Ojanguren, A.; Mittal, N.; Lizundia, E.; Niederberger, M. Stable Na Electrodeposition Enabled by Agarose-Based Water-Soluble Sodium Ion Battery Separators. *ACS Appl. Mater. Interfaces* **2021**, *13*, 21250–21260, doi:10.1021/acsaem.1c02135.
139. Chen, W.; Zhang, L.; Liu, C.; Feng, X.; Zhang, J.; Guan, L.; Mi, L.; Cui, S. Electrospun Flexible Cellulose Acetate-Based Separators for Sodium-Ion Batteries with Ultralong Cycle Stability and Excellent Wettability: The Role of Interface Chemical Groups. *ACS Appl. Mater. Interfaces* **2018**, *10*, 23883–23890, doi:10.1021/acsaem.8b06706.
140. Ni, J.; Li, L.; Lu, J. Phosphorus: An Anode of Choice for Sodium-Ion Batteries. *ACS Energy Lett.* **2018**, *3*, 1137–1144, doi:10.1021/acsaem.8b00312.
141. Fan, T.-E.; Xie, H.-F. Sb<sub>2</sub>S<sub>3</sub>-rGO for high-performance sodium-ion battery anodes on Al and Cu foil current collector. *Journal of Alloys and Compounds* **2019**, *775*, 549–553, doi:10.1016/j.jallcom.2018.10.103.
142. Otaegui, L.; Goikolea, E.; Aguesse, F.; Armand, M.; Rojo, T.; Singh, G. Effect of the electrolytic solvent and temperature on aluminium current collector stability: A case of sodium-ion battery cathode. *J. Power Sources* **2015**, *297*, 168–173, doi:10.1016/j.jpowsour.2015.07.084.
143. Bhide, A.; Hofmann, J.; Dürr, A.K.; Janek, J.; Adelhelm, P. Electrochemical stability of non-aqueous electrolytes for sodium-ion batteries and their compatibility with Na<sub>0.7</sub>CoO<sub>2</sub>. *Phys. Chem. Chem. Phys.* **2014**, *16*, 1987–1998, doi:10.1039/c3cp53077a.
144. Jin, T.; Han, Q.; Jiao, L. Binder-Free Electrodes for Advanced Sodium-Ion Batteries. *Adv. Mater.* **2020**, *32*, e1806304, doi:10.1002/adma.201806304.
145. Kim, T.; Choi, W.; Shin, H.-C.; Choi, J.-Y.; Kim, J.M.; Park, M.-S.; Yoon, W.-S. Applications of Voltammetry in Lithium Ion Battery Research. *J. Electrochem. Sci. Te.* **2020**, *11*, 14–25, doi:10.33961/jecst.2019.00619.

146. Demtröder, W. *Experimentalphysik 2*; Springer Berlin Heidelberg: Berlin, Heidelberg, 2013, ISBN 978-3-642-29943-8.
147. Habedank, J.B.; Kraft, L.; Rheinfeld, A.; Krezdorn, C.; Jossen, A.; Zaeh, M.F. Increasing the Discharge Rate Capability of Lithium-Ion Cells with Laser-Structured Graphite Anodes: Modeling and Simulation. *J. Electrochem. Soc.* **2018**, *165*, A1563-A1573, doi:10.1149/2.1181807jes.
148. Morasch, R.; Landesfeind, J.; Suthar, B.; Gasteiger, H.A. Detection of Binder Gradients Using Impedance Spectroscopy and Their Influence on the Tortuosity of Li-Ion Battery Graphite Electrodes. *J. Electrochem. Soc.* **2018**, *165*, A3459-A3467, doi:10.1149/2.1021814jes.
149. Billot, N.; Günther, T.; Schreiner, D.; Stahl, R.; Kranner, J.; Beyer, M.; Reinhart, G. Investigation of the Adhesion Strength along the Electrode Manufacturing Process for Improved Lithium-Ion Anodes. *Energy Technol.* **2020**, *8*, 1801136, doi:10.1002/ente.201801136.
150. Yan, S.; Xiao, X.; Huang, X.; Li, X.; Qi, Y. Unveiling the environment-dependent mechanical properties of porous polypropylene separators. *Polymer* **2014**, *55*, 6282–6292, doi:10.1016/j.polymer.2014.09.067.
151. Stanga, M. New Solef PVDF aqueous dispersions for Lithium batteries: Green PVDF for green batteries. In *Stakeholders Conference on ELIBAMA project*; Jerome Peyrard, Ed., 2014.
152. *Introduction to Fluoropolymers*; Elsevier, 2013, ISBN 9781455774425.
153. Spreafico, M.A.; Cojocar, P.; Magagnin, L.; Triulzi, F.; Apostolo, M. PVDF Latex As a Binder for Positive Electrodes in Lithium-Ion Batteries. *Ind. Eng. Chem. Res.* **2014**, *53*, 9094–9100, doi:10.1021/ie403239s.
154. Qian, J.; Wiener, C.G.; Zhu, Y.; Vogt, B.D. Swelling and plasticization of polymeric binders by Li-containing carbonate electrolytes using quartz crystal microbalance with dissipation. *Polymer* **2018**, *143*, 237–244, doi:10.1016/j.polymer.2018.04.021.
155. Bülter, H.; Peters, F.; Schwenzel, J.; Wittstock, G. In Situ Quantification of the Swelling of Graphite Composite Electrodes by Scanning Electrochemical Microscopy. *J. Electrochem. Soc.* **2016**, *163*, A27-A34, doi:10.1149/2.1061514jes.
156. Zhang, N.; Tang, H. Dissecting anode swelling in commercial lithium-ion batteries. *J. Power Sources* **2012**, *218*, 52–55, doi:10.1016/j.jpowsour.2012.06.071.
157. Costa, C.M.; Gomez Ribelles, J.L.; Lanceros-Méndez, S.; Appetecchi, G.B.; Scrosati, B. Poly(vinylidene fluoride)-based, co-polymer separator electrolyte membranes for lithium-ion battery systems. *J. Power Sources* **2014**, *245*, 779–786, doi:10.1016/j.jpowsour.2013.06.151.
158. Bolloli, M.; Antonelli, C.; Molméret, Y.; Alloin, F.; Iojoiu, C.; Sanchez, J.-Y. Nanocomposite poly(vinylidene fluoride)/nanocrystalline cellulose porous membranes as separators for lithium-ion batteries. *Electrochim. Acta* **2016**, *214*, 38–48, doi:10.1016/j.electacta.2016.08.020.
159. Gor, G.Y.; Cannarella, J.; Leng, C.Z.; Vishnyakov, A.; Arnold, C.B. Swelling and softening of lithium-ion battery separators in electrolyte solvents. *J. Power Sources* **2015**, *294*, 167–172, doi:10.1016/j.jpowsour.2015.06.028.
160. Lis, M.; Chudzik, K.; Bakierska, M.; Świętosławski, M.; Gajewska, M.; Rutkowska, M.; Molenda, M. Aqueous Binder for Nanostructured Carbon Anode Materials for Li-Ion Batteries. *J. Electrochem. Soc.* **2019**, *166*, A5354-A5361, doi:10.1149/2.0591903jes.
161. Singh, M.; Kaiser, J.; Hahn, H. Thick Electrodes for High Energy Lithium Ion Batteries. *J. Electrochem. Soc.* **2015**, *162*, A1196-A1201, doi:10.1149/2.0401507jes.
162. Shin, D.; Park, H.; Paik, U. Cross-linked poly(acrylic acid)-carboxymethyl cellulose and styrene-butadiene rubber as an efficient binder system and its physicochemical effects on a high energy density graphite anode for Li-ion batteries. *Electrochemistry Communications* **2017**, *77*, 103–106, doi:10.1016/j.elecom.2017.02.018.

163. Frankenberger, M.; Singh, M.; Dinter, A.; Jankowksy, S.; Schmidt, A.; Pettinger, K.-H. Laminated Lithium Ion Batteries with improved fast charging capability. *Journal of Electroanalytical Chemistry* **2019**, *837*, 151–158, doi:10.1016/j.jelechem.2019.02.030.
164. Chernysh, O.; Khomenko, V.; Makyeyeva, I.; Barsukov, V. Effect of binder's solvent on the electrochemical performance of electrodes for lithium-ion batteries and supercapacitors. *Materials Today: Proceedings* **2019**, *6*, 42–47, doi:10.1016/j.matpr.2018.10.073.
165. Dodero, A.; Vicini, S.; Alloisio, M.; Castellano, M. Sodium alginate solutions: correlation between rheological properties and spinnability. *J Mater Sci* **2019**, *54*, 8034–8046, doi:10.1007/s10853-019-03446-3.
166. Ma, J.; Lin, Y.; Chen, X.; Zhao, B.; Zhang, J. Flow behavior, thixotropy and dynamical viscoelasticity of sodium alginate aqueous solutions. *Food Hydrocolloids* **2014**, *38*, 119–128, doi:10.1016/j.foodhyd.2013.11.016.
167. Dodero, A.; Vicini, S.; Alloisio, M.; Castellano, M. Rheological properties of sodium alginate solutions in the presence of added salt: an application of Kulicke equation. *Rheol Acta* **2020**, *59*, 365–374, doi:10.1007/s00397-020-01206-8.
168. Zhong, D.; Huang, X.; Yang, H.; Cheng, R. New insights into viscosity abnormality of sodium alginate aqueous solution. *Carbohydr. Polym.* **2010**, *81*, 948–952, doi:10.1016/j.carbpol.2010.04.012.
169. Fang, D.; Liu, Y.; Jiang, S.; Nie, J.; Ma, G. Effect of intermolecular interaction on electrospinning of sodium alginate. *Carbohydr. Polym.* **2011**, *85*, 276–279, doi:10.1016/j.carbpol.2011.01.054.
170. García, A.; Culebras, M.; Collins, M.N.; Leahy, J.J. Stability and rheological study of sodium carboxymethyl cellulose and alginate suspensions as binders for lithium ion batteries. *Journal of Applied Polymer Science* **2018**, *135*, 46217, doi:10.1002/app.46217.
171. Ganapathy, S.; Wagemaker, M. Nanosize storage properties in spinel Li<sub>4</sub>Ti<sub>5</sub>O<sub>12</sub> explained by anisotropic surface lithium insertion. *ACS Nano* **2012**, *6*, 8702–8712, doi:10.1021/nn302278m.
172. Li, J.; Armstrong, B.L.; Daniel, C.; Kiggans, J.; Wood, D.L. Optimization of multicomponent aqueous suspensions of lithium iron phosphate (LiFePO<sub>4</sub>) nanoparticles and carbon black for lithium-ion battery cathodes. *Journal of Colloid and Interface Science* **2013**, *405*, 118–124, doi:10.1016/j.jcis.2013.05.030.
173. Bitsch, B.; Dittmann, J.; Schmitt, M.; Scharfer, P.; Schabel, W.; Willenbacher, N. A novel slurry concept for the fabrication of lithium-ion battery electrodes with beneficial properties. *J. Power Sources* **2014**, *265*, 81–90, doi:10.1016/j.jpowsour.2014.04.115.
174. Adamson, A.W.; Gast, A.P. *Physical chemistry of surfaces*, 6th ed.; John Wiley & Sons, Inc.: New York, 1967.
175. Wang, Y.Q.; Wan, L.J.; Guo, Y.G. Inkjet-printed thin films of nanostructured electrode materials for lithium-ion batteries. *Chin. Sci. Bull.* **2013**, *58*, 3227–3232, doi:10.1360/972013-794.
176. Risthaus, T.; Zhou, D.; Cao, X.; He, X.; Qiu, B.; Wang, J.; Zhang, L.; Liu, Z.; Paillard, E.; Schumacher, G.; et al. A high-capacity P2 Na<sub>2</sub>/3Ni<sub>1</sub>/3Mn<sub>2</sub>/3O<sub>2</sub> cathode material for sodium ion batteries with oxygen activity. *J. Power Sources* **2018**, *395*, 16–24, doi:10.1016/j.jpowsour.2018.05.026.
177. Rezende, R.A.; Bártolo, P.J.; Mendes, A.; Filho, R.M. Rheological behavior of alginate solutions for biomanufacturing. *J. Appl. Polym. Sci.* **2009**, *113*, 3866–3871, doi:10.1002/app.30170.
178. Belalia, F., Djelali, N.-E. Rheological properties of sodium alginate solutions. *Roumanian Journal of Chemistry* **2014**, *59*, 135–145.
179. Yu, J.; Zhao, Z.; Sun, J.; Geng, C.; Bu, Q.; Wu, D.; Xia, Y. Electrospinning Highly Concentrated Sodium Alginate Nanofibres without Surfactants by Adding Fluorescent Carbon Dots. *Nanomaterials* **2020**, *10*, 565, doi:10.3390/nano10030565.

180. Cho, K.Y.; Kwon, Y.I.; Youn, J.R.; Song, Y.S. Evaluation of slurry characteristics for rechargeable lithium-ion batteries. *Materials Research Bulletin* **2013**, *48*, 2922–2926, doi:10.1016/j.materresbull.2013.04.026.
181. Cho, K.Y.; Kwon, Y.I.; Youn, J.R.; Song, Y.S. Interaction analysis between binder and particles in multiphase slurries. *Analyt* **2013**, *138*, 2044–2050, doi:10.1039/c3an36720g.
182. Kwon, Y.I.; Kim, J.D.; Song, Y.S. Agitation Effect on the Rheological Behavior of Lithium-Ion Battery Slurries. *Journal of Elec Materi* **2015**, *44*, 475–481, doi:10.1007/s11664-014-3349-1.
183. Lim, S.; Kim, S.; Ahn, K.H.; Lee, S.J. The effect of binders on the rheological properties and the microstructure formation of lithium-ion battery anode slurries. *J. Power Sources* **2015**, *299*, 221–230, doi:10.1016/j.jpowsour.2015.09.009.
184. Phanikumar, V.V.N.; Rikka, V.R.; Das, B.; Gopalan, R.; Appa Rao, B.V.; Prakash, R. Investigation on polyvinyl alcohol and sodium alginate as aqueous binders for lithium-titanium oxide anode in lithium-ion batteries. *Ionics* **2019**, *25*, 2549–2561, doi:10.1007/s11581-018-2751-8.
185. Bauer, W.; Nötzel, D. Rheological properties and stability of NMP based cathode slurries for lithium ion batteries. *Ceramics International* **2014**, *40*, 4591–4598, doi:10.1016/j.ceramint.2013.08.137.
186. Ouyang, L.; Wu, Z.; Wang, J.; Qi, X.; Li, Q.; Wang, J.; Lu, S. The effect of solid content on the rheological properties and microstructures of a Li-ion battery cathode slurry. *RSC Adv.* **2020**, *10*, 19360–19370, doi:10.1039/d0ra02651d.
187. Yue, Z.; Economy, J. Synthesis of highly mesoporous carbon pellets from carbon black and polymer binder by chemical activation. *Microporous and Mesoporous Materials* **2006**, *96*, 314–320, doi:10.1016/j.micromeso.2006.07.025.
188. Hecht, H.; Srebnik, S. Structural Characterization of Sodium Alginate and Calcium Alginate. *Biomacromolecules* **2016**, *17*, 2160–2167, doi:10.1021/acs.biomac.6b00378.
189. Kracalik, M. Recycled clay/PET nanocomposites evaluated by novel rheological analysis approach. *Applied Clay Science* **2018**, *166*, 181–184, doi:10.1016/j.clay.2018.09.007.
190. Lee, J.-H.; Choi, Y.-M.; Paik, U.; Park, J.-G. The effect of carboxymethyl cellulose swelling on the stability of natural graphite particulates in an aqueous medium for lithium ion battery anodes. *J Electroceram* **2006**, *17*, 657–660, doi:10.1007/s10832-006-8975-4.
191. Qiu, L.; Shao, Z.; Wang, D.; Wang, F.; Wang, W.; Wang, J. Novel polymer Li-ion binder carboxymethyl cellulose derivative enhanced electrochemical performance for Li-ion batteries. *Carbohydr. Polym.* **2014**, *112*, 532–538, doi:10.1016/j.carbpol.2014.06.034.
192. Saunier, J.; Alloin, F.; Sanchez, J.Y.; Barrière, B. Plasticized microporous poly(vinylidene fluoride) separators for lithium-ion batteries. I. Swelling behavior of dense membranes with respect to a liquid electrolyte-Characterization of the swelling equilibrium. *J. Polym. Sci. B Polym. Phys.* **2004**, *42*, 532–543, doi:10.1002/polb.10730.
193. Choi, N.-S.; Ha, S.-Y.; Lee, Y.; Jang, J.Y.; Jeong, M.-H.; Shin, W.C.; Ue, M. Recent Progress on Polymeric Binders for Silicon Anodes in Lithium-Ion Batteries. *J. Electrochem. Sci. Te.* **2015**, *6*, 35–49, doi:10.5229/JECST.2015.6.2.35.
194. Chou, S.-H.; Pan, Y.; Wang, J.-Z.; Liu, H.-K.; Dou, S.-X. Small things make a big difference: binder effects on the performance of Li and Na batteries. *Phys. Chem. Chem. Phys.* **2014**, *16*, 20347–20359.
195. Wang, R.; Wang, Z.; Li, X.; Zhang, H. Electrochemical Analysis the influence of Propargyl Methanesulfonate as Electrolyte Additive for Spinel LTO Interface Layer. *Electrochim. Acta* **2017**, *241*, 208–219, doi:10.1016/j.electacta.2017.04.125.
196. Lee, M.-L.; Li, Y.H.; Liao, S.-C.; Chen, J.-M.; Yeh, J.-W.; Shih, H.C. Li<sub>4</sub>Ti<sub>5</sub>O<sub>12</sub>-coated graphite anode materials for lithium-ion batteries. *Electrochim. Acta* **2013**, *112*, 529–534, doi:10.1016/j.electacta.2013.08.150.

197. Lv, W.; Gu, J.; Niu, Y.; Wen, K.; He, W. Review—Gassing Mechanism and Suppressing Solutions in Li<sub>4</sub>Ti<sub>5</sub>O<sub>12</sub>-Based Lithium-Ion Batteries. *J. Electrochem. Soc.* **2017**, *164*, A2213-A2224, doi:10.1149/2.0031712jes.
198. Widmaier, M.; Jäckel, N.; Zeiger, M.; Abuzarli, M.; Engel, C.; Bommer, L.; Presser, V. Influence of carbon distribution on the electrochemical performance and stability of lithium titanate based energy storage devices. *Electrochim. Acta* **2017**, *247*, 1006–1018, doi:10.1016/j.electacta.2017.07.073.
199. Gaberscek, M.; Moskon, J.; Erjavec, B.; Dominko, R.; Jamnik, J. The Importance of Interphase Contacts in Li Ion Electrodes: The Meaning of the High-Frequency Impedance Arc. *Electrochem. Solid-State Lett.* **2008**, *11*, A170, doi:10.1149/1.2964220.
200. Jossen, A.; Weydanz, W. *Moderne Akkumulatoren richtig einsetzen*; Reichardt Verlag, 2006, ISBN 978-3939359111.
201. Frankenberger, M.; Singh, M.; Dinter, A.; Pettinger, K.-H. EIS Study on the Electrode-Separator Interface Lamination. *Batteries* **2019**, *5*, 71, doi:10.3390/batteries5040071.
202. Waag, W.; Käbitz, S.; Sauer, D.U. Experimental investigation of the lithium-ion battery impedance characteristic at various conditions and aging states and its influence on the application. *Applied Energy* **2013**, *102*, 885–897, doi:10.1016/j.apenergy.2012.09.030.
203. Ma, M.; Mansour, A.N.; Ko, J.K.; Waller, G.H.; Hendricks, C.E. Characterization of Li Diffusion and Solid Electrolyte Interface for Li<sub>4</sub>Ti<sub>5</sub>O<sub>12</sub> Electrode Cycled with an Organosilicon Additive Electrolyte. *J. Electrochem. Soc.* **2020**, *167*, 110549, doi:10.1149/1945-7111/aba5d3.
204. Kawade, U.V.; Jayswal, M.S.; Ambalkar, A.A.; Kadam, S.R.; Panmand, R.P.; Ambekar, J.D.; Kulkarni, M.V.; Kale, B.B. Surface modified Li<sub>4</sub>Ti<sub>5</sub>O<sub>12</sub> by paper templated approach for enhanced interfacial Li<sup>+</sup> charge transfer in Li-ion batteries. *RSC Adv.* **2018**, *8*, 38391–38399, doi:10.1039/c8ra07953f.
205. Ishihara, Y.; Miyazaki, K.; Fukutsuka, T.; Abe, T. Kinetics of Lithium-Ion Transfer at the Interface between Li<sub>4</sub>Ti<sub>5</sub>O<sub>12</sub> Thin Films and Organic Electrolytes. *ECS Electrochemistry Letters* **2014**, *3*, A83-A86, doi:10.1149/2.0011408eel.
206. Ma, J.; Li, Y.; Grundish, N.S.; Goodenough, J.B.; Chen, Y.; Guo, L.; Peng, Z.; Qi, X.; Yang, F.; Qie, L.; et al. The 2021 battery technology roadmap. *J. Phys. D: Appl. Phys.* **2021**, *54*, 183001, doi:10.1088/1361-6463/abd353.
207. Helmich, U. Schalenmodell: Drei Atome, dargestellt nach dem Schalenmodell. Available online: <http://www.u-helmich.de/che/0809/03-atombau/atombau04.html> (accessed on 20 October 2021).
208. Delmas, C.; Nadiri, A.; Soubeyroux, J.L. The nasicon-type titanium phosphates Ati<sub>2</sub>(PO<sub>4</sub>)<sub>3</sub> (A=Li, Na) as electrode materials. *Solid State Ionics* **1988**, *28-30*, 419–423, doi:10.1016/S0167-2738(88)80075-4.
209. Li, N.; Wang, Y.; Rao, R.; Dong, X.; Zhang, X.; Zhu, S. The preparation and graphene surface coating NaTi<sub>2</sub>(PO<sub>4</sub>)<sub>3</sub> as cathode material for lithium ion batteries. *Applied Surface Science* **2017**, *399*, 624–629, doi:10.1016/j.apsusc.2016.12.117.
210. Chen, M.; Liu, Q.; Wang, S.-W.; Wang, E.; Guo, X.; Chou, S.-L. High-Abundance and Low-Cost Metal-Based Cathode Materials for Sodium-Ion Batteries: Problems, Progress, and Key Technologies. *Adv. Energy Mater.* **2019**, *9*, 1803609, doi:10.1002/aenm.201803609.
211. Zhang, Q.; Liao, C.; Zhai, T.; Li, H. A High Rate 1.2V Aqueous Sodium-ion Battery Based on All NASICON Structured NaTi<sub>2</sub>(PO<sub>4</sub>)<sub>3</sub> and Na<sub>3</sub>V<sub>2</sub>(PO<sub>4</sub>)<sub>3</sub>. *Electrochim. Acta* **2016**, *196*, 470–478, doi:10.1016/j.electacta.2016.03.007.
212. Vujković, M.; Mitrić, M.; Mentus, S. High-rate intercalation capability of NaTi<sub>2</sub>(PO<sub>4</sub>)<sub>3</sub>/C composite in aqueous lithium and sodium nitrate solutions. *J. Power Sources* **2015**, *288*, 176–186, doi:10.1016/j.jpowsour.2015.04.132.

213. Cao, X.; Yang, Y. Facile synthesis of NaTi<sub>2</sub>(PO<sub>4</sub>)<sub>3</sub>-carbon composite through solid state method and its application in aqueous sodium ion battery. *Materials Letters* **2018**, *231*, 183–186, doi:10.1016/j.matlet.2018.08.020.
214. Yuan, C.; Zhang, Y.; Pan, Y.; Liu, X.; Wang, G.; Cao, D. Investigation of the intercalation of polyvalent cations (Mg<sup>2+</sup>, Zn<sup>2+</sup>) into λ-MnO<sub>2</sub> for rechargeable aqueous battery. *Electrochim. Acta* **2014**, *116*, 404–412, doi:10.1016/j.electacta.2013.11.090.
215. Albanelli, N. *Anodi a base di titanio per batterie sodio-ione: Bachelor-Thesis*, **2019**.
216. Bargnesi, L.; Gigli, F.; Faggiano, L.; Albanelli, N.; Toigo, C.; Arbizzani, C. Crosslinked binders for sustainable aqueous Na-ion batteries. *Nanomaterials* **2021**, under submission.

## 8 List of acronyms

BET	Brunauer-Emmett-Teller
CA	contact angle
CB	carbon black
CC-CV	constant current-constant voltage
CCV	complex cumulative viscosity
CE	counter electrode
CEf	coulombic efficiency
CEI	cathode electrolyte interphase
CN	coordination number
CSF	cumulative storage factor
CyV	cyclovoltammetry, cyclic voltammetry
CMC	carboxy methyl cellulose
DEC	diethyl carbonate
DMC	dimethyl carbonate
DSC	differential scanning calorimetry
EC	ethylene carbonate
EDX	electron-dispersive X-ray spectroscopy
EMC	ethyl methyl carbonate
EIS	electrochemical impedance spectroscopy
ESB	energy selective backscatter detector
EV	electric vehicle
FEC	fluoro ethylene carbonate
FIB	focus ion beam
KAc	kalium acetate
HEC	hydroxy ethyl cellulose
LCA	life cycle analysis
LFMP	lithium iron manganese phosphate

LFP	lithium iron phosphate
LIB	Lithium ion battery
LMO	lithium manganese oxide
LMP	lithium manganese phosphate
LNO	lithium nickel oxide
LTO	Lithium titanate
NaAc	sodium acetate
NASICON	sodium super ionic conductor
NMC	lithium nickel manganese cobalt oxide
NMP	N-methyl pyrrolidone
NTP	sodium titanium phosphate
PAA	polyacrylic acid
PC	propylene carbonate
PE	polyethylene
PEG	polyethylene glycol
PEK	polyether ketone
PI	polyimide
PP	polypropylene
PVDF	poly vinylidene fluoride
RE	reference electrode
RF	roughness factor
SA	sodium alginate
SBR	styrene butadiene rubber
SEI	solid electrolyte interphase
SEM	scanning electron microscopy
SOC	state of charge
SOH	state of health
TEGDME	tetraethylene glycol dimethyl ether
TMP	trimethyl phosphate
TGA	thermogravimetric analysis

VC	vinylene carbonate
WE	working electrode
WISE	water in salt electrolyte
XRD	x-ray diffraction

## 9 List of figures

Figure 1: Scheme of lithium insertion/de-insertion .....	2
Figure 2: Typical charging-discharging cycle of a LFMP/graphite full cell, performed at C/10 rate. CCCV charging up to 4.3 V and CC discharging up to 2.0 V [14]. .....	6
Figure 3: Layered structure of graphite, reprinted from ref. [26] with permission of Springer Nature. 9	
Figure 4: Scheme of graphite electrode covered with an inhomogeneous SEI. ....	10
Figure 5: Cross-section scheme of electrode setup. Reprinted from ref. [50] under the terms of the Creative Commons CC-BY license.....	19
Figure 6: Evaluated binders, from left to right: Poly vinylidene difluoride (PVDF), Sodium carboxymethyl cellulose (Na-CMC) and Sodium alginate (SA).....	20
Figure 7: a) isotactic, b) syndiotactic and c) atactic polymer. ....	23
Figure 8: Schematic drawing of chain structure of amorphous (left) and crystalline (right) polymer. Reprinted from ref. [49] under the terms of the Creative Commons CC-BY license. ....	24
Figure 9: Processing steps for preparation of LIB electrode. Reprinted from [45] under the terms of the Creative Commons CC-BY license. ....	24
Figure 10: Scheme on continuous coating of battery slurry upon current collector foil. ....	26
Figure 11: Schematic set-up of Swagelok (R) three-electrode arrangement. Reprinted from ref. [49] under the terms of the Creative Commons CC-BY license. ....	28
Figure 12: Set-up of Swagelok (R) three-electrode arrangement. Reprinted from ref. [29] under the terms of the Creative Commons CC-BY license.....	28
Figure 13: Dimensions of separator (left), anode (middle) and cathode (right) for lab-scale cell preparation.....	29
Figure 14: Schematic set-up of capacitance measurement. Reprinted from ref. [49] under the terms of the Creative Commons CC-BY license. ....	41
Figure 15: Viscosity curve for different kinds of fluids, a) ideal viscous, b) shear-thinning and c) shear-thickening. ....	42
Figure 16: Swelling measurement with ethanol at different dry thicknesses. Reprinted from ref. [49] under the terms of the Creative Commons CC-BY license. ....	58
Figure 17: Swelling tests of binders with different crystallinities with mixture of EC/DMC. Reprinted from ref. [49] under the terms of the Creative Commons CC-BY license. ....	59
Figure 18: Swelling test – practical procedure. ....	60
Figure 19: EDX image of a) low, b) medium, c) high crystallinity PVDF. Reprinted from ref. [49] under the terms of the Creative Commons CC-BY license. ....	60
Figure 20: Schematic set-up of peeling test (a), typical results: mostly adhesive (b) and cohesive (c) breaking. Reprinted from ref. [49] under the terms of the Creative Commons CC-BY license. ....	62
Figure 21: Results of peeling test for different crystallinities and electrode thicknesses. Reprinted from ref. [49] under the terms of the Creative Commons CC-BY license. ....	62
Figure 22: Result of bending test - example delamination. ....	63
Figure 23: Result of bending test - no delamination. Reprinted from ref. [49] under the terms of the Creative Commons CC-BY license.....	64
Figure 24: Charge-discharge profiles of graphite anodes containing different types of water-based PVDF binder at different C-rates: a) 0.1 C b) 1 C c) 3C d) 5C rate. Reprinted from ref. [49] under the terms of the Creative Commons CC-BY license.....	65
figure 25: Result of half-cell C-rate test. Reprinted from ref. [49] under the terms of the Creative Commons CC-BY license. ....	66

Figure 26: Electrochemical performance of full cells (a) charge-discharge profiles at 0.1 C rate; (b) discharge capacity data at different C-rates. Reprinted from ref. [49] under the terms of the Creative Commons CC-BY license. ....	67
Figure 27: Irreversible capacity losses during formation of full cells. Reprinted from ref. [49] under the terms of the Creative Commons CC-BY license. ....	68
Figure 28: Chemical structure of SA. ....	70
Figure 29: Chemical structure of SA (left) and its polyelectrolyte structure in salt-free (middle) and salt-containing environment (right). Reprinted from ref. [45] under the terms of the Creative Commons CC-BY license. ....	71
Figure 30: Photograph of de-mixing slurry with small particles of CB on water surface – directly after mixing. Reprinted from ref. [45] under the terms of the Creative Commons CC-BY license.....	72
Figure 31: SEM images of LTO-SA electrode in pristine state (a) and after 80 cycles (b). Reprinted from ref. [50] under the terms of the Creative Commons CC-BY license. ....	73
Figure 32: SEM pictures of SA3 (a,d), SAD1 (b,e) and SAD2 (c,f). Reprinted from ref. [45] under the terms of the Creative Commons CC-BY license. ....	73
Figure 33: Scheme on detergent influence on active material particles (left: with detergent, right: without detergent). Reprinted from ref. [45] under the terms of the Creative Commons CC-BY license. ....	74
Figure 34: Graphical analysis of elementary mass-shares, derived from EDX-measurements.....	75
Figure 35: Result of peeling test for LTO-SA at different dry thickness. ....	75
Figure 36: Different droplet forms on substrate (left) and CA measurement (right). Reprinted from ref. [45] under the terms of the Creative Commons CC-BY license. ....	76
Figure 37: Viscosity as a function of shear rate for LTO-SA slurry directly and 24 hours after mixing. ....	79
Figure 38: Shear stress vs shear rate for different SA-LTO slurries. Reprinted from ref. [45] under the terms of the Creative Commons CC-BY license. ....	80
Figure 39: Shear rate vs viscosity for slurries at different temperatures. Green = 20 °C, orange = 30 °C, red = 40 °C. Reprinted from ref. [45] under the terms of the Creative Commons CC-BY license.....	81
Figure 40: Storage and loss modulus for three different SA-based slurries. Reprinted from ref. [45] under the terms of the Creative Commons CC-BY license. ....	82
Figure 41: Cumulative complex viscosity vs. cumulative storage factor for all tested slurries. Reprinted from ref. [45] under the terms of the Creative Commons CC-BY license. ....	83
Figure 42: CA measurements, exemplary for SAD2 (54.98 °), SAD3 (66.77 °) and SA3 (74.17 °). Reprinted from ref. [45] under the terms of the Creative Commons CC-BY license. ....	84
Figure 43: medium CA for different tested slurries, equipped with error bars. Reprinted from ref. [45] under the terms of the Creative Commons CC-BY license. ....	84
Figure 44: Chemical structure of CMC. ....	86
Figure 45: SEM images of the two types of pristine electrodes: (a,c) LTO/PVDF-CMC and (b,d) LTO/PVDF-SA. Reprinted from ref. [50] under the terms of the Creative Commons CC-BY license.....	87
Figure 46: Result of peeling test for LTO-PVDF/SA and -PVDF/CMC electrodes at different dry thickness.....	88
Figure 47: Viscosity as a function of the shear rate for different slurries: (a) directly after mixing and (b) 24 hours after mixing.....	89
Figure 48: Difference between the slurries seven days after mixing containing (a) LTO-PVDF/CMC and (b) LTO-PVDF/SA binder systems. Reprinted from ref. [50] under the terms of the Creative Commons CC-BY license. ....	90
Figure 49: Charge-discharge profiles of LTO anodes at (a) 0.33 C, (b) 1 C, (c) 5 C and (d) 10 C. Reprinted from ref. [50] under the terms of the Creative Commons CC-BY license. ....	92

Figure 50: Electrochemical performance during C-rate test (a) and charge capacities for each of 2 exemplary electrodes (b). Reprinted from ref. [50] under the terms of the Creative Commons CC-BY license.....	93
Figure 51: SEM of dendritic foil covered with graphite particles. Reprinted from ref. [29] under the terms of the Creative Commons CC-BY license.....	96
Figure 52: FIB-SEM images of untreated (a) and dendritic (b-d) copper foil. Colour map false colour images c) and d): orange = copper, blue = LTO, green = binder and conductive additive. Reprinted from ref. [29] under the terms of the Creative Commons CC-BY license. ....	97
Figure 53: Scheme on connectivity of particles at different sizes; micrometer-scale flakes on plain (a) and treated (b) copper surface and sub-micron particles on plain (c) and treated (d) copper surface. Reprinted from ref. [29] under the terms of the Creative Commons CC-BY license. ....	98
Figure 54: Comparison of failure mechanisms a) and internal resistance b) of LTO electrodes for untreated and dendritic copper foil as current collector. Reprinted from ref. [29] under the terms of the Creative Commons CC-BY license. ....	99
Figure 55: Galvanostatic charge/discharge test a) and C-rate test b) of LTO electrodes with untreated and dendritic current collectors. The error bars are also displayed. Reprinted from ref. [29] under the terms of the Creative Commons CC-BY license.....	100
Figure 56: Impedance measurements (100 kHz – 10 mHz) of LTO electrodes on untreated or dendritic current collectors; three-electrode (T-cell) geometry; fitting curves indicated as solid lines; the data points at 1 kHz highlighted in pale blue; frequencies of final datapoints indicated for partially visible datasets. Reprinted from ref. [29] under the terms of the Creative Commons CC-BY license.....	101
Figure 57: Equivalent circuit model used for EIS fit analysis.....	101
Figure 58: EIS fitting parameters of LTO electrodes with untreated or dendritic current collectors, along 3rd cycle lithiation step; data normalized to geometric electrode area. Reprinted from ref. [29] under the terms of the Creative Commons CC-BY license.....	102
Figure 59: Averaged EIS fitting parameters of LTO electrodes with untreated or dendritic current collectors, along 3rd cycle lithiation step; data normalized to geometric electrode area. The point near 90% is the result of a single measurement. Reprinted from ref. [29] under the terms of the Creative Commons CC-BY license.....	104
Figure 60: Comparison of surface increase factors at the electrode current collector interface, determined via roughness factor shift, surface capacitance shift and surface resistance shift; measured error bars indicated as solid lines, estimated error bars indicated as dashed lines. Reprinted from ref. [29] under the terms of the Creative Commons CC-BY license. ....	105
Figure 61: Size and electron configuration of lithium and sodium atom. Reprinted from ref. [207] under the terms of the Creative Commons CC-BY license.....	108
Figure 62: Mixed educts in ball mill (left), sintered product “sample 4” (middle) and carbon-coated product (right). ....	110
Figure 63: Result of XRD measurements for samples 1-4, synthesized by route #1.....	111
Figure 64: Result of XRD-measurement for samples 4-5, synthesized by route #1.....	112
Figure 65: Result of TGA measurement of first NTP synthesis, synthesized by route #1. ....	113
Figure 66: Product synthesis route #3 after ball-milling and carbon-coating.....	114
Figure 67: TGA analysis of prepared NTP according synthesis route #3.....	115
Figure 68: Comparison of products following synthesis route #1 and #3.....	115
Figure 69: Result of XRD measurement for lambda-MnO <sub>2</sub> synthesis product.....	117
Figure 70: SEM images of synthesized lambda-MnO <sub>2</sub> .....	117
Figure 71: XRD analysis of lambda-MnO <sub>2</sub> prepared with sulfuric acid. ....	118
Figure 72: SEM images of unpressed (a) and pressed (b) NTP anode (reprinted with permission from ref [215])......	119

Figure 73: Cyclovoltammetry of unpressed electrode #28 at different scan speeds (0.1 mV/s in blue and 0.2 mV/s in orange), reprinted with permission from ref. [215]. .....	120
Figure 74: CyV diagram of electrode #10 equipped with carbon paper at 0.05 mV/s. Reprinted with permission form ref. [215]. .....	121
Figure 75: CyV diagram of pressed electrode #29 at different measurement speeds of 2 (blue), 5 (orange), 10 (grey) and 20 (yellow) mV/s. Reprinted with permission from ref. [215]. .....	122
figure 76: Comparison between unpressed electrode (#7, orange) and carbon paper electrode (#33, blue) at 0.1 mV/S. Reprinted with permission from ref. [215]. .....	123
figure 77: CyV of NTP electrode (6 mg cm <sup>-2</sup> ) with chitosan binder in aqueous 1.5 M Na <sub>2</sub> SO <sub>4</sub> -solution at 0.5 mV s <sup>-1</sup> . .....	124

## 10 List of tables

Table 1: List of LIB cathode materials.....	7
Table 2: Overview on different anode materials for LIBs.....	13
Table 3: Common electrolyte solvents in LIBs.....	14
Table 4: Common electrolyte salts for LIBs.....	14
Table 5: Overview on typical active materials and their electronic conductivities.....	17
Table 6: Formulations for reference graphite electrode.....	47
Table 7: Formulation for graphite electrodes containing water-based PVDF binder.....	47
Table 8: Formulation of LTO electrodes.....	49
Table 9: Slurry characteristics and composition for rheological experiments.....	49
Table 10: Result of bending tests for all electrode formulations and thicknesses.....	64
Table 11: Mass-shares derived from EDX measurement.....	74
Table 12: Cumulative complex viscosity (CCV) and cumulative storage factor (CSF) for all tested slurries.....	82
Table 13: Results of CA measurements.....	84
Table 14: Averaged EIS fit parameters of LTO electrodes.....	104
Table 15: Comparison of different synthesis routes for NTP.....	109
Table 16: Used chemicals for synthesis route #1.....	111
Table 17: Used chemicals for synthesis route #3.....	114
Table 18: Step-wise addition of diluted HCl for preparation of lambda-MnO <sub>2</sub> .....	116
Table 19: Active material weight and electrolyte volume for electrodes.....	119

## 11 List of publications

C.Toigo, M. Singh, B. Gmeiner, M. Biso, K.-H. Pettinger, *J. Electrochem. Soc.* 167 020514 (2020),  
“A Method to Measure the Swelling of Water-Soluble PVDF Binder System and Its Electrochemical Performance for Lithium Ion Batteries”

C. Toigo, M. Biso, K.-H. Pettinger, C. Arbizzani, *Molecules*, 25, 2443 (2020), “Study on Different Water-Based Binders for  $\text{Li}_4\text{Ti}_5\text{O}_{12}$  Electrodes

C. Toigo, M. Frankenberger, N. Billot, C. Pscherer, B. Stumper, F. Distelrath, J. Schubert, K.-H. Pettinger, C. Arbizzani, *Electrochimica Acta* 392, 138978 (2021) „Improved LTO electrodes by modified current collector surfaces”

C.Toigo, M.Krakalik, E.Bradt, K.-H.Pettinger, C.Arbizzani, *Polymers*, 13, 3582 (2021),  
“Rheological properties of aqueous sodium alginate slurries for LTO battery electrodes”

L. Bargnesi, F. Gigli, N. Albanelli, C.Toigo, C. Arbizzani, *Nanomaterials*, 12, 254 (2022),  
“Crosslinked chitosan binder for sustainable aqueous batteries”

## 12 List of contributions to conferences

Toigo C., Arbizzani, C.; “Study on different water-based binders and their performance for LTO electrodes”, **Poster Presentation** at Advanced Lithium Batteries for Automobile Applications (ABAA12), October 6<sup>th</sup> to 9<sup>th</sup> 2019, Ulm, Germany

Toigo C., Albanelli, N., Arbizzani, C., Pettinger, K.-H.; “Promising Electrode materials for Sodium Ion Batteries”, **Poster Presentation** at World Sustainable Energy Days, March 3<sup>rd</sup> to 6<sup>th</sup> 2020, Wels, Austria

Toigo C., Frankenberger M., Billot N., Pscherer C., Stumper B., Distelrath F., Schubert J., Pettinger K.-H., Arbizzani C.; „Improved LTO electrodes by modified current collector surfaces”, **oral presentation** at ISE 72<sup>nd</sup> meeting, August 29<sup>th</sup> to September 6<sup>th</sup> 2021, Korea (online)

Toigo C., Kracalik M., Bradt E., Pettinger K.-H., Arbizzani C.; „Rheological properties of aqueous sodium alginate slurries for LTO battery electrodes”, **oral presentation** at XXVII National SCI Congress, September 14<sup>th</sup> to 23<sup>rd</sup>, Italy (online)

Toigo C., Pettinger K.-H., Arbizzani C.; “Sodium Alginate - a promising bio-based polymer for the use in battery electrodes”, **oral presentation** at E-MRS (European Materials Research Society), September 20<sup>th</sup> to 23<sup>rd</sup>, Italy (online)